Title
First-principles calculations and model Hamiltonian approaches to electronic and optical properties of defects, interfaces and nanostructures

Author
Choi, Sangkook

Publication Date
2013

Peer reviewed|Thesis/dissertation

First-principles calculations and model Hamiltonian approaches to electronic and optical properties of defects, interfaces and nanostructures

by

Sangkook Choi

A dissertation submitted in partial satisfaction of the

requirements for the degree of

Doctor of Philosophy

in

Physics

in the

Grauduate Division

of the

University of California, Berkeley

Committee in charge:

Professor Steven G. Louie, Chair

Professor John Clarke

Professor Mark Asta

Fall 2013

First-principles calculations and model Hamiltonian approaches

to electronic and optical properties of defects, interfaces and nanostructures

Sangkook Choi

Abstract

First principles calculations and model Hamiltonian approaches
to electronic and optical properties of defects, interfaces and nanostructures

By

Sangkook Choi

Doctor of Philosophy in Physics

University of California, Berkeley

Professor Steven G. Louie, Chair

The dynamics of electrons governed by the Coulomb interaction determines a large portion of the observed phenomena of condensed matter. Thus, the understanding of electronic structure has played a key role in predicting the electronic and optical properties of materials. In this dissertation, I present some important applications of electronic structure theories for the theoretical calculation of these properties. In the first chapter, I review the basics necessary for two complementary electronic structure theories: model Hamiltonian approaches and first principles calculation. In the subsequent chapters, I further discuss the applications of these approaches to nanostructures (chapter II), interfaces (chapter III), and defects (chapter IV).

The abstract of each section is as follows.

● Section II-1

The sensitive structural dependence of the optical properties of single-walled carbon nanotubes, which are dominated by excitons and tunable by changing diameter and chirality, makes them excellent candidates for optical devices. Because of strong many-electron interaction effects, the detailed dependence of the optical oscillator strength f_S of excitons on nanotube diameter d, chiral angle θ, and electronic subband index P (the so-called family behavior) however has been unclear. In this study, based on results from an extended Hubbard Hamiltonian with parameters derived from *ab initio* GW-BSE calculations, we have obtained an explicit formula for the family behavior of the oscillator strengths of excitons in semiconducting single-walled carbon nanotubes (SWCNTs), incorporating environmental screening. The formula explains well recent measurements, and is expected to be useful in the understanding and design of possible SWCNT optical and optoelectronic devices.

● Section II-2

Wave supercollimation, in which a wavepacket is guided to move undistorted along a selected direction, is a highly desirable property that is difficult to achieve for photons and has yet to be experimentally seen for electrons. Disorder in a medium would inhibit supercollimation. Here, we report a counter-intuitive phenomenon of electron supercollimation

by disorder in graphene, made possible by its Dirac fermion states. We show that one can use one-dimensional disorder potentials to control electron wavepacket transport along the potential fluctuation direction. This is distinct from all known systems where the wavepacket would be further spread by the disorder and hindered in the potential fluctuating direction. This phenomenon has significant implications in the understanding and applications of transport in graphene and other Dirac fermion materials.

● Section III-1

The origin of magnetic flux noise in superconducting quantum interference devices with a power spectrum scaling as $1/f$ (f is frequency) has been a puzzle for over 20 years. This noise limits the decoherence time of superconducting qubits. A consensus has emerged that the noise arises from fluctuating spins of localized electrons with an areal density of $5\times10^{17}m^{-2}$. We show that the physical origin of the phenomenon are localized metal-induced gap states at the interface. In the presence of potential disorder at the metal-insulator interface, some of the metal-induced gap states become localized and produce local moments. A modest level of disorder yields the observed areal density.

● Section III-2

We present a microscopic theory of disorder-induced magnetic moment generation at nonmagnetic metal-insulator interfaces. Screened Hartree-Fock solution of a tight-binding Hamiltonian with electron-electron interaction, in which disorder is mimicked by the Anderson disorder model, shows that magnetic moments are originated from localized metal-induced gap states at the interface. Magnetic moment areal density becomes saturated at a maximum value of $4\times10^{17}m^{-2}$ as the disorder magnitude increases, consistent with the observed universality of measured local magnetic moment areal density. Dielectric screening effect is found to be essential for understanding the relatively universal behavior of the observed value.

● Section IV-1

Optical initialization of the negatively charged nitrogen-vacancy (NV^-) center in diamond makes it one of the best candidates for realization of addressable spins in the solid state for quantum computing and other studies. However, its exact mechanism was not clear. We show that exact diagonalization of a many-electron Hamiltonian with parameters derived from *ab initio* GW calculations puts strong constraints on the mechanism. The energy surfaces of the low-energy many-body states and the relaxation processes of photo-excitation responsible for the optical initialization are calculated. Intersystem crossings are shown to be essential

● Section IV-2

Graphene has been predicted to be a good test material for atomic collapse theory due to its linear band structure with a Fermi velocity 300 times slower than the speed of light. The Crommie group at UC Berkeley measured, using scanning tunneling microscopy, electrons bound to the positively charged calcium dimers on graphene, which corresponds to electrons collapsed to the super-heavy nucleus in artificial atoms. To compare measured bound states to atomic collapse theory in an artificial atom on graphene, the net charges associated with calcium

dimers should be quantified. Here, we quantified the net charges associated with a calcium dimer using density function theory.

For my family:

Jongchul Choi, Kyeja Hong,

Yongsub Lee, Jiye Choi, June Lee,

Byunggil Son, Jihyun Choi, Gaon Son, Laon Son,

Jundong Shin, Hyunae Yoon,

YoungSub Shin, Hyelim Choi

and Hyo Jeong Shin

Table of Contents

List of Figures

List of Tables

Acknowledgments

I would like to thank my advisor Prof. Steven G. Louie for his guidance and patience during my PhD; My collaborators Manish Jain, Jack Deslippe, Prof. John Clarke, Prof. Dung-Hai Lee, Prof. Marvin L. Cohen, Prof. Rodrigo B. Capaz, Prof. Feng Wang, Liang Tan, and Prof. Cheol-Hwan Park; my group mates Georgy Samsonidze, Sinisa Coh, Marco Bernardi, Felipe Jornada, Derek Vigil, Brad Barker, Jamal Mustafa, Diana Qiu, Ting Cao, and Chin Shen for many helpful discussions; my qualifying exam committee member Prof. Mark Asta; I thank the Samsung Foundation of Culture for fellowships.

I. Theoretical methods

The electronic and optical properties of a condensed matter system are dictated by the electrons in the system. Understanding materials properties involves solving quantum many-electron problems with the Hamiltonian:

$$H = H_0 + H_{\text{int}} \qquad \text{(I-1)}$$

with

$$H_0 = \sum_i \frac{p_i^2}{2m_e} + \sum_i H_{ext}(\boldsymbol{r}_i) \qquad \text{(I-2)}$$

and

$$H_{\text{int}} = \sum_{i>j} \frac{e^2}{|\boldsymbol{r}_i - \boldsymbol{r}_j|}, \qquad \text{(I-3)}$$

where $\boldsymbol{p}_i(\boldsymbol{r}_i)$ denotes momentum (position) operators of i th electron and $m_e(e)$ represents the mass (charge) of the electron. The term H_{ext} represents the interaction of electrons and external potentials such as potentials from nuclei.

Due to the huge number of particles in the system on the macroscopic scale, it is almost impossible to study the materials properties within many-body Schrodinger equation approaches. We should have an alternative theory which can handle many-electrons and their creation and annihilation in the system. Density functional theory and many-body theory provide an efficient and accurate means to study the ground and excited state properties of interacting electron system. Within these first principles approaches, it is feasible to determine many properties of materials directly from the fundamental Hamiltonian without empirical parameters.

However, due to its heavy computational cost, it is not always feasible to apply the above mentioned first principle approaches. For some complex systems, the number of degrees of freedom is so large that one will not be able to make theoretical progress by an approaches that treat all microscopic constituents as equally relevant degrees of freedom. In the majority of condensed matter applications, one is interested not so much in the full spectrum of a given system, but rather in its energetically low-lying dynamics. By constructing low energy effective Hamiltonian (which is mimicking the Hamiltonian in Eq. (I-1) in the low energy range) in the wisely-chosen restricted Hilbert space, we can calculate measurable quantities quantitatively. In addition, one can determine, from first principles, interaction parameters which are needed in model studies of condensed matter systems.

In this chapter, we review the basics of these complementary theoretical methods (first principles calculations and model Hamiltonian approaches): density functional theory, many-body theory, and model Hamiltonian approaches.

1. Density functional theory

(a) Hohenberg-Kohn theorem.

According to the first theorem of Hohenberg and Kohn [1,2], external potential $V_{ext}(\boldsymbol{r})$ is determined uniquely, except for a constant shift, by the ground state density $n_0(\boldsymbol{r})$, for any system of interacting particles in $V_{ext}(\boldsymbol{r})$. A corollary of this theorem is as follow. Since Hamiltonian is determined by $n_0(\boldsymbol{r})$ except for a constant shift, the many-body wavefunctions for ground and excited states are also determined by $n_0(\boldsymbol{r})$. Therefore, the properties of the system are completely determined by $n_0(\boldsymbol{r})$.

The second theorem states that a universal functional for the total energy $E[n]$ can be defined. For any $V_{ext}(\boldsymbol{r})$, $n_0(\boldsymbol{r})$ minimizes $E[n]$ at the exact ground state energy of the system. A direct consequence of the second theorem is that $E[n]$ is sufficient to determine the exact ground state energy and $n_0(\boldsymbol{r})$.

(b) The Kohn-Sham equations

The Kohn-Sham approach [2,3] is based on an ansatz: to mimic the original interacting many-body problem by an auxiliary independent-particle problem. The Kohn–Sham construction of an auxiliary system relies on two assumptions. First, the exact ground state density of the interacting system can be represented by the ground state density of an auxiliary non-interacting system. Second, the auxiliary Hamiltonian is chosen to have the usual kinetic operator and an effective local potential $V_{eff}^{\sigma}(\boldsymbol{r})$ acting on an electron of spin σ at position $\boldsymbol{r}$. This approach leads to exact calculations of properties of many-body systems using independent-particle methods and has made possible approximate formulations that have proved to be remarkably successful for the properties of the ground state in practice.

The Kohn–Sham approach is to write the ground state energy functional in the form

$$E_{KS}[n] = T_s[n] + \int d\boldsymbol{r} V_{ext}(\boldsymbol{r}) n(\boldsymbol{r}) + E_{hartree}[n] + E_{I-I}[n] + E_{xc}[n] \qquad \text{(I-4)}$$

with

$$n = \sum_{\sigma} \sum_{i=1}^{N_\sigma} \left| \psi_i^{\sigma} \right|^2 , \qquad \text{(I-5)}$$

$$T_s = -\sum_{\sigma}\sum_{i=1}^{N_\sigma}\frac{\left\langle \psi_i^\sigma \left| \nabla^2 \right| \psi_i^\sigma \right\rangle}{2}, \qquad \text{(I-6)}$$

and

$$E_{hartree} = \frac{1}{2}\int d\boldsymbol{r}d\boldsymbol{r}'\frac{n(\boldsymbol{r})n(\boldsymbol{r}')}{|\boldsymbol{r}-\boldsymbol{r}'|} \ . \quad \text{(I-7)}$$

Here, E_{I-I} is the interaction energy between nuclei and E_{xc} is exchange correlation functional.

From variational method which minimize the energy functional in Eq. (I-4), we can derive the Kohn-Sham equation of the auxiliary independent-particle system:

$$\left[-\frac{\hbar^2}{2m_e}\nabla^2 + V_{ext}(\boldsymbol{r}) + \int d\boldsymbol{r}'\frac{n(\boldsymbol{r}')}{|\boldsymbol{r}-\boldsymbol{r}'|} + V_{xc}^\sigma(\boldsymbol{r})\right]\psi_\sigma(\boldsymbol{r}) = \mathrm{E}_\sigma\,\psi_\sigma(\boldsymbol{r}) \qquad \text{(I-8)}$$

with

$$V_{xc}^\sigma(\boldsymbol{r}) = \frac{\delta E_{xc}[n]}{\delta n_\sigma(\boldsymbol{r})}. \qquad \text{(I-9)}$$

Eq. (I-8) is solved self-consistently to find the ground state density $n_\sigma(\boldsymbol{r})$ and the total energy. Although the exact form of $E_{xc}[n]$ is not known, it can reasonably be approximated in many cases within a local density approximation or generalized-gradient approximations for the properties of ground states.

2. Many-body theory

To study excited state properties of materials, we need to go beyond ground-state theories such as density function theory. Within many-body theory or quantum field theory, excited state properties of materials are understood in terms of the elementary excitation. To illustrate, photo-emission, transport, or tunneling technique, in general, yield the information on the quasi-electrons and quasi-holes. In an optical experiments, one can create an exciton, which is correlated electron-hole pair excitation. In this section, I would review single and two particle Greens function which yields the dynamics of quasiparticles and excitons, respectively.

(a) Field operators and second quantization

In quantum mechanics, the wave function is a complex-valued function of coordinates and time, which is "classical number" in Dirac's terminology. On the other hand, in quantum field theory, wave function is regarded as a field operator in the Fock-space satisfying certain

commutation relations. For a non-relativistic electron of which dynamics is governed by Schrodinger equation in Eq. (I-1), field operator for electrons satisfies anti-commutation relation of

$$\left[\psi(x),\psi^{\dagger}(x')\right]_{+} = \delta(x-x') . \quad \text{(I-10)}$$

and

$$\left[\psi(x),\psi(x')\right]_{+} = \left[\psi^{\dagger}(x),\psi^{\dagger}(x')\right]_{+} = 0 , \qquad \text{(I-11)}$$

where $[\ \ ]_{+}$ is anti-commutator. If the wave function $\psi(x)$ is expanded in terms of a basis set such that $\psi(x) = \sum_{n} c_n \varphi_n(x)$, the creation and annihilation operator of c_n and $c_n^{\dagger}$ must satisfy their own anti-commutation relations of

$$\left[c_n, c_{n'}^{\dagger}\right]_{+} = \delta_{n,n'} \qquad \text{(I-12)}$$

and

$$\left[c_n, c_{n'}\right]_{+} = \left[c_n^{\dagger}, c_{n'}^{\dagger}\right]_{+} = 0 . \qquad \text{(I-13)}$$

For any one body operator of $\sum_{i} A(\boldsymbol{r}_i)$ in many-body quantum mechanics, corresponding second-quantized operator is given by

$$\hat{A} = \int d\boldsymbol{r}\, \psi^{\dagger}(\boldsymbol{r}) A(\boldsymbol{r}) \psi(\boldsymbol{r}) = \left\langle n \middle| A \middle| m \right\rangle c_n^{\dagger} c_m . \qquad \text{(I-14)}$$

For any two body operator of $B = \sum_{i>j} B(\boldsymbol{r}_i - \boldsymbol{r}_j)$ in many-body quantum mechanics, corresponding second-quantized operator is given by

$$\begin{aligned} \hat{B} &= (1/2) \int d\boldsymbol{r} d\boldsymbol{r}'\, \psi^{\dagger}(\boldsymbol{r}) \psi^{\dagger}(\boldsymbol{r}') B(\boldsymbol{r}-\boldsymbol{r}') \psi(\boldsymbol{r}') \psi(\boldsymbol{r}) \\ &= (1/2) \left\langle mn \middle| B \middle| pq \right\rangle c_m^{\dagger} c_n^{\dagger} c_p c_q \end{aligned} \qquad \text{(I-15)}$$

(b) Single-particle Green's function

Single-particle Green's function $G(1,2)$ describes how a quasiparticle propagates from coordinates $\boldsymbol{r}_2$ at time t_2 to coordinates $\boldsymbol{r}_1$ at time t_1 with a boundary condition of $\delta(\boldsymbol{r}_1 - \boldsymbol{r}_2)$ at time t_2. In the non-relativistic quantum mechanics, $G_0(1,2)$ of

$$H_0 = \frac{p_1^2}{2m} + V_{ext}(\boldsymbol{r}_1) \qquad \text{(I-16)}$$

satisfies

$$i\hbar\partial_{t_1} G(1,2) - H_0(1)G(1,2) = \delta(r_1 - r_2)\delta(t_1 - t_2)\,. \qquad \text{(I-17)}$$

There are many different kinds of time-dependent Green's functions, but two of the most important one is retarded and advanced Green's function. Retarded and advanced Green's function is defined by

$$G(1,2) = \pm\frac{1}{i\hbar}U(1,2)\theta(\pm t)\,, \qquad \text{(I-18)}$$

where $U(1,2)$ is electron propagator. The upper and lower sign in Eq. (I-18) refers to retarded and advanced Green's function, respectively. In the energy space, Green's function in operator form G_0 of H_0 is

$$G_0 = (E - H_0)^{-1} = \sum_n \frac{|n_0\rangle\langle n_0|}{E - E_{n_0} + i\eta}\,, \qquad \text{(I-19)}$$

where $|n_0\rangle$ and E_{n_0} represent an eigenstate of H_0 and its energy, and η is a tiny positive (negative) real number for retarded (advanced) Green's function. As shown in Eq. (I-19), Green's function in the energy space shows eigenstate spectrum of H_0.

Using time-dependent perturbation theory which describes how propagator changes by perturbing Hamiltonian H_1, we can show that

$$G(1,2) = G_0(1,2) + \int d\boldsymbol{r}_3 dt_3 G_0(1,3)H_1(3)G(3,2) \qquad \text{(I-20)}$$

In energy space, Green's function (in operator form G) of a Hamiltonian (in operator form $H = H_0 + H_1$) satisfies

$$G^{-1} = G_0^{-1} - H_1\,. \qquad \text{(I-21)}$$

Eq. (I-21) shows how much eigenenergy changes due to H_1:

$$E_n = \sum_{n_0} E_{n_0} \left|\langle n_0 | n \rangle\right|^2 + \langle n | H_1 | n \rangle, \qquad \text{(I-22)}$$

where $|n\rangle$ and E_n represent an eigenstate of $H = H_0 + H_1$ and its eigenenergy.

In quantum field theory, time-ordered Green's function is important. In the coordinate space, time ordered Green's function of the Hamiltonian in Eq. (I-1) is

$$G(1,2) = \frac{1}{i\hbar} \frac{\langle \Psi_0 | T\left[\psi(1)\psi^\dagger(2)\right]_+ | \Psi_0 \rangle}{\langle \Psi_0 | \Psi_0 \rangle}. \qquad \text{(I-23)}$$

where $T[\ ]_+$ denotes time ordered product operator and $|\Psi_0\rangle$ is interacting ground state. From functional integration formalism as well as the formalism of canonically quantized field operators, the single-particle Green's function can be shown to satisfy

$$\mathrm{G}(\boldsymbol{r}_1, \boldsymbol{r}_2, E) = \mathrm{G}_0(\boldsymbol{r}_1, \boldsymbol{r}_2, E) + \int d\boldsymbol{r}_3 d\boldsymbol{r}_4 \, \mathrm{G}_0(\boldsymbol{r}_1, \boldsymbol{r}_3, E) \Sigma(\boldsymbol{r}_3, \boldsymbol{r}_4, E) \mathrm{G}(\boldsymbol{r}_4, \boldsymbol{r}_2, E) \quad \text{(I-24)}$$

in the energy space, where $\Sigma(\boldsymbol{r}, \boldsymbol{r}'', E)$ is electron self-energy due to electron-electron interaction in Eq. (I-3). There are various kinds of approximation to $\Sigma(\boldsymbol{r}, \boldsymbol{r}'', E)$ such as Hartree-Fock approximation and GW approximation. In the following subsection, I will review GW approximation.

(c) GW approximation to electron self-energy

Electron self-energy due to electron-electron interaction is composed of two different contributions from Hartree interaction and exchange-correlation. Electron self-energy due to Hartree interaction is originated from classical electrostatic interaction and can be represented by

$$\Sigma_H(\boldsymbol{r}_1, \boldsymbol{r}_2, E) = \int d\boldsymbol{r}_3 \frac{e^2}{|\boldsymbol{r}_1 - \boldsymbol{r}_3|} \rho(\boldsymbol{r}_3). \qquad \text{(I-25)}$$

Within GW approximation, electron self-energy due to exchange correlation is approximated by

$$\Sigma_{GW}(\boldsymbol{r}_1, \boldsymbol{r}_2, E) = iG(\boldsymbol{r}_1, \boldsymbol{r}_2, E) W(\boldsymbol{r}_1, \boldsymbol{r}_2, E) \qquad \text{(I-26)}$$

with

$$W(\mathbf{r}_1,\mathbf{r}_2,E)=\int d\mathbf{r}_3\,\epsilon^{-1}(\mathbf{r}_1,\mathbf{r}_3,E)V(\mathbf{r}_3,\mathbf{r}_2)\,, \qquad \text{(I-27)}$$

where $W(V)$ is screened (bare) Coulomb interaction and ϵ^{-1} is inverse dielectric function.

(d) Two particle correlation function and GW-BSE equation

The physical properties of excitons, correlated quasielectron-quasihole pair excitation, can be understood using two-particle correlation function:

$$L(1,2,1'2')=-G_2(1,2,1'2')+G_1(1,1')G_1(2,2') \qquad \text{(I-28)}$$

where

$$G_2(1,2,1'2')=\frac{1}{(i\hbar)^2}\frac{\langle\Psi_0|T[\psi(1)\psi(2)\psi^\dagger(2')\psi^\dagger(1')]_+|\Psi_0\rangle}{\langle\Psi_0|\Psi_0\rangle} \qquad \text{(I-29)}$$

is two particle Green's function and G_1 is single particle Green's function. From the "equation of motion method" [4], we can show that two particle correlation function satisfies

$$L(1,2,1'2')=G_1(1,2')\,\mathrm{G}_1(2,1')+\int d3456\;G(1,3)G(4,1')\Xi(3,5,4,6)L(6,2,5,2') \qquad \text{(I-30)}$$

in the coordinate space. The effective two particle interaction kernel Ξ is

$$\Xi(3,5,4,6)=\frac{\delta\Sigma(3,4)}{\delta G_1(6,5)}\,. \qquad \text{(I-31)}$$

Within GW approximation to the electron self-energy,

$$\Xi(3,5,4,6)=-i\delta(3,4)\delta(5^-6)V(3,6)+i\delta(3,6)\delta(4,5)W(3^+,4)\,, \qquad \text{(I-32)}$$

which is GW-BSE interaction kernel. If an exciton is assumed to be represented as $|S>=\sum_{cv\mathbf{k}}A^S_{cv\mathbf{k}}c^\dagger_{c\mathbf{k}}c_{v\mathbf{k}}\,|\Psi>$, we can determine the excitation energy spectrum of excitons by solving the GW-BSE equation (from the inversion of two particle correlation function in the energy space):

$$(E_c(\mathbf{k})-E_v(\mathbf{k}))A^S_{cv\mathbf{k}}+\sum_{c'v'\mathbf{k}'}<cv\mathbf{k}\,|\,\Xi\,|\,c'v'\mathbf{k}'>A^S_{c'v'\mathbf{k}'}=\Omega^S A^S_{cv\mathbf{k}}\,, \qquad \text{(I-33)}$$

where Ω^S is the exciton excitation energy, and $E_c(\boldsymbol{k})$ and $E_v(\boldsymbol{k})$ is quasiparticle energy.

3. Model Hamiltonian approach

(a) Extended Hubbard model

In solving Eq. (I-1), we don't need to treat all microscopic constituents as equally relevant degrees of freedom to predict the properties of low energy excitation. We may restrict our Hilbert space to a finite size which is spanning low energy electronic excitation such as quasi-particles and quasi-hole. In most materials, a few localized orbitals at each atomic sites are enough to evaluate electronic and optical properties of materials in the low energy-scale. In that case, Hamiltonian can be approximated by

$$\hat{H} = \sum_i E_i n_i + \sum_{i \neq j} \mathrm{t}_{ij} \mathrm{c}_i^\dagger \mathrm{c}_j + \frac{1}{2} \sum_{ij} V_{ij} n_i n_j \,, \qquad \text{(I-34)}$$

where i is the index indicating localized orbitals and $n_i = c_i^\dagger c_i$ is number operator on the i th orbital. Interaction parameters of E_i, t_{ij}, and V_{ij} are effective parameters with renormalized values due to the restriction of Hilbert space to a finite size.

(b) Anderson impurity model

Anderson impurity model [5] explains the occurrence of localized magnetic moments on strongly-localized orbitals dissolved in nonmagnetic metals by writing down the Hamiltonian:

$$H = \sum_{\boldsymbol{k}\sigma} E_{\boldsymbol{k}} n_{\boldsymbol{k}\sigma} + \sum_{\sigma} E_d n_{d\sigma} + \sum_{\boldsymbol{k}\sigma} V_{d\boldsymbol{k}} (c_{d\sigma}^\dagger c_{\boldsymbol{k}\sigma} + c_{\boldsymbol{k}\sigma}^\dagger c_{d\sigma}) + U n_{d,\uparrow} n_{d,\downarrow} \,, \qquad \text{(I-35)}$$

where $\boldsymbol{k}$ indicates a free-electron state at crystal momentum $\boldsymbol{k}$ and d indicates localized impurity orbital. The last term in Eq. (I-35) is the repulsive energy among the d orbital due to Coulomb interaction. Electron in this Hamiltonian is allowed to hop between metal orbital and impurity d orbital. Within self-consistent Hartree-Fock approximation in which many-body ground states are represented by a single Slater-determinant, the expectation value of electron density associated with the impurity d orbital is given by

$$\left\langle n_{d,\sigma} \right\rangle = \frac{1}{\pi} \int_{-\infty}^{E_F} dE \, \frac{\Delta_d}{(E - E_{d,\sigma})^2 + {\Delta_d}^2} \,, \qquad \text{(I-36)}$$

where $E_{d,\sigma} = E_d + U\left\langle n_{d,-\sigma}\right\rangle$, $\Delta_d = \pi\left\langle\left|V_{k,d}\right|^2\right\rangle NV$, N is metal electron density of state and V is the volumes of the system.

II. Nanostructures

1. Optical oscillator strength of excitons in semiconducting single-walled carbon nanotubes

(a) Introduction

A single-walled carbon nanotube (SWCNT) is a graphene strip of nanometer width rolled width-wise into a seamless cylinder [6,7]. The optical properties of SWCNTs have attracted much attention since they are tunable by changing the SWCNT's geometrical structure (i.e., the width and orientation of the graphene strip) [8] and are of significant potential in applications such as light-emitting diodes [9], photo-detectors [10] and other optoelectronic devices. Because of strong many-electron interactions in reduced dimensional system, the dominant features of the optical properties of SWCNTs can only be understood in terms of exciton excitations (as opposed to interband transitions) [11–13]. For one-particle (quasiparticle) excitations in SWCNTs, confinement of the electron wavefunction along the tube circumference quantizes the wavelength (or equivalently the crystal momentum) of the quasiparticles along that direction, resulting in only discrete sets of wavevectors (or **k** points) in the two-dimensional Brillouin zone (BZ) of graphene allowable for the SWCNTs. Electronic states from these allowed **k** points (the cutting-lines labeled with index P) shown in Figure II-1b give rise to the SWCNT electronic subbands [14]. In optical processes, the photo-excited quasielectron in the conduction band and the quasihole left behind in the valence band interact with each other forming excitons with excitation energies lower than the inter-subband transition energies, as schematically shown in Figure II-1c, giving rise to large exciton binding energies. The explicit dependence of exciton oscillator strength on diameter d, chiral angle θ, and subband index P (the so-called family behavior) is yet unclear, in contrast to, for example, that of exciton excitation energies [8,15–18]. Although the first-principles GW plus Bethe-Salpeter Equation (GW-BSE) approach [19,20] for treating electron-hole interactions and optical response [4,21] has successfully predicted the optical properties of SWCNTs including oscillator strengths, its application is so far limited to achiral and smaller diameter nanotubes, owing to the rather heavy computational cost of the calculations. An effective model Hamiltonian approach with reliable many-electron interaction parameters, such as an extended Hubbard model, would provide an efficient means to arrive at such a formula. In this approach, the interactions between electrons are limited to a physically relevant, restricted Hilbert space, and the screening effects of configurations outside of the restricted Hilbert space are taken into account using effective Coulomb interaction parameters. Such approaches had been tried, [18,22] but difficulties were encountered in obtaining physically well-based effective interaction parameters in the past.

Here, we apply an extended Hubbard Hamiltonian to the optical properties of SWCNTs with three geometrical-structure-independent parameters that are fixed by results from *ab initio* GW-BSE calculations. These parameters are obtained by fitting twenty physical quantities (quasiparticle energy gaps and exciton excitation energies of 4 achiral nanotubes) from our extended Hubbard model study to those from the *ab initio* calculations of the real systems using

the BerkeleyGW code [23]. In both the extended Hubbard model and *ab initio* studies, we employed the same approximations to the electron self energy [19,21] for quasiparticle excitations energy and to the BSE interaction kernel for the optical excitation energies of excitons [4,20]. The idea is to fit enough number of relevant physical quantities affected by many-electron interaction, to pin down the effective electron-electron interactions in the model Hamiltonian so that it is applicable to nanotubes of any arbitrary structure.

(b) Theory and computation

We chose for our full *ab initio* calculations of the real systems four SWCNTs -- one small diameter tube and one large diameter tube in each of the two types of semiconducting (n, m) SWCNTs classified by (n-m) modulo 3 equal to 1 or 2: the (10,0), (14,0), (16,0) and (17,0) nanotubes. We calculated the ground-state properties of the SWCNTs using density functional theory in the local density approximation (DFT-LDA) in a supercell geometry with a tube-tube separation of 36, 50.7, 57.9, and 61.2 in atomic units (a.u.) for the (10, 0), (14, 0), (16, 0), and (17, 0) SWCNTs, respectively. Norm-conserving pseudopotentials were used with a plane wave basis (60 Ry cutoff). For the DFT-LDA calculation, we sampled 32 k points in the BZ along the tube axial direction. We then calculated the quasiparticle energies within the GW approximation [19,21,23]: $\Sigma = iGW$ where G is the electron Green′s function and W is screened Coulomb interaction. The frequency-dependence of the dielectric screening matrix is obtained from the static dielectric matrix employing a generalized plasmon pole model [19]. For the GW calculations, we used a cutoff parameter of 9, 6, 6, and 6 Ry for the dielectric matrix and a cutoff parameter of 390, 376, 488, and 500 bands for the evaluation of the dielectric screening matrix and self-energy operator, for the (10, 0), (14, 0), (16, 0), and (17, 0) SWCNTs, respectively.

The optical excitation spectrum is then calculated. The exciton states can be represented, in occupation number representation, as

$$| S >= \sum_{cv\mathbf{k}} A^S_{cv\mathbf{k}} c^\dagger_{c\mathbf{k}} c_{v\mathbf{k}} | 0 > \qquad \text{(II-1)}$$

within the Tamm-Dancoff approximation. $A^S_{cv\mathbf{k}}$ is the electron-hole pair amplitude obtained by solving the GW-BSE equation [4,20],

$$(E_c(\mathbf{k}) - E_v(\mathbf{k}))A^S_{cv\mathbf{k}} + \sum_{c'v'\mathbf{k}'} < cv\mathbf{k} | K^{\text{int}} | c'v'\mathbf{k}' > A^S_{c'v'\mathbf{k}'} = \Omega^S A^S_{cv\mathbf{k}} \qquad \text{(II-2)}$$

where Ω^S is the exciton excitation energy and K^{int} is the quasielectron-quasihole interaction kernel. There are two distinct terms in K^{int}: i) an attractive direct interaction K^{int}_D - an electron-hole pair scatters to another pair via the screened Coulomb interaction between the negatively charged electron and the positively charged hole; ii) a repulsive exchange interaction via the

bare Coulomb interaction K_{ex}^{int}. For the interaction kernel, we used up to 256 k-points along the tube axis direction and 10 valence and 10 conduction bands. A truncated Coulomb interaction is used in the GW-BSE calculations to prevent interaction with nanotubes in neighboring supercells [23,24]. The details of the methodology may be found in Refs. 14 and 15.

Next, the effective model Hamiltonian is constructed with one p_z orbital at each carbon atom:

$$H = \sum_{\substack{<i,j> \\ \sigma=\{\uparrow,\downarrow\}}} t_{ij} c_{i,\sigma}^{\dagger} c_{j,\sigma} + \frac{1}{2} \sum_{\substack{i,j \\ \sigma,\sigma'=\{\uparrow,\downarrow\}}} V_{ij} n_{i\sigma} n_{j\sigma'} \qquad \text{(II-3)}$$

where $c_{i\sigma}^{\dagger}$, $c_{i\sigma}$, and $n_{i\sigma}$ are the electron creation, annihilation, and number operators at the site i with spin σ respectively. The curvature of the nanotube tilts the p_z orbitals as shown in Figure II-1d, which are originally parallel to each other in planar graphene. Curvature shifts the position of the Dirac point of graphene from the K and K′ point of the Brillouin zone, leading to a curvature gap at the charge neutrality energy for small diameter metallic nanotubes except for the armchair nanotubes [25]. The nearest-neighbor hopping integral, t_{ij}, between the p_z orbitals (aligned normal to the surface in graphene) at sites i and j may be modeled to incorporate the curvature effect in the following form [25]:

$$t_{ij} = t_{\pi\pi}(\mathbf{n}_i - \mathbf{n}_i \cdot \hat{\mathbf{R}}_{ij} \hat{\mathbf{R}}_{ij}) \cdot (\mathbf{n}_j - \mathbf{n}_j \cdot \hat{\mathbf{R}}_{ij} \hat{\mathbf{R}}_{ij}) + t_{\sigma\sigma}(\mathbf{n}_i \cdot \hat{\mathbf{R}}_{ij} \mathbf{n}_j \cdot \hat{\mathbf{R}}_{ij}) \qquad \text{(II-4)}$$

where $t_{\pi\pi}$ and $t_{\sigma\sigma}$ are the hopping integrals between two p orbitals side-by-side and end-to-end, respectively, $\mathbf{n}_i$ is

$$V_{ij} = \frac{1}{\sqrt{(|\mathbf{R}_i - \mathbf{R}_j| / e^2)^2 + 1/U^2}} \qquad \text{(II-5)}$$

the surface normal unit vector, and $\hat{\mathbf{R}}_{ij} = (\mathbf{R}_j - \mathbf{R}_i)/|\mathbf{R}_j - \mathbf{R}_i|$ where $\mathbf{R}_i$ is the carbon atom position vector as shown in Figure II-1d. The bare Coulomb interaction between two electrons is modeled in the form of an Ohno potential [26], in CGS unit, and U is a Coulomb potential regularization parameter. Although our model given by Eq. (II-3) does not incorporate all possible many-electron interaction terms in the exact many- body Hamiltonian for the SWCNT, we include the dominant terms when an atom-centered basis set spans the Hilbert space [27].

To calculate the quasiparticle energies for our extended Hubbard model Hamiltonian, we use also the DFT-LDA results from the model as the mean-field starting point [28]. We use the full symmetry of the SWCNT including the screw translations, so that there are only two atoms per unit cell for any (n,m) tubes; and there is no need for a supercell geometry. In the local density approximation, the exchange-correlation potential is then a function of site occupation. Since geometrical relaxation is included in the hopping integrals t_{ij} effectively and

site occupation is assumed to be uniform within our model, the inclusion of a LDA exchange-correlation functional doesn't change the band dispersion from the tight-binding band dispersion given by the first term in Eq. (II-3).

We evaluated Σ in the GW approximation (as for the case of the real systems) using the generalized plasmon pole approximation to the screening of the Coulomb interaction in contrast to a previous model study in which a further approximation of the static COHSEX approximation to GW self energy is employed [18]. The static COHSEX approximation is known to overestimate the electron self-energy [19]. Additionally, we represent the Coulomb interaction and the longitudinal polarization function as 2×2 matrices at each momentum $\mathbf{q}$ and frequency ω. This is needed since we have two p_z orbitals in a unit cell in our Hilbert space. Furthermore, in contrast to a previous study [18], we did not include a constant renormalization factor to the bare Coulomb interaction, a factor that was attributed by the authors in Ref. 13 to additional screening from electronic states outside of the Hilbert space. We argue that this renormalization factor in the SWCNT should be unity in the long wavelength (q small) limit, which is appropriate for excitons in SWCNTs since they have large radius. This arises from the fact that, due to the 1D character of the SWCNTS, the longitudinal polarizability from the other electronic states multiplied by the bare Coulomb interaction goes to zero in the $q \to 0$ limit [31].

We calculated the electron self-energy (Σ) correction to the mean-field solution within the GW approximation [21]. Within our model of Eq. (II-3), the longitudinal polarizability matrix at momentum $\mathbf{q}$ in the static limit is

$$\chi^0_{\tau,\tau'}(\mathbf{q},\omega=0) = \frac{2}{N}\sum_{n,m,\mathbf{k}} \beta_{n\tau}(\mathbf{k})\beta^*_{m\tau}(\mathbf{k}+\mathbf{q})\beta^*_{n\tau'}(\mathbf{k})\beta_{m\tau'}(\mathbf{k}+\mathbf{q}) \times \frac{f(E^0_m(\mathbf{k}+\mathbf{q})) - f(E^0_n(\mathbf{k}))}{E^0_m(\mathbf{k}+\mathbf{q}) - E^0_n(\mathbf{k})} \quad \text{(II-6)}$$

where τ is the basis atom index in the 2-atom unit cell of SWCNT, N is the number of 2-atom unit cell in our system, $\beta_{n\tau}(\mathbf{k})$ is the DFT-LDA Kohn-Sham orbital coefficient in the basis of the p_z orbitals, $E^0_n(\mathbf{k})$ is the Kohn-Sham orbital energy, and $f(E)$ is the Fermi-Dirac distribution function. The screened Coulomb interaction matrix W in the static limit is

$$\tilde{W}(\mathbf{q},\omega=0) = (\tilde{1} - \tilde{V}(\mathbf{q})\tilde{\chi}^0(\mathbf{q},\omega=0))^{-1}\tilde{V}(\mathbf{q}) \,. \quad \text{(II-7)}$$

with the bare Coulomb interaction matrix denoted as

$$V_{\tau,\tau'}(\mathbf{q}) = \sum_{\mathbf{R}} V(\mathbf{R}+\boldsymbol{\tau}-\boldsymbol{\tau}')e^{-i\mathbf{k}\cdot(\mathbf{R}+\boldsymbol{\tau}-\boldsymbol{\tau}')} \quad \text{(II-8)}$$

Here the "~" symbol denotes that the quantities are 2×2 matrices. In order to extend the static screened Coulomb interaction in the model calculation to nonzero frequencies, we made also

use of a generalized plasmon pole (GPP) model [19,29,30]. We express the screened Coulomb interaction in its eigen-representation $\tilde{W}_n(\mathbf{q},\omega)$:

$$W_{\tau,\tau'}(\mathbf{q},\omega) = \sum_n D_{\tau n}(\mathbf{q}) W_n(\mathbf{q},\omega) D^{-1}_{n\tau'}(\mathbf{q}) \qquad \text{(II-9)}$$

where $\tilde{D}(\mathbf{q})$ is a matrix formed from the outerproduct of the eigenvectors of the static $\tilde{W}(\mathbf{q})$. Due to the restriction of Hilbert space to two p_z orbital in the two-atom unit cell, we have only two longitudinal modes of excitation. Then, $\tilde{W}(\mathbf{q})$ have eigenvalues of the form

$$W_n(\mathbf{q},\omega) = V_n(\mathbf{q}) + \frac{B_n(\mathbf{q})}{\omega - \omega_n(\mathbf{q}) + i\eta} - \frac{B_n(\mathbf{q})}{\omega + \omega_n(\mathbf{q}) - i\eta}, \quad \text{(II-10)}$$

in Lehmann′s representation where

$$V_n(\mathbf{q}) = (\tilde{D}^{-1}(\mathbf{q})\tilde{V}(\mathbf{q})\tilde{D}(\mathbf{q}))_{nn} \quad \text{(II-11)}$$

and n = 1 or 2. The parameters $B_n(\mathbf{q})$ and $\omega_n(\mathbf{q})$ are chosen such that $\tilde{W}(\mathbf{q},\omega)$ reproduces the static screened Coulomb interaction in the static limit, and $\tilde{W}(\mathbf{q},\omega)$ satisfies the sum rules derived from the longitudinal *f*-sum rules for imaginary part of retarded polarization matrix within an extended Hubbard model:

$$\begin{aligned}
&\int_{-\infty}^{\infty} \mathrm{Im}\,\chi^R_{\tau,\tau'}(\mathbf{q},\omega)\omega\, d\omega = \\
&-\frac{\pi}{N}\sum_{\mathbf{k}\sigma}\left(t(\mathbf{k}+\mathbf{q})_{\tau,\tau'} \left\langle 0\middle| c^\dagger_{\tau\sigma}(\mathbf{k}) c_{\tau'\sigma}(\mathbf{k}) \middle|0\right\rangle + t(\mathbf{k}-\mathbf{q})_{\tau',\tau} \left\langle 0\middle| c^\dagger_{\tau'\sigma}(\mathbf{k}) c_{\tau\sigma}(\mathbf{k}) \middle|0\right\rangle \right) \quad \text{(II-12)} \\
&+\frac{\pi}{N}\sum_{\mathbf{k}\sigma\tau_1}\left(t(\mathbf{k})_{\tau,\tau_1} \left\langle 0\middle| c^\dagger_{\tau\sigma}(\mathbf{k}) c_{\tau_1\sigma}(\mathbf{k}) \middle|0\right\rangle + t(\mathbf{k})_{\tau_1,\tau} \left\langle 0\middle| c^\dagger_{\tau_1\sigma}(\mathbf{k}) c_{\tau\sigma}(\mathbf{k}) \middle|0\right\rangle \right)\delta_{\tau,\tau'}
\end{aligned}$$

where

$$t_{\tau,\tau'}(\mathbf{k}) = \sum_{\mathbf{R}} t(\mathbf{R}+\boldsymbol{\tau}-\boldsymbol{\tau}') e^{-i\mathbf{k}\cdot(\mathbf{R}+\boldsymbol{\tau}-\boldsymbol{\tau}')}. \quad \text{(II-13)}$$

For example, for a system with one s orbital in the unit cell of a simple cubic lattice,

$$\int_{-\infty}^{\infty} \mathrm{Im}\,\chi^R(\mathbf{q},\omega)\omega\, d\omega = -2\pi\sum_{\mathbf{k}}^{occ}\left(t(\mathbf{k}+\mathbf{q}) + t(\mathbf{k}-\mathbf{q}) - 2t(\mathbf{k}) \right)/N. \qquad \text{(II-14)}$$

In the continuum limit, $t(\mathbf{k})$, which is the eigen-energy of the noninteracting Hamiltonian, corresponds to kinetic energy $\hbar^2 k^2 / 2m$ in the jellium model and $-2\pi \sum_{\mathbf{k}}^{occ} \left(t(\mathbf{k}+\mathbf{q}) + t(\mathbf{k}-\mathbf{q}) - 2t(\mathbf{k}) \right) / N$ is (analogous to that of jellium model with electron density of n) $-\pi n q^2 / 2m$. The Coulomb-hole (COH) and screened exchange (SEX) term of the electron self-energy [19] within the GW approximation is then given by

$$\Sigma_n^{SEX}(\mathbf{q},\omega) = -\frac{1}{N} \sum_{m\mathbf{k}}^{occ} \sum_{\tau_1 \tau_2} \beta_{n\tau_1}^*(\mathbf{q}) \beta_{m\tau_1}(\mathbf{k}) \beta_{m\tau_2}^*(\mathbf{k}) \beta_{n\tau_2}(\mathbf{q})$$
$$\times \left[V_{\tau_1,\tau_2}(\mathbf{q}-\mathbf{k}) + \sum_s D_{\tau_1 s}(\mathbf{q}-\mathbf{k}) B_s(\mathbf{q}-\mathbf{k}) D_{s\tau_2}^{-1}(\mathbf{q}-\mathbf{k}) \right. \qquad \text{(II-15)}$$
$$\left. \times \left(P \frac{1}{\omega - E_m^0(\mathbf{k}) - \omega_s(\mathbf{q}-\mathbf{k})} - P \frac{1}{\omega - E_m^0(\mathbf{k}) + \omega_s(\mathbf{q}-\mathbf{k})} \right) \right]$$

and

$$\Sigma_n^{COH}(\mathbf{q},\omega) = \frac{1}{N} \sum_{m\mathbf{k}} \sum_{\tau_1 \tau_2} \beta_{n\tau_1}^*(\mathbf{q}) \beta_{m\tau_1}(\mathbf{k}) \beta_{m\tau_2}^*(\mathbf{k}) \beta_{n\tau_2}(\mathbf{q})$$
$$\times \left[\sum_s D_{\tau_1 s}(\mathbf{q}-\mathbf{k}) B_s(\mathbf{q}-\mathbf{k}) D_{s\tau_2}^{-1}(\mathbf{q}-\mathbf{k}) \left(P \frac{1}{\omega - E_m^0(\mathbf{k}) - \omega_s(\mathbf{q}-\mathbf{k})} \right) \right]. \qquad \text{(II-16)}$$

The quasiparticle energy is, denoting the renormalization factor

$$Z_n(\mathbf{q}) = \left(1 - \mathrm{Re} \frac{\partial \Sigma_n(\mathbf{q},\omega)}{\partial \omega} \right)^{-1}_{\omega = E_n^0(\mathbf{q})}, \qquad \text{(II-17)}$$

given by

$$E_n(\mathbf{q}) = E_n^0(\mathbf{q}) + Z_n(\mathbf{q}) Re \Delta\Sigma_n(\mathbf{q}, E_n^0(\mathbf{q})) \qquad \text{(II-18)}$$

where

$$\Delta\Sigma_n(\mathbf{q}, E_n^0(\mathbf{q})) = \Sigma_n^{GW}(\mathbf{q}, E_n^0(\mathbf{q})) - \Sigma_n^{DFT}(\mathbf{q}, E_n^0(\mathbf{q})) \qquad \text{(II-19)}$$

with $\Sigma_n^{GW}(\mathbf{q}, E_n^0(\mathbf{q})) = \Sigma_n^{COH}(\mathbf{q}, E_n^0(\mathbf{q})) + \Sigma_n^{SEX}(\mathbf{q}, E_n^0(\mathbf{q}))$ and $\Sigma_n^{DFT}(\mathbf{q}, E_n^0(\mathbf{q}))$ is the DFT exchange-correlation energy [28].

The optical excitations are then calculated for our extended Hubbard Hamiltonian within the Tamm-Dancoff approximation to the Bethe-Salpeter equation, similar to the discussion for the *ab initio* calculations above. Following Rohlfing and Louie [20], the direct electron-hole interaction term is

$$< cv\mathbf{k} \mid K_D \mid c'v'\mathbf{k}' >= -\frac{1}{N}\sum_{\tau_1\tau_2} \beta^*_{c\tau_1}(\mathbf{k})\beta_{c'\tau_1}(\mathbf{k}')\beta_{v\tau_2}(\mathbf{k})\beta^*_{v'\tau_2}(\mathbf{k}') \times W_{\tau_1,\tau_2}(\mathbf{k}-\mathbf{k}', \omega = 0) \qquad \text{(II-20)}$$

and the exchange electron-hole interaction term is

$$< cv\mathbf{k} \mid K_{ex} \mid c'v'\mathbf{k}' >= \frac{1}{N}\sum_{\tau_1\tau_2} \beta^*_{c\tau_1}(\mathbf{k})\beta_{c'\tau_2}(\mathbf{k}')\beta_{v\tau_1}(\mathbf{k})\beta^*_{v'\tau_2}(\mathbf{k}') \times V_{\tau_1,\tau_2}(0, \omega = 0). \qquad \text{(II-21)}$$

From the solutions of the BSE (Eq. (II-2)), optical transition oscillator strength to creating an exciton in state |S> is given by [32]

$$f^S = \frac{2m \mid< 0 \mid \mathbf{v}\cdot\hat{\mathbf{e}} \mid S >\mid^2}{\Omega^S} \qquad \text{(II-22)}$$

where $\hat{\mathbf{e}}$ is the polarization direction of light, $\mathbf{v}$ is electron velocity operator, |0> is the ground state of the SWCNT, m is the mass of the electron, and Ω^S is the exciton excitation energy. The velocity matrix elements for the *ab initio* calculation is computed through the following relation using the generalized Hellmann-Feynman theorem [33]

$$
\begin{aligned}
&< 0 \,|\, \mathbf{v}\cdot\hat{\mathbf{e}} \,|\, S > \\
&= < 0 \,|\, [\mathbf{x}, \hat{H}] \,|\, S > \cdot\hat{\mathbf{e}} / i\hbar \\
&= < 0 \,|\, \mathbf{x} \,|\, S > \cdot\hat{\mathbf{e}}\ \Omega^S / i\hbar \\
&= \sum_{cv\mathbf{k}nq\mathbf{q}m\mathbf{p}} A^S_{cv\mathbf{k}} \int \psi^{\dagger}_{nq}\mathbf{x}\cdot\hat{\mathbf{e}}\ \psi_{m\bar{p}} d\mathbf{x} < 0 \,|\, c^{?}_{n\mathbf{q}} c_{m\mathbf{p}} c_{c\mathbf{k}} c_{v\mathbf{k}} \,|\, 0 > \Omega^S / i\hbar \\
&= \sum_{cv\mathbf{k}} A^S_{cv\mathbf{k}} \int \psi^*_{v\mathbf{k}}(\mathbf{x})\mathbf{x}\cdot\hat{\mathbf{e}}\psi_{c\mathbf{k}}(\mathbf{x}) d\mathbf{x}\ \Omega^S / i\hbar \\
&= \sum_{cv\mathbf{k}} A^S_{cv\mathbf{k}} \int \psi^*_{v\mathbf{k}}(\mathbf{x})[\mathbf{x}\cdot\hat{\mathbf{e}}, H^{qp}]\psi_{c\mathbf{k}}(\mathbf{x}) d\mathbf{x}\ \Omega^S / (E_{c\mathbf{k}} - E_{v\mathbf{k}}) i\hbar \\
&= \sum_{cv\mathbf{k}} A^S_{cv\mathbf{k}} \int u^*_{v\mathbf{k}}(\mathbf{x})[\mathbf{x}\cdot\hat{\mathbf{e}}, e^{-i\mathbf{k}\cdot\mathbf{x}} H^{qp} e^{i\mathbf{k}\cdot\mathbf{x}}] u_{c\mathbf{k}}(x) d\mathbf{x}\ \Omega^S / (E_{c\mathbf{k}} - E_{c\mathbf{k}}) i\hbar \\
&= \sum_{cv\mathbf{k}} A^S_{cv\mathbf{k}} \int u^*_{v\mathbf{k}}(\mathbf{x})\hat{\mathbf{e}}\cdot\nabla_{\mathbf{k}}(e^{-i\mathbf{k}?\mathbf{x}} H^{qp} e^{i\mathbf{k}\ \mathbf{x}}) u_{c\mathbf{k}}(x) d\mathbf{x}\ \Omega^S / (E_{v\mathbf{k}} - E_{c\mathbf{k}}) \hbar \\
&= \sum_{cv\mathbf{k}} A^S_{cv\mathbf{k}} \hat{\mathbf{e}}\cdot\left(\int \nabla_{\mathbf{k}} u^*_{c\mathbf{k}}(\mathbf{x}) u_{v\mathbf{k}}(\mathbf{x}) d\mathbf{x} - \int u^*_{c\mathbf{k}}(\mathbf{x})\nabla_{\mathbf{k}} u_{v\mathbf{k}}(\mathbf{x}) d\mathbf{x} \right) \Omega^S / 2\hbar
\end{aligned}
\qquad \text{(II-23)}
$$

where H^{qp} is the quasiparticle Hamiltonian for which $\psi_{v\mathbf{k}}(\mathbf{x})$ and $\psi_{c\mathbf{k}}(\mathbf{x})$ are the Bloch eigenstates with energy of $E_{v\mathbf{k}}$ and $E_{c\mathbf{k}}$. $u_{v\mathbf{k}}(\mathbf{x})$ and $u_{c\mathbf{k}}(\mathbf{x})$ are the periodic parts of the Bloch eigenstates and $\mathbf{x}$ is position operator. For the extended Hubbard model, it is as follows

$$
< 0 \,|\, \mathbf{v}\cdot\hat{\mathbf{e}} \,|\, S > = \sum_{cv\mathbf{k}} A^S_{cv\mathbf{k}} \sum_{\tau} \hat{\mathbf{e}}\cdot\left(\nabla_{\mathbf{k}} \beta^*_{c\tau}(\mathbf{k}) \beta_{v\tau}(\mathbf{k}) - \beta^*_{c\tau}(\mathbf{k}) \nabla_{\mathbf{k}} \beta_{v\tau}(\mathbf{k}) \right) \Omega^S / 2\hbar. \qquad \text{(II-24)}
$$

This procedure is exactly at the same level of approximation as the *ab initio* GW-BSE calculation for the real SWCNT systems.

(c) Results and discussion

We tuned the model parameters until we minimize the differences between the model and *ab initio* results of the four SWCNTs considered within the GW-BSE approach for: i) the quasiparticle excitation gap and the 1u and 3u exciton excitation energies of the P=1 subband transitions, and ii) the quasiparticle excitation gap and the 1u exciton excitation energy of the P=2 subband transitions. The optimized effective interaction parameters for our extended Hubbard Hamiltonian are: $t_{\pi\pi}$ = -2.69 eV, $t_{\sigma\sigma}$ = 3.04 eV, and U = 3.87 eV. The 20 excitation energies of the 4 SWCNTs considered from the extended Hubbard Hamiltonian with the above parameters match those from the *ab initio* GW-BSE calculations to within 0.06 eV

Figure II-2 shows the imaginary part of the polarizability per tube, $\alpha(E)$, for the (10,0) and (14,0) SWCNTs, from both the *ab initio* and model calculations with light polarization

along the tube axis. In an *ab initio* calculation using a supercell geometry [13], $\alpha(E)$ is obtained from the calculated dielectric function $\epsilon(E)$ by the relation

$$\alpha(E) = \mathrm{Im}(A^{cs}(\epsilon(E)-1)/4\pi), \qquad \text{(II-25)}$$

where A^{cs} is the supercell cross-sectional area perpendicular to the nanotube axis. To compare with experiment, the imaginary part of the polarizability of a system consisting of identical nanotubes would be the area density of the tubes multiplied by $\alpha(E)$. The imaginary part of the polarizability per tube is related to the optical oscillator strength by

$$\alpha(E) = \sum_S \frac{\pi\hbar^2 e^2}{mEL} f^S \delta(E-\Omega^S) \qquad \text{(II-26)}$$

where m is the mass of the electron, e is the charge of electron *,* L is the length of the SWCNT and f^S is the optical transition oscillator strength of the excited state $|S>$. The oscillator strength is defined as [32]

$$f^S = \frac{2m|<0|\mathbf{v}\cdot\hat{\mathbf{e}}|S>|^2}{\Omega^S} \qquad \text{(II-27)}$$

where $\hat{\mathbf{e}}$ is the polarization direction of light, $\mathbf{v}$ is electron velocity operator and |0> is the ground state of the SWCNT. We sampled $\alpha(E)$ at 0.01 eV steps and convoluted the results with a 0.025 eV Gaussian broadening. Note that, although we tuned the effective interaction parameters to fit only the exciton excitation energies and the quasiparticle gaps, the resulting oscillator strengths match to within 10 % of the *ab initio* results without further adjustment. Within the energy gap of one inter-subband transition, there can be several different exciton states. For example, below the onset of the P=1 inter-subband transition, we have the 1u, 2g, 3u, ... singlet exciton states, which are odd, even, and odd with respect to inversion [34] for the first three states, respectively; but only the odd symmetry states are optically active for the light polarization considered here. As found in previous studies [12], the 1u excitons have the biggest oscillator strength and basically dominate the spectrum at the onset of each inter-subband transition. This characteristic originates from the 1-dimensional character of the SWCNTs. For example, for an 1-dimensional hydrogenic system with an attractive $1/|x|$ potential, only the 1s state has nonzero amplitude at the origin [35]; thus, for dipole allowed transitions, only the 1u exciton is optically active and the oscillator strength is concentrated all in 1u state or the lowest energy excited state.

Figure II-3a shows the family behavior of the optical excitation energies as a function of inverse diameter in the so called Kataura plot for SWCNTs from our theory and those from experiments [36–38]. In the energy range of 0-2.5 eV, the theoretical and experimental results agree with each other to within ~0.1eV, without any adjustable parameters from experiment. Figure II-3b compares the calculated oscillator strength per atom with experiments. Among the

21 different isolated single-walled carbon nanotubes measured by the Wang group [39], there is very good agreement between theory and experiment, especially in view of the difficulty in deducing the absolute absorption cross-sections from experiment. The apparently systematic overestimation of theory as compared to experiment may arise from several factors, including the simplicity of the model Hamiltonian used, uncertainties in the background subtraction of experimental data, and possible doping of the measured semiconducting SWCNTs. Screening from the doped carriers would reduce electron-hole interactions, resulting in a decrease in both the exciton binding energy and oscillator strength.

From our calculations, the oscillator strength per atom, f_s/N_a, of the 1u singlet excitons in the semiconducting SWCNTs is found to follow the formula,

$$\frac{f_S}{N_a} = \frac{G(1+J\xi cos(3\theta)\mathrm{P}/d)}{(\mathrm{P}+\mathrm{Q})d}, \quad \text{(II-28)}$$

where G, J, and Q are structure-independent parameters having the values of G=0.29 nm, J=0.047 nm and Q=7.5, and $\xi = (-1)^{mod(n-m,3)+2\mathrm{P}/3+\mathrm{mod}(\mathrm{P},3)/3}$. The physical origin of the form of the analytical formula above may be understood as follows. The exciton states can be viewed to a good approximation, in occupation number representation, as $|S>=\sum_{cv\mathbf{k}} A^S_{cv\mathbf{k}} c^\dagger_{c\mathbf{k}} c_{v\mathbf{k}} |0>$ where $A^S_{cv\mathbf{k}}$ is the electron-hole pair amplitudes that are obtained by solving the Bethe-Salpeter equation of the two-particle Green′s function [4,20]. From the *ab initio* calculations [12], an exciton in the energy gap of a particular P inter-subband transition is shown to be composed of basically free electron-hole pair configurations concentrated near the subband edges at $\pm\mathbf{k_0}$ (as marked by the blue circles in Figure II-1b) since the exciton extent is large compared to the inter-atomic distance. Thus the exciton velocity matrix element square per carbon atom, $|<0|\hat{\mathbf{v}}\cdot\mathbf{e}|S>|^2/N_a$, can be approximated as $2|<c\mathbf{k_0}|\hat{\mathbf{v}}|v\mathbf{k_0}>\cdot\hat{e}|^2|F(x=0)|^2 L/N_a$, where F is the exciton envelope function in real space ($F(x)=\sum_k A^S_{cvk}\, e^{ikx}/\sqrt{L}$ with x is a vector along the tube axial direction.). $|F(x=0)|^2$ is the probability density to find the excited electron and the created hole at the same location, and L is the length of the nanotube. The envelope function of the 1-dimensional 1u exciton of semiconducting SWCNTs, $F(x)$, has been shown to be well approximated by a Gaussian function [16], so that $|F(x=0)|^2=\frac{1}{\sqrt{2\pi}r_o}$ where r_0 is the exciton radius. From the facts that (i) $L/N \propto 1/d$, (ii) the exciton size scaling relation [40,41] of $r_0 \propto d\left(1+\frac{T}{p}\right)$ with *T,* a constant from our model, (iii) the interband velocity matrix elements $<c\mathbf{k_0}|\hat{\mathbf{v}}|v\mathbf{k_0}>\cdot\hat{\mathbf{e}} \propto Y+\xi cos(3\theta)\mathrm{P}/d$ with *Y* a constant from our model, and (iv) the exciton excitation energy scaling law[26] of $\Omega \propto \frac{\mathrm{P}}{d}\left(Z-\xi cos(3\theta)\frac{\mathrm{P}}{d}\right)$ with *Z* a constant, one obtains the

above formula (Eq. (II-28)) for the oscillator strength per atoms, to first order in $cos(3\theta)$. Figure II-4 shows f_s/N_a from 160 carbon nanotubes, comparing the calculated results with the formula given by Eq. (II-28). As predicted, f_s/N_a follows accurately the explicit formula with three structure-independent parameters. For tubes that are not isolated, an additional environmental polarizability, χ_{en}, is expected to change Q to $Q(1+4\pi\chi_{en})$, since it is known that χ_{en} increase the exciton size to $r_0 \propto d\left(1+\frac{Q}{p}(1+4\pi\chi_{en})\right)$ [40]. Environmental screening effect on the exciton excitation energies is typically very small due to a cancellation of electron self-energy correction and exciton binding energy [12,36], but it may be larger on the oscillator strengths.

(d) Conclusion

In summary, we have calculated the excitation energies and optical oscillator strength of excitons in semiconducting SWCNTs with the *ab initio* GW-BSE approach and in an extended Hubbard model using three parameters derived from the *ab initio* GW-BSE calculations. Our calculated results explain quantitatively recent experimental measurements. Moreover, we have obtained an explicit formula for the oscillator strength, and its family behavior, of the dominant excitation (the 1u singlet excitons of each inter-subband transition) of semiconducting SWCNTs of arbitrary structure under different environments. This formula should be useful in interpreting experiments and in guiding designs of optical and optoelectronic devices using carbon nanotubes.

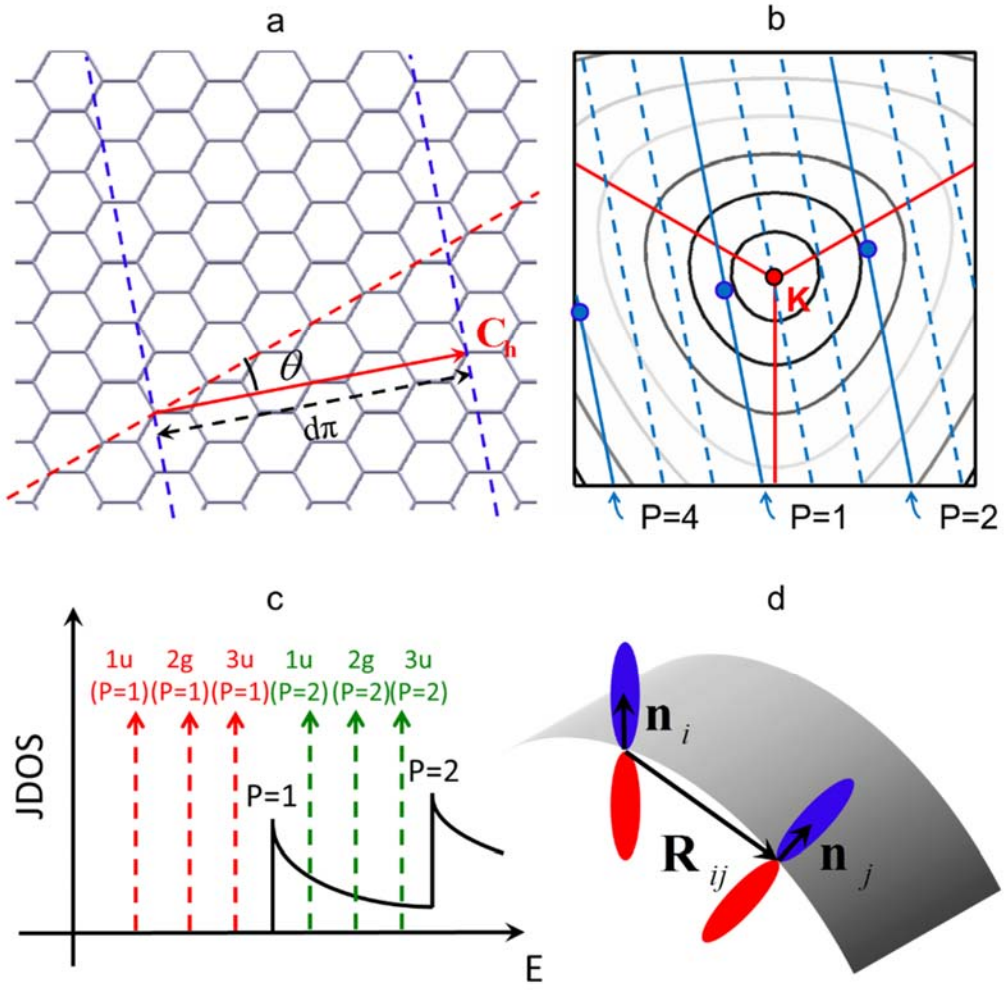

Figure II-1. Excitons in a SWCNT. (a) (4, 2) carbon nanotube geometrical structure. $\mathbf{C}_h$ is the chiral vector which is aligned along the circumferential direction when the sheet is rolled up into cylinder. $\mathbf{C}_h$, which uniquely defines a carbon nanotube, can be characterized by the chiral angle, θ, and the length $d\pi$ where d is diameter of the nanotube. (b) Graphene conduction band energy contours marked by light (gray) lines and allowed $\mathbf{k}$-lines of the carbon nanotube marked by dark (blue) lines due to quantum confinement along the circumferential direction. The subbands on the allowed $\mathbf{k}$-lines can be indexed by a number, P, which gives the distance from the Brillouin Zone corner points, K, of graphene. Filled (blue) circles indicate the location of band edge of the subbands. (c) Schematic of conduction and valence band joint density of states of SWCNT. Van Hove singularities in the joint density of states (JDOS) of each pair of subbands is labeled by P. Excitons associated with an inter-subband transition are marked by arrows and labeled by its symmetry representation such as 1u, 2g, and 3u. (d) p_z orbitals, which

are parallel to each other in planar graphene, are slant in nanotubes. $\mathbf{n}_i$ is the cylindrical surface normal unit vector and $\mathbf{R}_{ij} = (\mathbf{R}_j - \mathbf{R}_i)$ where $\mathbf{R}_i$ is the carbon position vector.

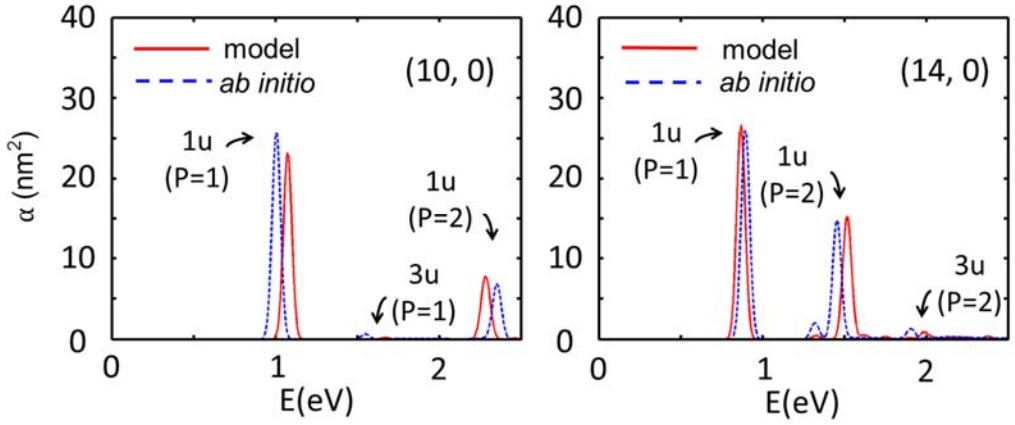

Figure II-2**.** Absorption spectra in SWCNTs from *ab initio* and model calculations. (a) The imaginary part of polarizability per tube (with light polarization along the tube axis) of the (10, 0) and (14, 0) nanotubes from *ab initio* (blue dashed line) and extended Hubbard model (red full line) calculations. Spectra are broadened with a 0.025eV Gaussian broadening. Exciton is labeled by their inter-subband P index and symmetry representation.

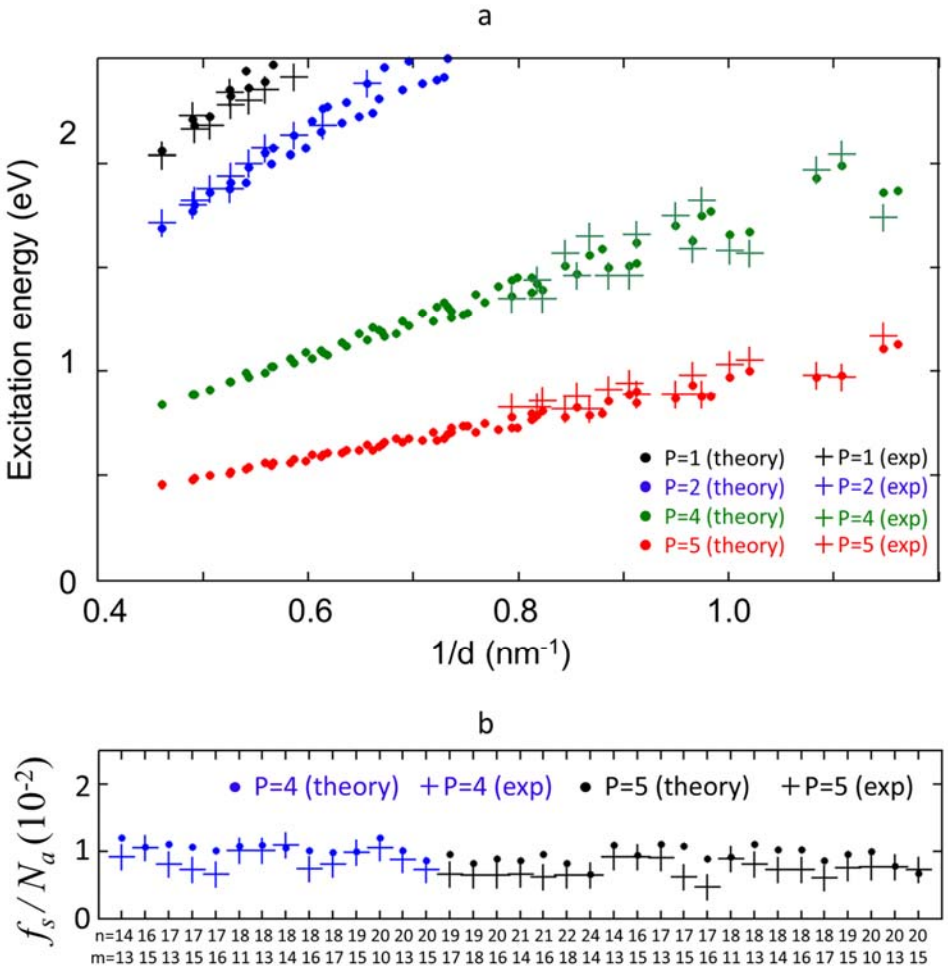

Figure II-3**.** Excitation energies and oscillator strengths of excitons in SWCNTs from theory and experiments (a) Exciton excitation energy family behavior. Dot and cross symbol are data from theory and experiments, respectively (see text). Red, green, blue, and black color represent data from the inter-subband transition of P=1, 2, 4, and 5. (b) 1u singlet exciton oscillator strength from present theory and from experiments.

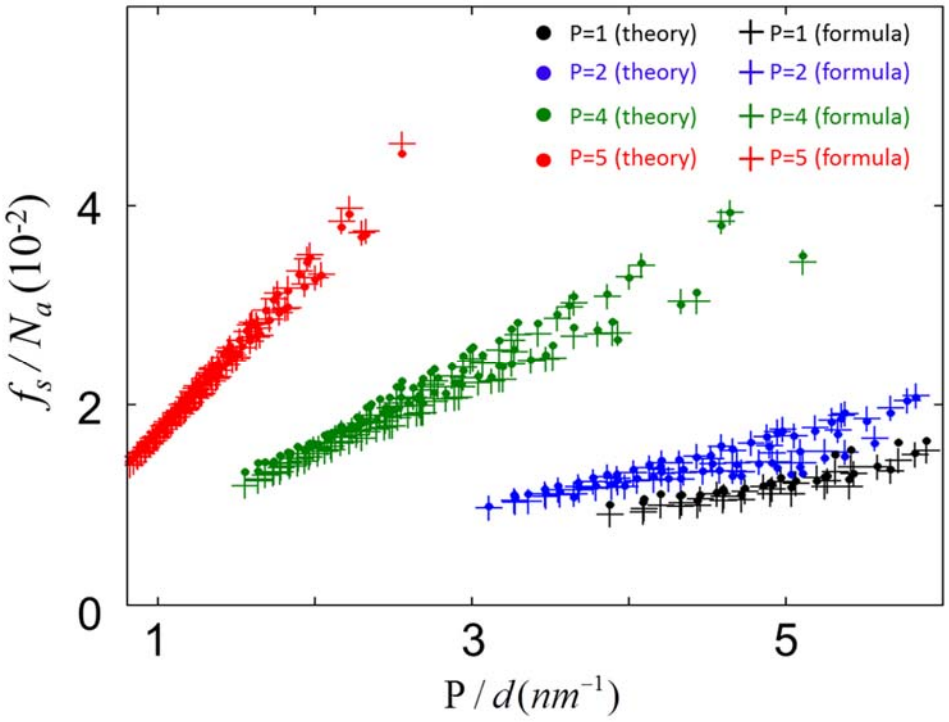

Figure II-4. The family behavior of the oscillator strengths of exciton transitions in SWCNTs. 1u singlet exciton oscillator strength family behavior. Dot and cross symbols are data from theory and the formula of $\frac{f_S}{N_a} = \frac{G(1 + J\xi cos(3\theta)\mathrm{P}/d)}{(\mathrm{P}+Q)d}$ with G=0.29 nm, J=0.047nm and Q=7.5 and $\xi = (-1)^{mod(n-m,3)+2\mathrm{P}/3+\mathrm{mod}(\mathrm{P},3)/3}$. Red, green, blue, and black color correspond to 1u singlet exciton corresponding to inter-subband transitions of P=1, 2, 4, and 5, respectively.

2. Electron beam supercollimation in graphene using one-dimensional disorder potentials

(a) Introduction

Graphene, an atomic layer of sp^2-bonded carbon atoms, is currently one of the most intensively investigated systems in condensed matter physics and materials science [42–45]. Its conical electronic structure near the Dirac points gives rise to massless neutrino-like two-dimensional (2D) electron states [46,47]. Due to the chiral nature of these Dirac fermion states, electrons in graphene interact with external potential in unusual ways, manifesting various interesting characteristics such as absence of backscattering by long-range potentials [48,49], Klein tunneling [50], weak-antilocalization [51–54], electron delocalization by one dimensional (1D) disorder [55–57], and supercollimation of electron beams by some specific 1D external periodic potentials [58]. Here we present another surprising, counter-intuitive electron transport phenomenon in graphene, made possible by the carriers' unique linear dispersion relation and chiral nature. We discovered that electron supercollimation can be induced by 1D disorder potentials. An electron wavepacket is guided to propagate virtually undistorted along the fluctuating direction of the external 1D disorder potential, independent of its initial motion, as long as the disorder is large enough to produce a wedge-like dispersion in the bandstructure within which the $\boldsymbol{k}$ -components of the wavepacket is contained. This phenomenon was not known in any medium previously. Further, we find for graphene in an external periodic potential that nearly satisfies the supercollimation condition predicted in Ref. [58], addition of disorder would greatly enhance collimation. The more is the disorder, the better is the supercollimation. This robust novel phenomenon has significant implications in the fundamental understanding of transport in graphene, as well as in other materials with Dirac cone physics (such as surface states of topological insulators [59] or possibly certain photonics crystals [60]), and has the potential to be exploited in the design of devices based on these materials.

(b) Theory and Results

We first discuss the predicted supercollimation in graphene using results from direct simulations (Figure II-5) and then derived the phenomenon from perturbation theory. For the low energy carriers in graphene (Figure II-6A) and an external potential $V(x)$ that depends only on x, we may set up an effective Hamiltonian for the electronic states [47]

$$H = \mathrm{v}_0\sigma_x p_x + \mathrm{v}_0\sigma_y p_y + V(x)I\,. \qquad \text{(II-29)}$$

Here v_0 is the Fermi velocity of electron in pristine graphene, σ_i is the i-component Pauli matrix, p_i is the i-direction momentum operator, and I is the identity matrix in the space describing the A, B sublattice components of the electron wavefunction. We may neglect

intervalley scattering for $V(x)$ that is smooth on the inter-atomic scales. We carried out direct numerical simulations on the Hamiltonian in Eq. (II-29) using a spatially-correlated Gaussian disorder potential for $V(x)$. Such a disorder potential is characterized by a two-point correlation function having $\overline{V(x_1)V(x_2)} = \Delta^2 \, \mathrm{e}^{-|x_1 - x_2|/l_c}$ where Δ is the magnitude of the disorder fluctuation and l_c is the disorder correlation length. The overline represents ensemble-averaged value. We generated the spatially correlated Gaussian disorder in the simulation by using a Cholesky decomposition of the two-point correlation matrix [61]. First, we generated a vector, $V_i = V(x_i)$, consisting of spatially-uncorrelated Gaussian-random variables having zero mean and a variance of 1. V_i can be characterized by $\overline{\underset{\sim}{V}\underset{\sim}{V}^T} = \underset{\sim}{I}$, where the tilde represents a matrix or vector and $\underset{\sim}{I}$ represents an identity matrix. A random vector $\underset{\sim}{W}$ with a desired spatial correlation, $\overline{\underset{\sim}{W}\underset{\sim}{W}^T} = \underset{\sim}{C}$ where $C_{ij} = \Delta^2 \, \mathrm{e}^{-|x_i - x_j|/l_c}$, can be obtained using by a Cholesky decomposition of $\underset{\sim}{C} = \underset{\sim}{L}\underset{\sim}{L}^T$ that is symmetric and positive definite by definition. If we construct a random vector $\underset{\sim}{W} = \underset{\sim}{L}\underset{\sim}{V}$ using the above generated $\underset{\sim}{V}$ and $\underset{\sim}{L}$ then

$$\overline{\underset{\sim}{W}\underset{\sim}{W}^T} = \underset{\sim}{L}\,\overline{\underset{\sim}{V}\underset{\sim}{V}^T}\,\underset{\sim}{L}^T = \underset{\sim}{L}\,\overline{\underset{\sim}{V}\underset{\sim}{V}^T}\,\underset{\sim}{L}^T = \underset{\sim}{L}\underset{\sim}{L}^T = \underset{\sim}{C} \qquad \text{(II-30)}$$

Hence, the random vector $\underset{\sim}{W} = \underset{\sim}{L}\underset{\sim}{V}$ would have the desired two point correlation matrix of $\underset{\sim}{C}$. Figure II-5A shows one realization of $V(x)$ in unit of Δ. The potential is spatially correlated so that on average it is nearly the same value within a length scale of l_c.

Figure II-5 B-D demonstrate supercollimation in a Gaussian wavepacket propagation simulation. Using 60 different realizations of the disorder potential $V(x)$ with $l_c\Delta = 4\pi\hbar \mathrm{v}_0$, we numerically calculated the electron density $\overline{\rho(\boldsymbol{r},t)}$ using an initial Gaussian packet with initial center of mass wavevector $k_0 = \pi / 5l_c$ and a half width of $\sqrt{2}r_0$ with $r_0 = 5l_c$. Figure II-5C and Figure II-5D show the evolution of the electron density $\overline{\rho(\boldsymbol{r},t)}$ from the initial electron density shown in Figure II-5B. In the absence of a disorder potential, the Gaussian wavepacket propagates along the initial center of mass wavevector direction marked by the white arrow and spreads sideway. Its spread angle at which the electron density is half the maximum is $48.6°$. With the 1D disorder potential $V(x)$, the electron package propagates nearly un-spread along the potential fluctuation direction, which is x, regardless of the initial velocity direction. The spread angles are $0.5°$ and $0.7°$ at an incident angle (measured from the x-axis) of $0°$ and $45°$, respectively. A very tiny fraction of the electron density forms a supercollimated trail (barely visible in Figure II-5D), which increases with increasing incident angle.

We present now an analytic derivation of the phenomenon. We separate the Hamiltonian in Eq. (II-29) into two terms, $H = H_0 + H_1$, with $H_0 = \mathrm{v}_0\sigma_x p_x + V(x)I$ and $H_1 = \mathrm{v}_0\sigma_y p_y$. If H_0 dominates over H_1 (to be defined more precisely below) as in the case of an extended low-energy wavepacket in real space in a disorder $V(x)$, we may regard $H_1 = \mathrm{v}_0\sigma_y p_y$ as a perturbation.

We first show that the electron dynamics in 2D governed by $H_0 = \mathrm{v}_0\sigma_x p_x + V(x)I$ alone yields supercollimation along the x direction. The term $\mathrm{v}_0\sigma_x p_x$ has two eigenstates ($s = \pm 1$) as shown in Figure II-6B. By a unitary transformation of $U = \frac{1}{\sqrt{2}}\begin{pmatrix} 1 & 1 \\ 1 & -1 \end{pmatrix}$, $U^\dagger \mathrm{v}_0 p_x \sigma_x U$ is diagonal with eigenvalues $s\hbar\mathrm{v}_0 k_x$ with $s = \pm 1$, and eigenvectors $\frac{1}{\sqrt{A}}\begin{pmatrix} e^{i\mathbf{k}\cdot\mathbf{r}} \\ 0 \end{pmatrix}'$ and $\frac{1}{\sqrt{A}}\begin{pmatrix} 0 \\ e^{i\mathbf{k}\cdot\mathbf{r}} \end{pmatrix}'$, respectively, where A is the area of the sample and the prime notation here indicates a matrix or vector in the unitary-transformed or pseudo-spin basis. These are chiral states moving forward ($s = 1$) or backward ($s = -1$) with a speed of v_0 and a pseudo spin aligned along the propagation direction.

We derived the exact retarded Green's function $G_0'(\mathbf{r},\mathbf{r}',t)$ of H_0' using a perturbation expansion. First, the retarded Green's function of the first or kinetic term in H_0' is

$$G_{0T}'(\mathbf{r},\mathbf{r}',t) = \frac{1}{i\hbar}\delta(y-y')\theta(t)\begin{pmatrix} \delta(x-x'-\mathrm{v}_0 t) & 0 \\ 0 & \delta(x'-x-\mathrm{v}_0 t) \end{pmatrix}. \qquad \text{(II-31)}$$

The retarded Green′s function of H_0' to infinite order in $V(x)$ is,

$$\begin{aligned}
&G_0'(\mathbf{r},\mathbf{r}',t) \\
&= G_{0T}'(\mathbf{r},\mathbf{r}',t) \\
&+ \sum_{n=1}^{\infty}\int dr_1\cdots dr_n dt_1\cdots dt_n G_{0T}'(\mathbf{r},\mathbf{r}_1,t-t_1)\, V(\mathbf{r}_1)\,\mathrm{I}\, G_{0T}'(\mathbf{r}_1,\mathbf{r}_2,t_1-t_2)\cdots V(\mathbf{r}_n)\,\mathrm{I}\, G_{0T}'(\mathbf{r}_n,\mathbf{r}',t_n) \\
&= G_{0T}'(\mathbf{r},\mathbf{r}',t) + \sum_{n=1}^{\infty}\frac{1}{(i\hbar)^{n+1}}\int_0^t dt_1\int_0^{t_1} dt_2\cdots\int_0^{t_{n-1}} dt_n\,\delta(y-y')\theta(t) \\
&\times\begin{pmatrix} V(x-\mathrm{v}_0(t-t_1))\cdots V(x-\mathrm{v}_0(t-t_n)) & 0 \\ \times\delta(x-x'-\mathrm{v}_0 t) & \\ 0 & V(x+\mathrm{v}_0(t-t_1))\cdots V(x+\mathrm{v}_0(t-t_n)) \\ & \times\delta(x'-x-\mathrm{v}_0 t) \end{pmatrix}.
\end{aligned} \qquad \text{(II-32)}$$

Since $V(x)$ at different positions commute with each other [62],

$$
\begin{aligned}
&G_0'(\boldsymbol{r},\boldsymbol{r}',t) \\
&= G_{0T}'(\boldsymbol{r},\boldsymbol{r}',t) + \sum_{n=1}^{\infty} \frac{1}{(i\hbar)^{n+1}\, n!} \int_0^t dt_1 \int_0^t dt_2 \cdots \int_0^t dt_n \delta(y-y')\theta(t) \\
&\times \begin{pmatrix} V(x-\mathrm{v}_0(t-t_1))\cdots V(x-\mathrm{v}_0(t-t_n)) & 0 \\ \times\delta(x-x'-\mathrm{v}_0 t) & \\ 0 & V(x+\mathrm{v}_0(t-t_1))\cdots V(x+\mathrm{v}_0(t-t_n)) \\ & \times\delta(x'-x-\mathrm{v}_0 t) \end{pmatrix} \qquad \text{(II-33)} \\
&= G_0'(\boldsymbol{r},\boldsymbol{r}',t) = \frac{1}{i\hbar}\theta(t)\delta(y-y') \begin{pmatrix} \delta(x-x'-\mathrm{v}_0 t)\alpha(x,x') & 0 \\ 0 & \delta(x'-x-\mathrm{v}_0 t)\alpha(x',x) \end{pmatrix},
\end{aligned}
$$

with

$$
\alpha(x,x') = \exp\left(\frac{1}{i\hbar \mathrm{v}_0} \int_{x'}^{x} V(x_1)dx_1 \right) \qquad \text{(II-34)}
$$

which satisfies $i\hbar\partial_t G_0'(\boldsymbol{r}_1,\boldsymbol{r}',t) - H_0'(\boldsymbol{r})G_0'(\boldsymbol{r},\boldsymbol{r}',t) = \delta(\boldsymbol{r}-\boldsymbol{r}')\delta(t)\mathrm{I}$. Eq. (II-33) is consistent with the transfer matrix in Ref. [63]. The Green's function determines the time evolution of the electron wavefunction and density through

$$
\psi'(\boldsymbol{r},t) = \int d\boldsymbol{r}'\, i\hbar G'(\boldsymbol{r},\boldsymbol{r}',t)\psi_0'(\boldsymbol{r}',t=0), \qquad \text{(II-35)}
$$

and

$$
\rho(\boldsymbol{r},t) = tr[\psi'(\boldsymbol{r},t)\psi'^{\dagger}(\boldsymbol{r},t)], \quad \text{(II-36)}
$$

where the trace is defined with respect to the 2×2 pseudo-spin subspace. (We recall that $\psi'(\boldsymbol{r},t)$ is a 2-component spinor function and the total density $\rho(\boldsymbol{r},t)$ is a sum over densities from the two components.) As seen from the diagonal-matrix form of $G_0'(\boldsymbol{r},\boldsymbol{r}',t)$ in Eq. (II-33) scattering between two states with different chirality (or group velocity) is not allowed for any arbitrary external potential $V(x)$, if we neglect H_1. Consequently, for the Hamiltonian H_0', the amplitude of any initial wavefunction $\psi'(\boldsymbol{r},t=0)$ with pseudo-spin s moves at a velocity of $s\mathrm{v}_0$, maintaining its initial shape, although the phase of the wave function is changed by the interaction with the potential $V(x)I$. The electron density of a wavepacket with a pseudo-spin s thus also propagates with a velocity of $s\mathrm{v}_0$ along the x direction, maintaining its original shape at $t=0$, again, if H_1' is neglected. To illustrate this point, if we take an initial Gaussian wave packet with initial center of mass wavevetor $\boldsymbol{k}_0$ and a half width of $\sqrt{2}r_0$,

$$\psi'(\boldsymbol{r},t=0)=\frac{1}{\sqrt{2\pi}r_0}\begin{pmatrix}1\\0\end{pmatrix}'\exp\left(-\frac{r^2}{4r_0^{\,2}}+i\boldsymbol{k}_0\cdot\boldsymbol{r}\right), \qquad \text{(II-37)}$$

then, as a function of time, the electron density is given by (from Eqs.(II-35) and (II-36))

$$\rho^{(0)}(\boldsymbol{r},t)=\frac{1}{2\pi r_0^2}\exp\left(-\frac{\left|\boldsymbol{r}-\mathrm{v}_0t\hat{\boldsymbol{x}}\right|^2}{2r_0^2}\right). \quad \text{(II-38)}$$

The disorder potential $V(x)$ generates a random phase accumulation for the electron which may be thought of as an effective elastic mean free path l_s or elastic collision time τ for electrons governed by H_0'. The quantity l_s may be extracted from $\bar{G}_0'$. In the expression for G_0' given by Eq. (II-33), the quantity $\alpha(x,x')$ incorporate all the effects of $V(x)$. For a random potential, translation symmetry is restored by ensemble average [64], so that $\overline{\alpha(x,x')}=\overline{\alpha(x-x')}$. The form of α in Eq. (II-34) dictates that $\overline{\alpha(x-x')}$ has its maximum at $x=x'$, and decreases as $|x-x'|$ increases since the phase of $\alpha(x,x')$ fluctuates from one member to another in an ensemble. If we assume that $\overline{\alpha(x,x')}$ decays with a full-width-half-maximum of l_s, then $\overline{G_0'(\boldsymbol{r}-\boldsymbol{r}',t)}$ decays with the same mean-distance l_s.The effective elastic collision time τ is obtained by considering $\bar{G}_0'$ in Fourier space. A Fourier transform of Eq. (II-33) yields

$$\overline{G_0'(\boldsymbol{k},\omega)}=\int dE'\frac{1}{\hbar\omega-E'+i\eta}\begin{pmatrix}A_0(E'-\hbar\mathrm{v}_0k_x) & 0\\ 0 & A_0(E'+\hbar\mathrm{v}_0k_x)\end{pmatrix} \qquad \text{(II-39)}$$

with

$$A_0(E)=\frac{1}{2\pi\hbar\mathrm{v}_0}\int dx\,\overline{\alpha(x)}\exp\left(i\frac{E}{\hbar\mathrm{v}_0}x\right). \qquad \text{(II-40)}$$

The function $A_0(E'-s\hbar\mathrm{v}_0k_x)$ here plays the role of the spectral function $A_0(s,\boldsymbol{k},\omega)$. Due to the decay of $\overline{\alpha(x)}$, $A_0(s,\boldsymbol{k},\omega)$ is maximum at $\omega=s\mathrm{v}_0k_x$ and has a finite width, owing to the effective finite elastic collision time, which is independent of the momentum $\boldsymbol{k}$. From the full-width-half-maximum of $A_0(s,\boldsymbol{k},\omega)$, we can deduce τ. For example, for a spatially correlated Gaussian disorder, one obtains:

$$\overline{\alpha(x)} = \exp\left[-\left(\frac{l_c\Delta}{\hbar v_0}\right)^2\left\{\exp\left(-\frac{|x|}{l_c}\right)-1+\frac{|x|}{l_c}\right\}\right]. \qquad \text{(II-41)}$$

Let us now consider the effects of $H_1 = \mathrm{v}_0 p_y \sigma_y$ and show that electron supercollimation still persists over a large distance L_0. We show this by examining the time evolution of the electron density $\rho(\boldsymbol{r},t)$ by the full Hamiltonian $H' = U^\dagger H U$ from a series expansion of the wavefunction up through third order in $H_1' = U^\dagger H_1 U = -v_0 p_y \sigma_y$. Suppose that we expand $\rho(\boldsymbol{r},t)$ and $\psi'(\boldsymbol{r},t)$ to third order in H_1':

$$\psi'(\boldsymbol{r},t) \simeq \sum_{i=0}^{3} \psi'^{(i)}(\boldsymbol{r},t) \quad \text{(II-42)}$$

and

$$\rho(\boldsymbol{r},t) \simeq \sum_{i=0}^{3} \rho^{(i)}(\boldsymbol{r},t), \quad \text{(II-43)}$$

where $\psi'^{(i)}(\boldsymbol{r},t)$ and $\rho^{(i)}$ are the ith order terms in H_1'. Substituting these expansions to Eq. (II-36) and arranging them according to powers in H_1',

$$\rho^{(0)}(\boldsymbol{r},t) = tr\left[\psi^{(0)}(\boldsymbol{r},t)\psi^{(0)\dagger}(\boldsymbol{r},t)\right], \quad \text{(II-44)}$$

$$\rho^{(1)}(\boldsymbol{r},t) = 2\,\mathrm{Re}\left(\mathrm{tr}\left[\psi^{(1)}(\boldsymbol{r},t)\psi^{(0)\dagger}(\boldsymbol{r},t)\right]\right), \quad \text{(II-45)}$$

$$\rho^{(2)}(\boldsymbol{r},t) = \rho_{02}^{(2)}(\boldsymbol{r},t) + \rho_{11}^{(2)}(\boldsymbol{r},t) \quad \text{(II-46)}$$

with

$$\rho_{02}^{(2)}(\boldsymbol{r},t) = 2\,\mathrm{Re}\left(tr\left[\psi^{(0)}(\boldsymbol{r},t)\psi^{(2)\dagger}(\boldsymbol{r},t)\right]\right) \quad \text{(II-47)}$$

and

$$\rho_{11}^{(2)}(\boldsymbol{r},t) = tr\left[\psi^{(1)}(\boldsymbol{r},t)\psi^{(1)\dagger}(\boldsymbol{r},t)\right], \quad \text{(II-48)}$$

and

$$\rho^{(3)}(\boldsymbol{r},t) = 2\,\mathrm{Re}\left(tr\left[\psi^{(3)}(\boldsymbol{r},t)\psi^{(0)\dagger}(\boldsymbol{r},t)\right] + tr\left[\psi^{(2)}(\boldsymbol{r},t)\psi^{(1)\dagger}(\boldsymbol{r},t)\right]\right). \quad \text{(II-49)}$$

As explained before, the zeroth order term $\rho^{(0)}(\boldsymbol{r},t)$ always shows supercollimation with the initial charge density. The first order term $\rho^{(1)}(\boldsymbol{r},t)$ and the third order term $\rho^{(3)}(\boldsymbol{r},t)$ is zero since the even order terms such as $\psi^{(0)}(\boldsymbol{r},t)$ and $\psi^{(2)}(\boldsymbol{r},t)$ are orthogonal to the odd order terms such as $\psi^{(1)}(\boldsymbol{r},t)$ and $\psi^{(3)}(\boldsymbol{r},t)$ in pseudo-spin space. Among the two second order terms, the $\rho_{02}^{(2)}(\boldsymbol{r},t)$ term doesn't disrupt supercollimation because the amplitude of $\psi^{(0)}(\boldsymbol{r},t)$ is $\sqrt{\rho^{(0)}(\boldsymbol{r},\mathrm{t})}$, which constrains $\rho_{02}^{(2)}(\boldsymbol{r},t)$ to have the same extent and motion as $\rho^{(0)}(\boldsymbol{r},t)$ in coordinate space. Only $\rho_{11}^{(2)}(\boldsymbol{r},t)$ may show electron dynamics deviating from electron beam supercollimation. With an initial wave packet of $\begin{pmatrix}1\\0\end{pmatrix}' \psi_0(\boldsymbol{r})\exp(i\boldsymbol{k}_0\cdot\boldsymbol{r})$ where $\boldsymbol{k}_0$ is the initial center of mass wavevector, $\rho_{11}^{(2)}(\boldsymbol{r},t)$ is

$$\begin{aligned}\rho_{11}^{(2)}(\boldsymbol{r},t) = \int_{x-v_0t}^{x+v_0t} dx_1 \int_{x-v_0t}^{x+v_0t} dx_2 [(k_{0y} - i\partial_y)\psi_0(x_1,y)][(k_{0y} - i\partial_y)\psi_0(x_2,y)]^* \\ \times \exp(ik_x(x_1 - x_2))\beta(x_1,x_2),\end{aligned} \quad \text{(II-50)}$$

with

$$\beta(x_1,x_2) = \alpha(x_1,x_2)\ \alpha((x_2 + x + \mathrm{v}_0 t)/2, (x_1 + x + \mathrm{v}_0 t)/2)^2 . \quad \text{(II-51)}$$

To obtain $\rho_{11}^{(2)}(r,t)$ on average, we estimated $\overline{\beta(x_1,x_2)}$. If $|x + \mathrm{v}_0 t| > r_0 + l_s$, the two factors in Eq. (II-51) are not correlated so that

$$\begin{aligned}\overline{\beta(x_1,x_2)} &\simeq \overline{\alpha(x_1,x_2)}\ \overline{\alpha((x_2 + x + \mathrm{v}_0 t)/2, (x_1 + x + \mathrm{v}_0 t)/2)^2} \\ &\simeq \overline{\alpha(x_1,x_2)}\ \overline{\alpha(x_2/2, x_1/2)^2}.\end{aligned} \quad \text{(II-52)}$$

If we assume that $\overline{\alpha(x,x')}$ decays with a full-width-half-maximum of l_s and l_s is inversely proportional to the disorder fluctuation as is the case of spatially-correlated Gaussian disorder, then

$$\overline{\alpha(x_1,x_2)}\,\overline{\alpha(x_2/2, x_1/2)^2} = \overline{\alpha(x_1,x_2)}^2 . \quad \text{(II-53)}$$

And

$$\begin{aligned}\overline{\rho_{11}^{(2)}(\boldsymbol{r},t)} \simeq \int_{x-v_0t}^{x+v_0t} dx_1 \int_{x-v_0t}^{x+v_0t} dx_2 [(k_{0y} - i\partial_y)\psi_0(x_1,y)][(k_{0y} - i\partial_y)\psi_0(x_2,y)]^* \\ \times \exp(ik_x(x_1 - x_2))\overline{\alpha(x_1,x_2)}^2 .\end{aligned} \quad \text{(II-54)}$$

Eq. (II-54) can be simplified for $r_0 > l_s$. In that case, $\overline{\alpha(x_1,x_2)}^2$ may be approximated by $l_s\delta(x_1-x_2)$ since $\psi_0(\boldsymbol{r})$ is a smooth function. Then

$$\overline{\rho_{11}^{(2)}(\boldsymbol{r},t)} \simeq l_s \int_{x-v_0 t}^{x+v_0 t} dx\, |(k_{0y} - i\partial_y)\psi_0(x_1,y)|^2 \ . \quad \text{(II-55)}$$

This corresponds a strip of density of width determined by the initial wavepacket but extended from $v_0 t$ to $-v_0 t$ in the x direction. For example, for an initial Gaussian wave packet given by Eq. (II-37),

$$\overline{\rho}_{11}^{(2)}(\boldsymbol{r},t) \simeq \frac{l_s}{2\sqrt{2\pi}r_0}\left(k_{0y}^2 + \frac{y^2}{4r_0^4}\right) e^{-y^2/2r_0^2}\left(-Erf\left(\frac{x-v_0 t}{\sqrt{2}r_0}\right) + Erf\left(\frac{x+v_0 t}{\sqrt{2}r_0}\right)\right). \quad \text{(II-56)}$$

Also, we shall assume that Eq. (II-56) approximates $\overline{\rho_{11}^{(2)}(\boldsymbol{r},t)}$ even if $|x+v_0 t| \le r_0 + l_s$ and $r_0 > l_s$. This is justified by the numerical wavepacket simulation with spatially-correlated Gaussian disorder potential. If we compare $\int d\boldsymbol{r}\,\overline{\rho_{11}^{(2)}(\boldsymbol{r},t)}$ with $\int d\boldsymbol{r}\,\rho^{(0)}(\boldsymbol{r},t)$, $\int d\boldsymbol{r}\,\overline{\rho_{11}^{(2)}(\boldsymbol{r},t)} < \int d\boldsymbol{r}\,\rho^{(0)}(\boldsymbol{r},t)$ for $(2k_{0y}^2 + 1/(2r_0^2))l_s v_0 t < 1$, giving rise to supercollimation with little diminishment of the intensity of the original Gaussian profile over a distance of roughly $L_0 = v_0 t = 1/\left(2l_s k_{0y}^2 + l_s/(2r_0^2)\right)$. For example, for a disorder potential that gives a broadening of 0.2 eV in the spectral function, a wavepacket with $r_0 > 40nm \simeq 250a_{cc}$ and a center of mass wavevector such that $\hbar v_0 k_{0y} < 0.01eV$ will undergo supercollimation for nearly a micrometer.

We propose a possible experiment to demonstrate the predicted electron supercollimation phenomenon by measuring the conductance G in a geometry shown in Figure II-7A. In this set up, graphene is in contact with two electrodes that are separated at a distance L along the $\hat{\mu}$ direction. This direction is at an angle θ with respect to the 1D potential fluctuation direction $\hat{x}$. The conductance G between the two electrodes is, according to the Kubo formula [65,66],

$$G(L,\theta) = \int d\boldsymbol{r}d\boldsymbol{r}'\,\sigma_{\mu\mu}(\boldsymbol{r},\boldsymbol{r}',E_F)\delta(\mu)\delta(\mu'-L), \quad \text{(II-57)}$$

with conductivity

$$\sigma_{\mu\mu}(\boldsymbol{r},\boldsymbol{r}',E_F) = \frac{\pi\hbar}{(2\pi i)^2} tr\left[j_\mu(\boldsymbol{r})(G^{R-A}(\boldsymbol{r},\boldsymbol{r}',E_F))\, j_\mu(\boldsymbol{r}')(G^{R-A}(\boldsymbol{r}',\boldsymbol{r},E_F))\right] \quad \text{(II-58)}$$

where $\boldsymbol{j} = e\mathrm{v}_0\boldsymbol{\sigma}$ [67]. The quantity G^{R-A} is defined as $\mathrm{G}^{R-A} = \mathrm{G}^{R} - \mathrm{G}^{A}$ with G^R and G^A being the retarded and advanced Green's functions, respectively. Suppose that we expand G^{R-A} and conductance G to first order in H_1'

$$G(L,\theta) \simeq G^{(0)}(L,\theta) + G^{(1)}(L,\theta) + \cdots \quad \text{(II-59)}$$
$$G^{R-A}(\boldsymbol{r},t) \simeq G^{R-A,(0)}(\boldsymbol{r},t) + G^{R-A,(1)}(\boldsymbol{r},t) + \cdots \quad \text{(II-60)}$$

where conductance $G^{(i)}$ and $G^{\mathrm{R-A},(i)}$ represent the ith order term in H_1'. Substituting these expansions to Eq. (II-57) and arranging them according to powers in H_1', we have

$$G^{(0)}(L,\theta) = \frac{\pi\hbar}{(2\pi i)^2} \int d\boldsymbol{r}d\boldsymbol{r}'\, tr\{J_\mu(\boldsymbol{r})(\mathrm{G}^{R-A,(0)}(\boldsymbol{r},\boldsymbol{r}',E_F))J_\mu(\boldsymbol{r}')(\mathrm{G}^{R-A,(0)}(\boldsymbol{r}',\boldsymbol{r},E_F))\}\delta(\mu)\delta(\mu'-L), \quad \text{(II-61)}$$

and

$$G^{(1)}(L,\theta) = \frac{\pi\hbar}{(2\pi i)^2} \int d\boldsymbol{r}d\boldsymbol{r}' \Big[tr\{J_\mu(\boldsymbol{r})(\mathrm{G}^{R-A,(0)}(\boldsymbol{r},\boldsymbol{r}',E_F))J_\mu(\boldsymbol{r}')(\mathrm{G}^{R-A,(1)}(\boldsymbol{r}',\boldsymbol{r},E_F))\} + tr\{J_\mu(\boldsymbol{r})(\mathrm{G}^{R-A,(1)}(\boldsymbol{r},\boldsymbol{r}',E_F))J_\mu(\boldsymbol{r}')(\mathrm{G}^{R-A,(0)}(\boldsymbol{r}',\boldsymbol{r},E_F))\}\Big]\delta(\mu)\delta(\mu'-L). \quad \text{(II-62)}$$

The zeroth order term in momentum space is, if we assume that $\overline{\alpha(|x_1 - x_2|)}$ decays exponentially,

$$\overline{G^{(0)}(L,\theta)} = \frac{2e^2}{h}\sum_{k_y}\left(\cos^2\theta + \sin^2\theta \exp[-2L/l_s\cos\theta]\cos(2E_F L/(\hbar \mathrm{v}_0\cos\theta))\right). \quad \text{(II-63)}$$

with periodic boundary condition along the ν direction. The first order term $G^{(1)}(L,\theta) = 0$ due to cancellation of the two terms in Eq. (II-62). This is dramatically distinct from that of a gated prinstine graphene in the ballistic regime, in which case the conductance $G(L,\theta)$ is constant regardless of the orientation angle θ.

The ensemble-average dispersion relation of the electrons is strongly and anisotropically renormalized in the presence of the random potential $V(x)$ for $|k_y| < 1/l_s$, forming a wedge-like structure for the energy surface $E(\boldsymbol{k})$. The contribution of the perturbing Hamiltonian, $H_1' = U^\dagger H_1 U = -\mathrm{v}_0 p_y \sigma_y$, to the electronic states can be evaluated by using a perturbation expansion of the retarded Greens function to first order in H_1',

$$G'(\boldsymbol{k},\boldsymbol{k}',\omega) \simeq G'_0(k_x,k'_x,\omega)\delta_{k_y k'_y} + \sum_{k''_x} G'_0(k_x,k''_x,\omega)H'_1(k_y)G'_0(k''_x,k'_x,\omega)\delta_{k_y k'_y} \qquad \text{(II-64)}$$

where $H'_1(k_y) = \langle \boldsymbol{k} | H'_1 | \boldsymbol{k} \rangle$. For a random potential $V(x)$, an ensemble average of Eq. (II-64) should be performed. The magnitude of the off-diagonal components of $\overline{G'_0(k_x)}H_1(k_y)$ in pseudo-spin indices may be viewed as a measure of the perturbation strength on average since $\bar{G}'_0$ is a diagonal matrix with respect to pseudo-spin indices as well as with respect to wavevectors (since translation symmetry of pristine graphene is restored by ensemble average [64]) and the diagonal components of $H'_1(k_y)$ in the pseudo-spin indices are zero. The maximum value of $|\bar{G}'_0(k_x,\omega)|$ is $\sim \tau/\hbar I'$ if we assume that the spectral function of an electronic state with k_x and s follows a Lorentzian distribution centered at $\omega = s\mathrm{v}_0 k_x$ with a full width at half maximum of $\sim 2\hbar/\tau$. Since $H'_1(k_y) = -\hbar \mathrm{v}_0 k_y \sigma_y$, the first and higher order contribution from H'_1 can be neglected if $|\tau \mathrm{v}_0 k_y| = |k_y l_s| < 1$, resulting in a flat dispersion given by H'_0.

We demonstrate this effect by calculating the ensemble-average spectral function. Using 60 different realizations of the disorder with $l_c\Delta = 4\pi\hbar\mathrm{v}_0$, we numerically calculated $\mathrm{Im}\, G'(\boldsymbol{k},\omega)$. Figure II-8 shows the 60-ensemble-average spectral function, $A(\boldsymbol{k},E) = -tr\, \mathrm{Im}\overline{G'(\boldsymbol{k},E)}/\pi$ where the trace is with respect to the 2×2 pseudo-spin subspace. Along the $\boldsymbol{k} = (k_x, 0)$ line, shown in Figure II-8A, the dispersion relation is linear and it follows the $E = \pm\hbar\mathrm{v}_0 k_x$ lines, which is the dispersion relation of pristine graphene. However, along the $\boldsymbol{k} = (0, k_y)$ line, shown in Figure II-8B, the bandstructure is strongly renormalized near the Dirac point and becomes flat. The anisotropic renormalization of the band structure can be demonstrated more clearly by a contour plot of $A(\boldsymbol{k},E)$ on the k_x-k_y plane with $E = 2\hbar v_0/l_s$, as shown in Figure II-8C. On this constant energy plane, constant amplitude lines of $A(\boldsymbol{k},E)$ are oval-shaped and stretched along the k_y direction. For spatially-correlated Gaussian disorder potentials, we can evaluate explicitly the spectral function of $\bar{G}'_0$ from the Fourier transform of Eq. (II-41). For this particular kind of disorder, the lineshape of the spectral function at different k_x with $|k_{0y}| < 1/l_s$ is identical and $\tau \sim \hbar/\Delta$. As shown in Figure II-8 D, the line shape from Eqs. (II-40) and (II-41) matches well with numerically simulated line shape from $\bar{G}'$ at various k_x with $k_y = 0$. However, as k_y increases (at $k_x = 0$), the numerically calculated spectral function deviates from the lineshape from $\overline{\alpha(x)}$ owing to the effect of H'_1.

Electron beam supercollimation has been predicted theoretically in certain special graphene superlattices (SGS): a graphene sheet modulated by 1D periodic potential satisfying specific conditions [58]. In the experimental realization of SGS (e.g., using substrate [68], controlled adatom deposition [69], ripples [70] under perpendicular electric field [71,72], or gating [73]), it is unavoidable to have some disorders in the external potential, which previously

thought might impede the supercollimation effect. However, we found that 1D disorder along the periodic potential modulation direction in fact enhances supercollimation for an external periodic potential which nearly satisfies the supercollimation condition. We demonstrate this effect by evaluating $\overline{\rho_{11}^{(2)}(\boldsymbol{r},t)}$ since the other terms to $\rho(\boldsymbol{r},t)$ up through third order always show supercollimation as discussed above. For a system under disorder potential in addition to the periodic potential, if $|x+\mathrm{v}_0 t|>r_0+l_s$,

$$\begin{aligned}\overline{\rho_{11}^{(2)}(\boldsymbol{r},t)} \simeq & \int_{x-v_0t}^{x+v_0t} dx_1 \int_{x-v_0t}^{x+v_0t} dx_2 [(k_{0y}-i\partial_y)\psi_0(x_1,y)][(k_{0y}-i\partial_y)\psi_0(x_2,y)]^* \\ & \times \exp(ik_x(x_1-x_2))\overline{\alpha_D(x_1,x_2)}\overline{\alpha_D(x_2/2,x_1/2)^2}\beta_P(x_1,x_2).\end{aligned} \quad \text{(II-65)}$$

Here $\beta_P(x_1,x_2)$ is $\beta(x_1,x_2)$ of the periodic potential and $\alpha_D(x_1,x_2)$ is $\alpha(x_1,x_2)$ of the disorder potential. If we assume that $\overline{\alpha(x,x')}$ decays with a full-width-half-maximum of l_s and l_s is inversely proportional to the disorder fluctuation as is in the case of spatially-correlated Gaussian disorder, then

$$\overline{\alpha_D(x_1,x_2)}\overline{\alpha_D(x_2/2,x_1/2)^2} = \overline{\alpha_D(x_1,x_2)}^2. \quad \text{(II-66)}$$

And we have

$$\begin{aligned}\overline{\rho_{11}^{(2)}(\boldsymbol{r},t)} \simeq & \int_{x-v_0t}^{x+v_0t} dx_1 \int_{x-v_0t}^{x+v_0t} dx_2 [(k_{0y}-i\partial_y)\psi_0(x_1,y)][(k_{0y}-i\partial_y)\psi_0(x_2,y)]^* \\ & \times \exp(ik_x(x_1-x_2))\overline{\alpha_D(x_1,x_2)}^2\beta_P(x_1,x_2).\end{aligned} \quad \text{(II-67)}$$

For $r_0 > l_s$, $\overline{\alpha_D(x_1,x_2)}^2$ may be approximated by $l_s\delta(x_1-x_2)$ since $\psi_0(\boldsymbol{r})$ is a smooth function. Then,

$$\overline{\rho_{11}^{(2)}(\boldsymbol{r},t)} \simeq l_s \int_{x-v_0t}^{x+v_0t} dx\, |(k_{0y}-i\partial_y)\psi_0(x_1,y)|^2. \quad \text{(II-68)}$$

Here, we assume that Eq. (II-68) approximate $\overline{\rho_{11}^{(2)}(\boldsymbol{r},t)}$ even if $|x+\mathrm{v}_0 t| \le r_0+l_s$ and $r_0 > l_s$. This is justified by the numerical wavepacket simulation with center-width-height disorder potential. Eq. (II-68) is the same form as Eq. (II-55), indicating that $\overline{\rho_{11}^{(2)}(r,t)}$ decreases as l_s/r_0 decreases as shown in Eq. (II-56).

We demonstrate this effect numerically using a width-height-center disorder to a particular type of periodic potential with a height of U_0 and a period of l shown in Figure II-9A. For each potential unit, we can disorder its center, width, and potential height by using mutually independent Gaussian random variables with a standard deviation of Δ_D centered at the

original value. We calculated wavepacket propagation in graphene under this disordered periodic potential from 60 ensemble average with $U_0 = 2\pi\hbar v_0 / l$ (which is half of the potential magnitude needed for supercollimation in SGS) and an Δ_D that is a 100 % of the original variables (potential height, center and width). The initial wave packet is given by Eq. (II-37) with $r_0 = 5l$ and $k_0 = \pi / 5l$. Figure II-9C and Figure II-9D show the electron density distributions at two different incident angles θ of 0° and 45° from the x axis. Without disorder, the electrons propagate nearly along the incident center of mass wavevector direction. Although the electron beam is slightly collimated along the x direction (owing to the superlattice potential) compared to pristine graphene shown in Figure II-5, it still spreads along the y direction. If we add the above disorder to this periodic potential, the Gaussian wave packet maintains its Gaussian shape and propagates along the direction of the external potential modulation regardless of the incident angle.

Here, we discuss an additional condition for observing supercollimation using an external disorder potential: the upper bound for disorder correlation length l_c. Firstly, l_c should be shorter than the phase coherence length L_ϕ of the system. Phase coherence length is the length scale beyond which there is no interference effect or no phase coherence [66]. It is originated from the incoherent and irreversible processes due to coupling of an electron to the environment such as interaction with phonons, other electrons, and impurities with internal degrees of freedom. For the case of prinstine graphene, it is $\sim 0.5\mu m$ [74]. We may expect that for a sample with $l_c >> L_\phi$, an electron would see a more or less constant potential before losing its phase-coherence. In this case, the broadening in the spectral function is originated from the distribution of the constant potential heights, not from the random phase accumulation in each member of the ensemble. In contrast, if $l_c < L_\phi$, the electron sees the potential variation before losing phase coherence and the external potential plays a role of a disorder potential. Then, broadening in the spectral function is originated from the random phase accumulation of the electron. Secondly, there is another consideration on the upper limit in l_c set by the reflection of a charge carrier from a slowly-varying potential. It is known that if an electronic state in graphene with wavevector $\boldsymbol{k}_0$ encounters a slowly-varying *p-n* junction such that the external potential changes by $\hbar v_0 k_0$ over a distance d_c, the propagating state will be partially reflected from the junction if $k_0 d_c > 1$ [63]. We have considered a potential with characteristic variation in strength by Δ over a distance of $\sim l_c$; hence, in our case, the distance d_c for partial reflection corresponds roughly to $d_c \sim l_c \dfrac{\hbar v_0 k_0}{\Delta}$ and the condition that such reflection does not occur is $k_0 \left(l_c \dfrac{\hbar v_0 k_0}{\Delta} \right) < 1$. Or, if we define $L_{PN} = \Delta / (\hbar v_0 k_0^2)$, the second condition on l_c reduces to $l_c < L_{PN}$. Combining these two effects, the upper bound on l_c for observing supercollimation discussed in our paper is roughly given by the shorter of the two lengths, L_ϕ and L_{PN}.

(c) Conclusion

In summary, through perturbation theory analysis and numerical simulations, we have discovered a highly counter-intuitive phenomenon of electron supercollimation via 1D disorder potential in graphene. To our knowledge, this phenomenon is not seen in any other systems.

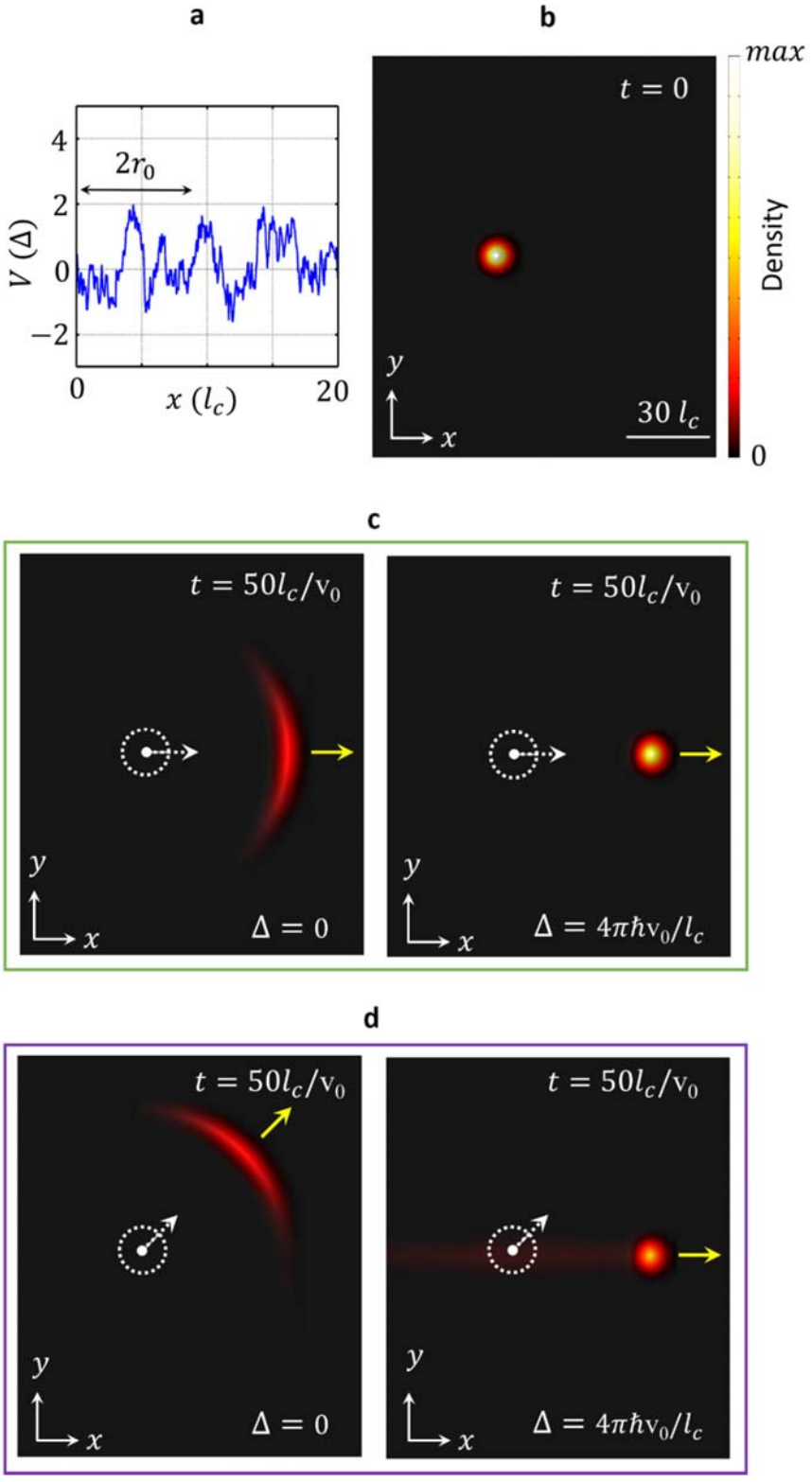
a
b
$2r_0$
$V\ (\Delta)$
$x\ (l_c)$
$t = 0$
$30\ l_c$
max
Density
0
c
$t = 50l_c/v_0$
$\Delta = 0$
$\Delta = 4\pi\hbar v_0/l_c$
d

Figure II-5 **(A)** A realization of spatially-correlated Gaussian disorder potential $V(x)$ with a magnitude Δ and correlation length l_c. **(B)** Initial wavepacket with electron density in a Gaussian shape in coordinate space with initial center of mass wavevector $k_0 = \pi / 5l_c$ and a half-width $r_0 = 5l_c$. **(C)-(D)** Electron density distribution in coordinate space at time $t = 50l_c / \mathrm{v}_0$ in prinstine graphene (left panel) and in disordered graphene (right panel) with initial center of mass wavevector direction (white arrow) pointing with respect to the x axis at $0°$ **(C)** and $45°$ **(D)**.

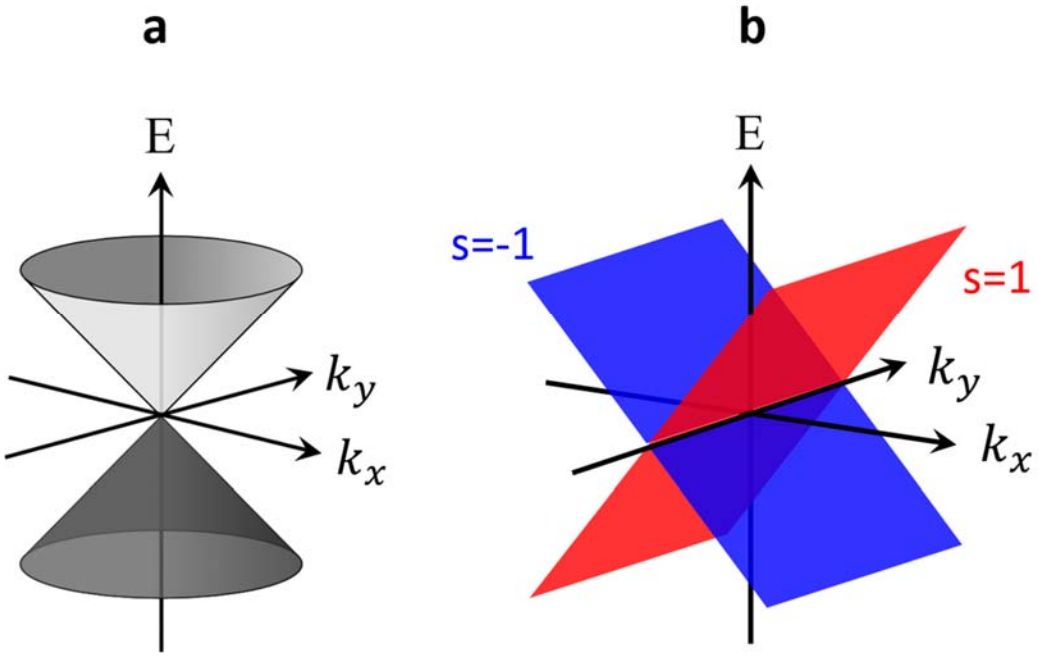

Figure II-6**.** (**A)** Low-energy electronic bandstructure of graphene near a Dirac point. **(B)** Electronic bandstructure of an initial 2D model Hamiltonian, $H_{in} = \mathrm{v}_0 \sigma_x p_x$, where v_0 is the Fermi velocity, σ_x is the x-component Pauli matrix and p_x is the x-direction momentum operator. This model Hamiltonian generates two chiral eigenstates which correspond to forward-moving ($s = 1$) and backward-moving ($s = -1$) states with a speed of v_0 and a pseudo-spin parallel to $s\hat{x}$.

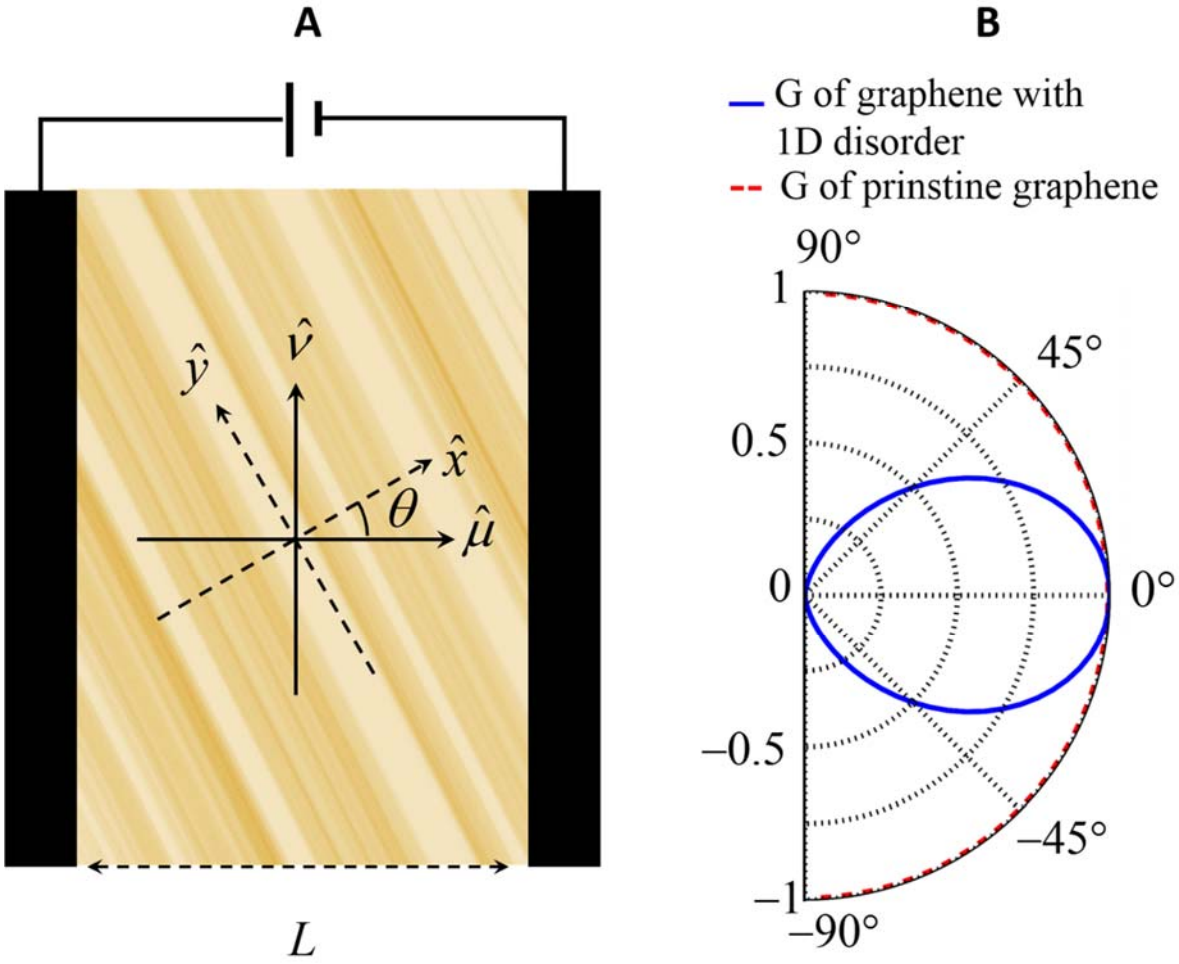

Figure II-7 **(A)** Schematic diagram of experimental setup for proposed conductance measurement. Two electrodes are in contact with graphene under 1D disorder potential fluctuating along the $\hat{x}$ direction. The electrodes are separated by a distance L along the $\hat{\mu}$ direction. **(B)** Calculated conductance $G(L,\theta)$ (in a unit of $2N_\nu e^2/h$ where N_ν is the number of subbands due to the confinement along the ν direction at energy E_F) as a function of the angle θ in a gated prinstine graphene in the ballistic regime (red line) and in graphene with 1D disorder potential ($l_s \ll L$) shown in **(A)** (blue line).

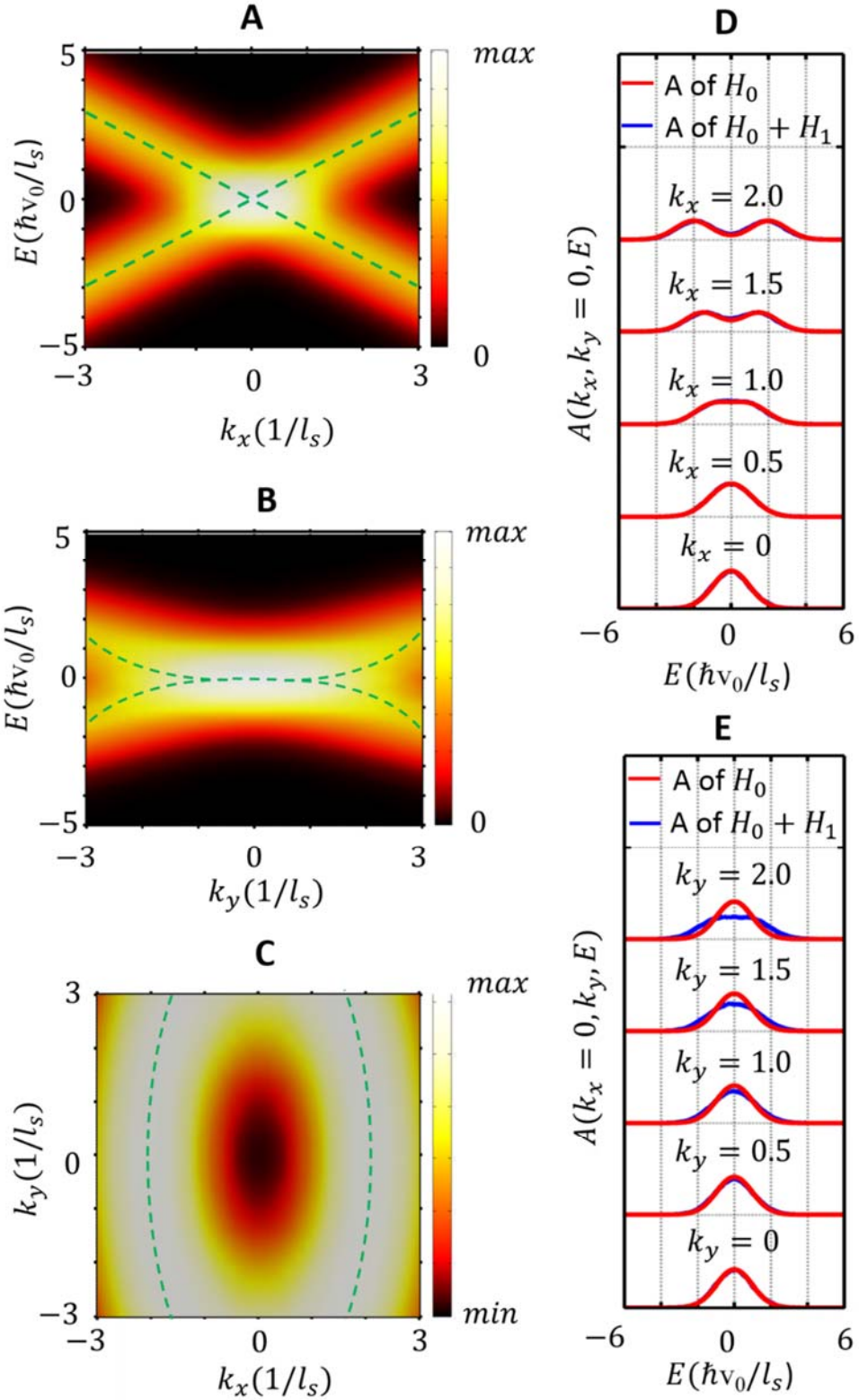
A
B
C
D
E
max
min
0
A of H_0
A of $H_0 + H_1$
$k_x = 2.0$
$k_x = 1.5$
$k_x = 1.0$
$k_x = 0.5$
$k_x = 0$
$k_y = 2.0$
$k_y = 1.5$
$k_y = 1.0$
$k_y = 0.5$
$k_y = 0$
$E(\hbar v_0/l_s)$
$k_x(1/l_s)$
$k_y(1/l_s)$
$A(k_x, k_y = 0, E)$
$A(k_x = 0, k_y, E)$

Figure II-8 **(A)-(C)** Numerically evaluated spectral function, $A(\boldsymbol{k},E) = -\,tr\,\mathrm{Im}\,\overline{G'(\boldsymbol{k},E)}/\pi$, for $l_c\Delta = 4\pi\hbar \mathrm{v}_0$ along the $k_y = 0$ line **(A)**, along the $k_x = 0$ line **(B)**, and on the $E = 2\hbar \mathrm{v}_0 / l_s$ plane with $l_s = \dfrac{\hbar \mathrm{v}_0}{\Delta}$ **(C)**. **(D)-(E)** The lineshapes of the spectral function of $H_0 = \mathrm{v}_0 \sigma_x p_x + V(x) I$ (red lines) and of $H_0 + H_1$ (blue lines) with $H_1 = \mathrm{v}_0 \sigma_y p_y$ at various k_x with $k_y = 0$ **(D)**, and at various k_y with $k_x = 0$ **(E)** .

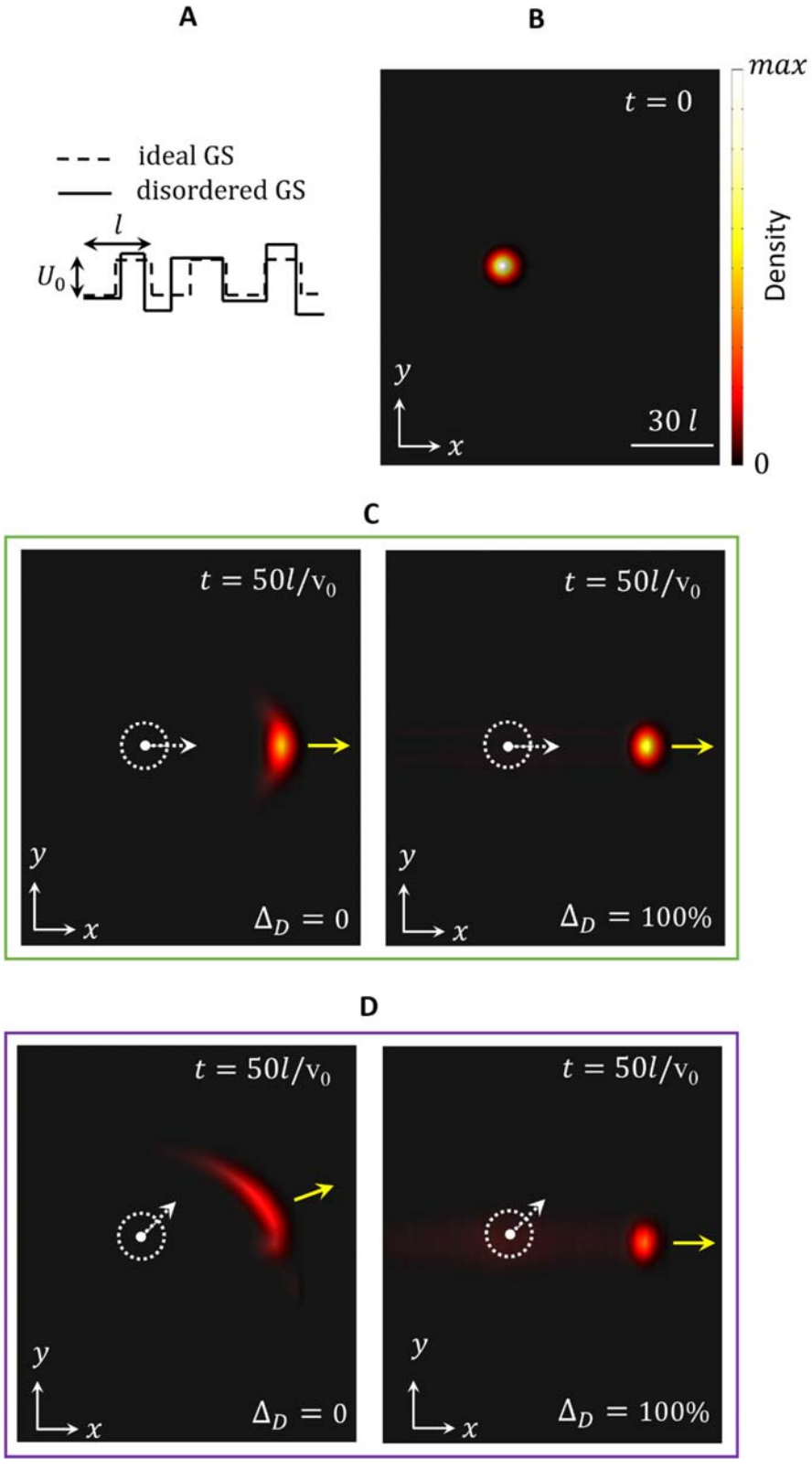
A
B
ideal GS
disordered GS
l
U_0
$t = 0$
max
Density
0
y
x
30 l
C
$t = 50l/v_0$
$\Delta_D = 0$
$t = 50l/v_0$
$\Delta_D = 100\%$
D
$t = 50l/v_0$
$\Delta_D = 0$
$t = 50l/v_0$
$\Delta_D = 100\%$

Figure II-9 **(A)** A realization of a periodic potential with 1D disorder. The full and dashed lines represent disordered and ideal periodic external potential, respectfully. **(B)** Initial wavepacket with electron density in a Gaussian shape in coordinate space with initial center of mass wavevector of $k_0 = \pi / 5l$ and $r_0 = 5l$. **(C)-(D)** Electron density distribution in coordinate space at $t = 50l / \mathrm{v}_0$ in graphene under periodic potential with $U_0 l = 2\pi\hbar \mathrm{v}_0$ (left panel) and in graphene under the same periodic potential but with disordered height, center and width of $\Delta_D = 100\%$ (right panel) with initial center of mass wavevector direction (white arrow) pointing with respect to the $\hat{x}$ axis at $0°$ **(C)** and $45°$ **(D)**.

III. Interfaces

1. Localization of metal-induced gap states at the metal-insulator interface.

(a) Introduction

Well below 1 K, low-transition temperature Superconducting Quantum Interference Devices [75] (SQUIDs) exhibit magnetic flux noise [76] with a temperature-independent spectral density scaling as $1/f^{\alpha}$, where f is frequency and $0.6 \leq \alpha \leq 1$. The noise magnitude, a few $\mu\Phi_0 \mathrm{Hz}^{1/2}$ at 1 Hz (Φ_0 is the flux quantum), scales slowly with the SQUID area, and does not depend significantly on the nature of the thin film superconductor or the substrate on which it is deposited. The substrate is typically silicon or sapphire, which are insulators at low temperature (T) [76]. Flux noise of similar magnitude is observed in flux [77,78] and phase [79] qubits. Flux noise limits the decoherence time of superconducting, flux sensitive qubits making scale-up for quantum computing problematic. The near-insensitivity of noise magnitude to device area [76,79,80] suggests the origin of the noise is local. Koch *et al.* [81] proposed a model in which electrons hop stochastically between traps with different preferential spin orientations. A broad distribution of time constants is necessary to produce a $1/f$ power spectrum [82,83]. They found that the major noise contribution arises from electrons above and below the superconducting loop of the SQUID or qubit [79,81], and that an areal density of about $5\times10^{17}\mathrm{m}^{-2}$ unpaired spins is required to account for the observed noise magnitude. De Sousa [84] proposed that the noise arises from spin flips of paramagnetic dangling bonds at the Si-SiO_2 interface. Assuming an array of localized electrons, Faoro and Ioffe [85] suggested that the noise results from electron spin diffusion. Sendelbach *et al.* [86] showed that thin film SQUIDs are paramagnetic, with a Curie ($1/T$) susceptibility. Assuming the paramagnetic moments arise from localized electrons, they deduced an areal density of $5 \times 10^{17}\mathrm{m}^{-2}$. Subsequently, Bluhm *et al.* [87] used a scanning SQUID microscope to measure the low-T paramagnetic response of (nonsuperconducting) Au rings deposited on Si substrates, and reported an areal density of $4 \times 10^{17}\mathrm{m}^{-2}$ for localized electrons. Paramagnetism was not observed on the bare Si substrate.

In this section, we propose that the local magnetic moments originate in metal-induced gap states (MIGS) [88] localized by potential disorder at the metal-insulator interface. At an ideal interface, MIGS are states in the band gap that are evanescent in the insulator and extended in the metal [88] (Figure III-1). In reality, at a nonepitaxial metal-insulator interface there are inevitably random fluctuations in the electronic potential. The MIGS are particularly sensitive to these potential fluctuations, and a significant fraction of them–with single occupancy–becomes strongly localized near the interface, producing the observed paramagnetic spins. Fluctuations [89] of these local moments yield T-independent $1/f$ flux noise.

(b) Theory and computation

To illustrate the effects of potential fluctuations on the MIGS we start with a tight-binding model for the metal-insulator interface, consisting of the (100) face of a simple-cubic metal epitaxially joined to the (100) face of an insulator in a CsCl structure (Figure III-2a). For the metal we assume a single s-orbital per unit cell and nearest neighbor (NN) hopping. For the insulator we place an s-orbital on each of the two basis sites of the CsCl structure and assume both NN and next-nearest neighbor (NNN) hopping. The parameters are chosen so that the metal s-orbitals are at zero energy and connected by a NN hopping energy of -0.83 eV. The onsite energy of the orbitals on the Cs and Cl sites is taken to be -4 eV and 2 eV, respectively, and both the NN and NNN hopping energies are set to -0.5 eV. These parameters yield a band width of 10 eV for the metal, and 8 and 4 eV band widths, respectively, for the valence and conduction bands of the insulator with a band gap of 2 eV (Figure III-2d). These band structure values are typical for conventional metals and for semiconductors and insulators. For the interface we take the hopping energy between the metallic and insulating atoms closest to the interface to be -0.67 eV, the arithmetic mean of -0.83 and -0.5 eV.

The electronic structure of the ideal metal-insulator junction is calculated using a supercell [90] containing 20 × 20 × 20 metal unit cells and 20 × 20 × 20 insulator unit cells, a total of 24,000 atoms. The total density of states (DOS) of the supercell (Figure III-2e) shows a nearly flat DOS in the band gap region. The states in the insulator band gap are MIGS that are extended in the metal, decaying rapidly away from the interface into the insulator. Our model with a lattice constant of 0.15 nm yields an areal density of states for the MIGS of about $3\times10^{18}\text{eV}^{-1}\,\text{m}^{-2}$, consistent with earlier self-consistent pseudopotential calculations [91].

To mimic the effects of interfacial randomness, we allow the onsite energy to fluctuate for both metal and insulator atoms near the interface [92]. Specifically we assume an energy distribution $P(E) = (1/\sqrt{2\pi}\delta)exp[-(E - E_0)^2/2\delta^2]$, where E_0 is the original onsite energy without disorder, and δ is the standard deviation. We characterize the degree of disorder by the dimensionless ratio $R = 2\delta/W$, where W is the bandwidth of the metal. For those MIGS that become localized, the energy cost, U_i, for double occupation is large, and we cannot use a noninteracting electron approach. Instead we adopt a strategy similar to that used by Anderson in his calculation of local moment formation [5]. We separate the space near the interface into 3 regions: (i) the perfect metal region (M), (ii) an interfacial region consisting of 2 layers of metal unit cells and 2 layers of insulator unit cells (D) (Figure III-2b), and (iii) the perfect insulator region (I). Region (ii) is analogous to the impurity in Anderson's analysis.

We first compute the single-particle eigenstates, $\phi_i(\mathbf{r})$, of region D *in isolation*. For each of these states, we calculate the Hubbard energy U_i for double occupation for states in the isolated D region by evaluating the integral

$$U_i = \int_D d\mathbf{r}d\mathbf{r}' \frac{\left|\phi_{i\uparrow}(\mathbf{r})\right|^2 \left|\phi_{i\downarrow}(\mathbf{r}')\right|^2}{\left|\mathbf{r}-\mathbf{r}'\right|} \qquad \text{(II-69)}$$

over the supercell. Within our tight-binding supercell scheme, two additional factors need to be included. (i) The part of the Coulomb integral on the same atomic site is replaced with the

value of an onsite Hubbard U_0 = 10 eV. (ii) When the localization length (ξ) of the localized states is larger than the supercell size, there is overlap of wavefunctions from the neighboring supercell; this overestimates U_i for the very weakly localized states. Given that the participation number, $P_i = 1/\mathrm{P}_j |\phi_i(\mathbf{r}_j)|^4 \sim (\xi_i/a)^d$ in a disordered d-dimensional system with supercell lattice constant a and $U_i \propto 1/\xi_i$, we map the U_i value of the finite supercell onto that of an infinite supercell using a scaling law [93] for ξ. The hybridization-energy broadening of the localized states arises from couplings to the extended states in the metal as well as those in the insulator, and is given by

$$\Gamma_i = \Gamma_i^M + \Gamma_i^I \qquad \text{(II-70)}$$

with

$$\Gamma_i^{M(I)} = \pi \left| V_i^{M(I)} \right|_{ave}^2 \rho^{M(I)}(E) \quad \text{(II-71)}$$

where $\rho^{M(I)}(E)$ is the density of extended states in M (I) at the energy of the localized state E, and $V_i^{M(I)}$ is the hopping matrix element between an extended state in M(I) and a localized state in D (*ave* indicates averaging over the extended states). Extended eigenstates in M(I) are a linear combination of constituent orbitals; the $V_i^{M(I)}$ can then be expressed in terms of the coupling of these orbitals to those in D. For example, the localized states inside the band gap of the insulator are hybridized with only extended states in M, and $\Gamma_i = \Gamma_i^M \simeq \pi V^2 d_i / W$. (Here d_i is the charge of the localized state $|i\rangle$ in the unit cell layer immediately adjacent to M.)

With the computed values of U_i and Γ_i, we solve Anderson's equation for the spin-dependent occupation for spin-dependent occupation for each localized state

$$\langle n_{i\sigma} \rangle = \frac{1}{\pi} \int_{\infty}^{E_F} dE' \frac{\Gamma_i}{(E' - E_{i\sigma})^2 + \Gamma_i^2}. \qquad \text{(II-72)}$$

Here, $E_{i,\sigma} = E_i + U_i \langle n_{i,-\sigma} \rangle$ and σ is the spin index. The net moment associated with the state is given by $m_i = \mu_B |\langle n_{i,\sigma} \rangle - \langle n_{i,-\sigma} \rangle|$. Eq. (II-72) and the associated expression for the net moment of the localized states are calculated within the self-consistent Hartree-Fock approximation [5]. An $m_i \neq 0$ solution is obtained only when $U_i/(E_F - E_i)$ exceeds a critical value which depends on $\Gamma_i/(E_F - E_i)$. In the large U_i limit, it is more appropriate to start from the weak coupling limit ($\Gamma_i = 0$), where the localized state is populated by a single electron, and treat Γ_i as a perturbation. By calculating the areal density of such moment-bearing localized states we estimate the density of spin-1/2 local moments.

(c) Results and Discussion

Figure III-3 shows the calculated distribution $\rho(E,U)$ in the isolated interfacial region for R= 0.05, 0.1, 0.15, 0.2, 0.25, and 0.3; for each value, higher values of U correspond to more

localized states. As expected we see that, for any given degree of randomness, the states with energy inside the insulator band gap (the MIGS) or those at the band edges are most susceptible to localization. Figure III-4 shows a perspective plot of the charge density of two states, with high and low values of U_i, showing the correlation between the degree of wavefunction localization and the value of U_i. Both states are centered in the insulator, a general characteristic of localized states in the band gap originating from the MIGS.

Setting the Fermi energy at the insulator midgap value, we estimate the areal density of spins for a given degree of randomness R. The top panel in Figure III-5 depicts the distribution $\rho(E,m)$ of the spin moments as a function of energy. We see that for small R virtually all the local moments are derived from the MIGS. The bottom panel of Figure III-5 shows the calculated areal density of local moments versus R. Our simple model thus indicates that moderate potential fluctuations ($R \sim 0.15$) at the interface produce an areal density of localized moments comparable to experimental values. If one includes the effect of metallic screening from region M on U_i, [94] U_i would decrease by a factor of roughly 2 since the localized state in region I is located on average $\sim$ 3 unit cell layers from region M. We estimate this effect reduces the spin density by $\sim$ 50% at each R value. As a result, R should be increased by at most 10% to produce an areal density of $\sim 5 \times 10^{17} m^{-2}$.

Although our analysis is for a specific model, we expect the general physical picture to remain valid for real materials. First, the formation of MIGS at a metal-insulator interface is universal, and their areal density is rather insensitive to the nature of the materials [91]. We give a simple estimate of the areal density of MIGS. In a two-band tight-binding model [95], the amplitude squared of the evanescent solutions [96] close to the valence band edge has an energy-dependent decay length $\beta(E) = 2[2m^*(E - E_{VBM})/\hbar^2]^{1/2}$, where m^* is the electron effective mass and E_{VBM} is the energy of the valence band maximum. Near the conduction band edge E_{CBM}, $\beta(E) = 2[2m^*(E_{CBM} - E)/\hbar^2]^{1/2}$. The areal density N of MIGS in the insulator (in units of states per unit area) is given by [88]

$$N = \int_0^{E_F} dE \int_0^{\infty} dz \eta(E) e^{-\beta(E)z} = \eta \int_0^{E_F} dE \frac{1}{\beta(E)} \quad \text{(II-73)}$$

where we have assumed the density of states $\eta(E)$ of the metal to be constant over the energy range of the band gap. Inserting the expression for $\beta(E)$ into Eq.(II-73), we obtain

$$N = \eta[(\hbar^2 / 2m^*)(E_F - E_{VBM})]^{1/2} \quad \text{(II-74)}$$

For most semiconductors and insulators [32], $m_e/m^* \approx 1 + C_1/E_g$ and $E_F - E_{VBM} = C_2 E_g$ with $C_1 \approx 10$ eV and $C_2 \approx 0.5$; furthermore, for most metals $\eta(E)$ is of the same of order of magnitude. Consequently, the approximate expression

$$N \approx \eta\left[\left(\hbar^2 / 2m_e\right) C_1 C_2\right]^{1/2} \quad \text{(II-75)}$$

is relatively insensitive to the nature of both the metal and the insulator. Using the typical values $\eta(E) \approx 2 \times 10^{28}\mathrm{m}^{-3}\mathrm{eV}^{-1}$ and $C_1C_2 \approx 5\mathrm{eV}$, we obtain $N \approx 8\times 10^{18}\mathrm{m}^{-2}$, in good agreement with pseudopotential calculation [91] for Al in contact with Si, GaAs or ZnS. Second, the formation of local moments from the combination of localized states and Coulomb interaction is a general phenomenon [5]. We also note that our analysis should not be significantly modified when the metal is superconducting. This is because the U_i for the localized states is generally much greater than the pairing gap. Of course, extended states with negligible U_i would be paired.

Given our picture of the origin of the localized spin-$\frac{1}{2}$ moments, how do they produce $1/f$ flux noise with a spectral density $S_\Phi(f) \propto 1/f^\alpha$? The local moments interact via mechanisms such as direct superexchange and the RKKY interaction [85,97–99] between themselves, and Kondo exchange with the quasiparticles in the superconductor. This system can exhibit a spinglass transition [100], which could account for the observed susceptibility cusp [86] near 55 mK. For $T > 55$ mK, however, experiments suggest that the spins are in thermal equilibrium [101] and exhibit a $1/T$ (Curie Law) static susceptibility [86,87]. In this temperature regime, for $hf << k_BT$ standard linear response theory [102] shows that the imaginary part of the dynamical susceptibility $\chi''(f,T) = A(f,T)(hf/k_BT)$. Here, $A(f,T) \propto \mathrm{P}_\mu \mathrm{P}_{\alpha\beta} P_\alpha \delta(hf + E_\alpha - E_\beta)|\langle\beta \mid S_\mu \mid \alpha\rangle|^2$, where S_μ is the μ-th component of the spin operator, α and β label the exact eigenstates, and P_α is the Boltzmann distribution associated with state α. Combining the above result with the fluctuation-dissipation theorem [89] which relates the flux noise to $\chi''(f,T)$, namely $S_\Phi(f,T) \propto (k_BT/hf)\chi''(f,T)$, we conclude that the observed $1/f^\alpha$ spectral density implies $A(f,T) \propto 1/f^\alpha (0.6 \leq \alpha \leq 1)$. Assuming low frequency contributions dominate the Kramers-Kronig transform, this result is consistent with the observed $1/T$ static susceptibility, and the recent measurement [103] showing that flux noise in a SQUID is highly correlated with fluctuations in its inductance, However, without knowing the form of the interaction between the spins, one cannot derive this behavior for $A(f,T)$ theoretically.

(d) Conclusion

In conclusion, we have presented a theory for the origin of the localized magnetic moments which have been shown experimentally to give rise to the ubiquitous low-T flux $1/f$ noise observed in SQUIDs and superconducting qubits. In particular we have shown that for a *generic* metal-insulator interface, disorder localizes a substantial fraction of the metal-induced gap states (MIGS), causing them to bear local moments. Although MIGS have been known to exist at metal-insulator interfaces for three decades, we believe this is the first understanding of their nature in the presence of strong local correlation and disorder. Provided T is above any possible spin glass transition, experiments show that fluctuations of these local moments produce a paramagnetic χ' and a power-law, f-dependent χ'' which in turn leads to flux $1/f$ noise. It is important to realize that localized MIGS occur not only at the metal-substrate interface but also at the interface between the metal and the oxide that inevitably forms on the surface of superconducting films such as aluminum and niobium. There are a number of open problems, for example, the precise interaction between the local moments, its relation to the value of α, and the possibility of a spin glass phase at low temperature. A particularly intriguing experimental issue to address is why different metals and substrates evidently have such similar values of R, around 0.15. Experimentally, to improve the performance of SQUIDs and

superconducting qubits we need to understand how to control and reduce the disorder at metal-insulator interfaces, for example, by growing the superconductor epitaxially on its substrate.

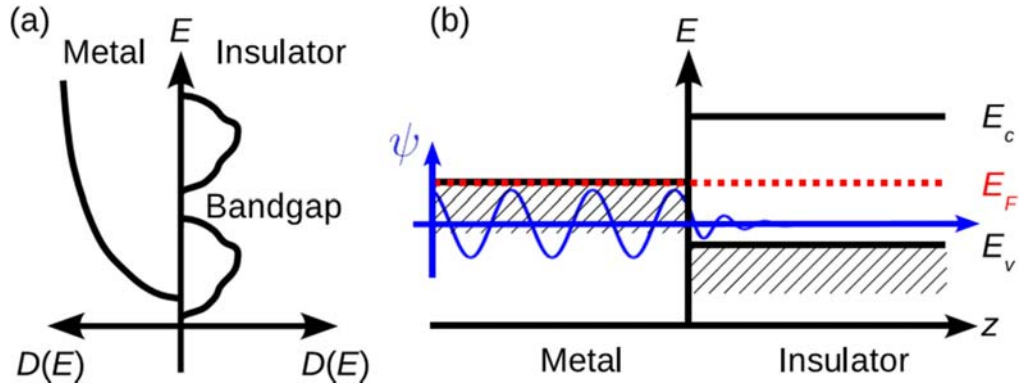

Figure III-1. (a) Schematic density of states. (b) MIGS at a perfect interface with energy in the band gap are extended in the metal and evanescent in the insulator.

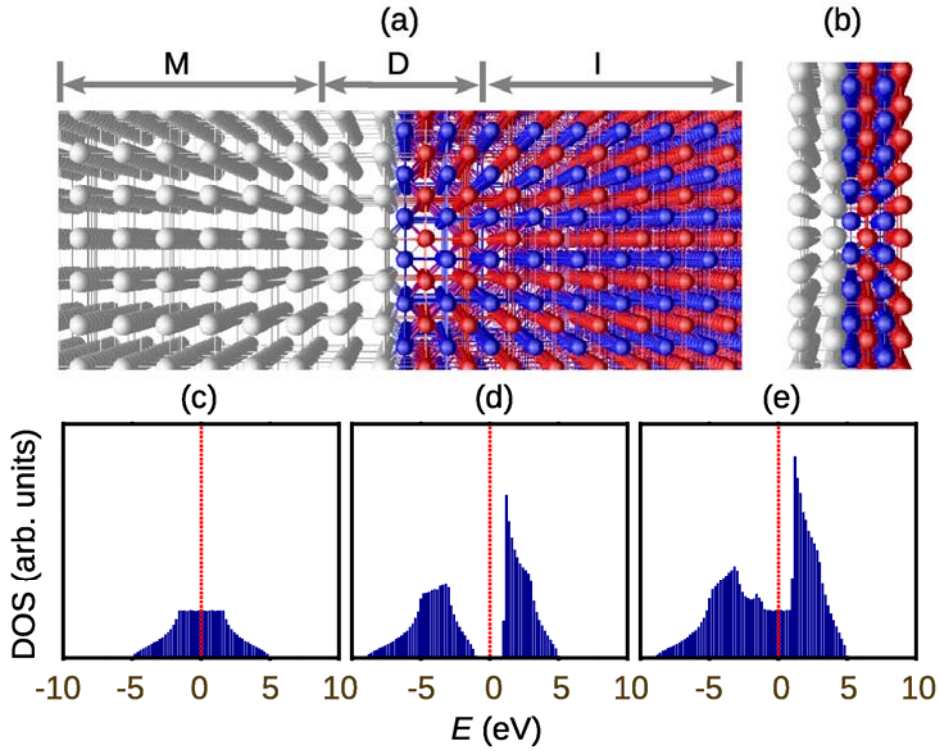

Figure III-2. (a) The metal (M) has a simple-cubic structure with one atom per unit cell and the insulator (I) a CsCl structure with two atoms per unit cell. (b) Interfacial region (D) consists of 2 layers of metal unit cells and 2 layers of insulator unit cells. The lattice constant is 0.15 nm. Computed DOS with Fermi energy (dotted red line) set to zero. (c) Typical metal with 10 eV bandwidth. (d) Typical insulator with a 2 eV band gap separating two bands of about 8 and 4 eV. (e) Metal-insulator interface with MIGS in the band gap of the insulator due to the presence of the metal.

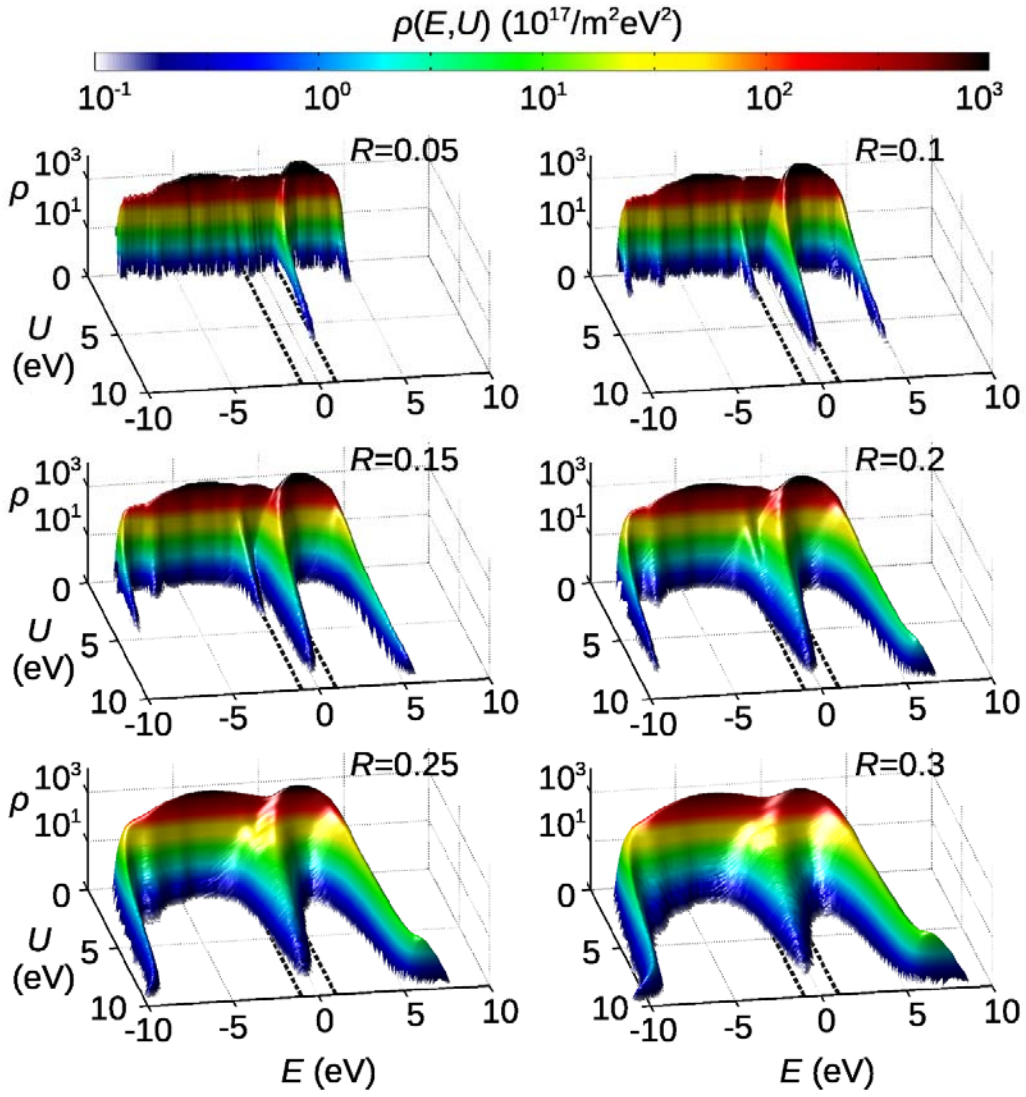

Figure III-3. Density of states distribution $\rho(E,U)$ as a function of energy E and Hubbard energy U for 6 values of the randomness parameter R in the isolated D region of Figure III-2. For a given value of R, the highest values of U, resulting in the most highly localized states, appear in the band gap of the insulator and at the band edges. The position of the insulator band gap is represented by black dashed lines

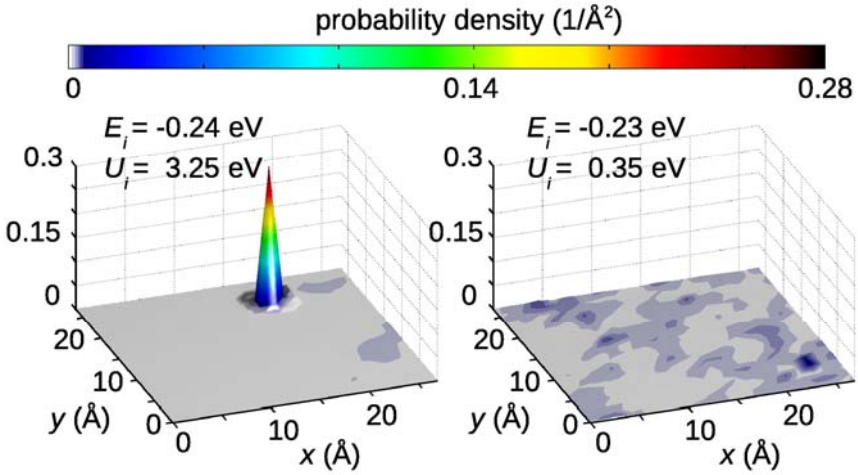

Figure III-4. Perspective view images of the two-dimensional probability density distribution at the interfacial region (D) along directions parallel to the interface (x and y directions), integrated along the z direction. (a) States with $U_i = 3.25 eV$ and $E_i = -0.24 eV$ and (b) with $U_i = 0.35 eV$ and $E_i = -0.23 eV$

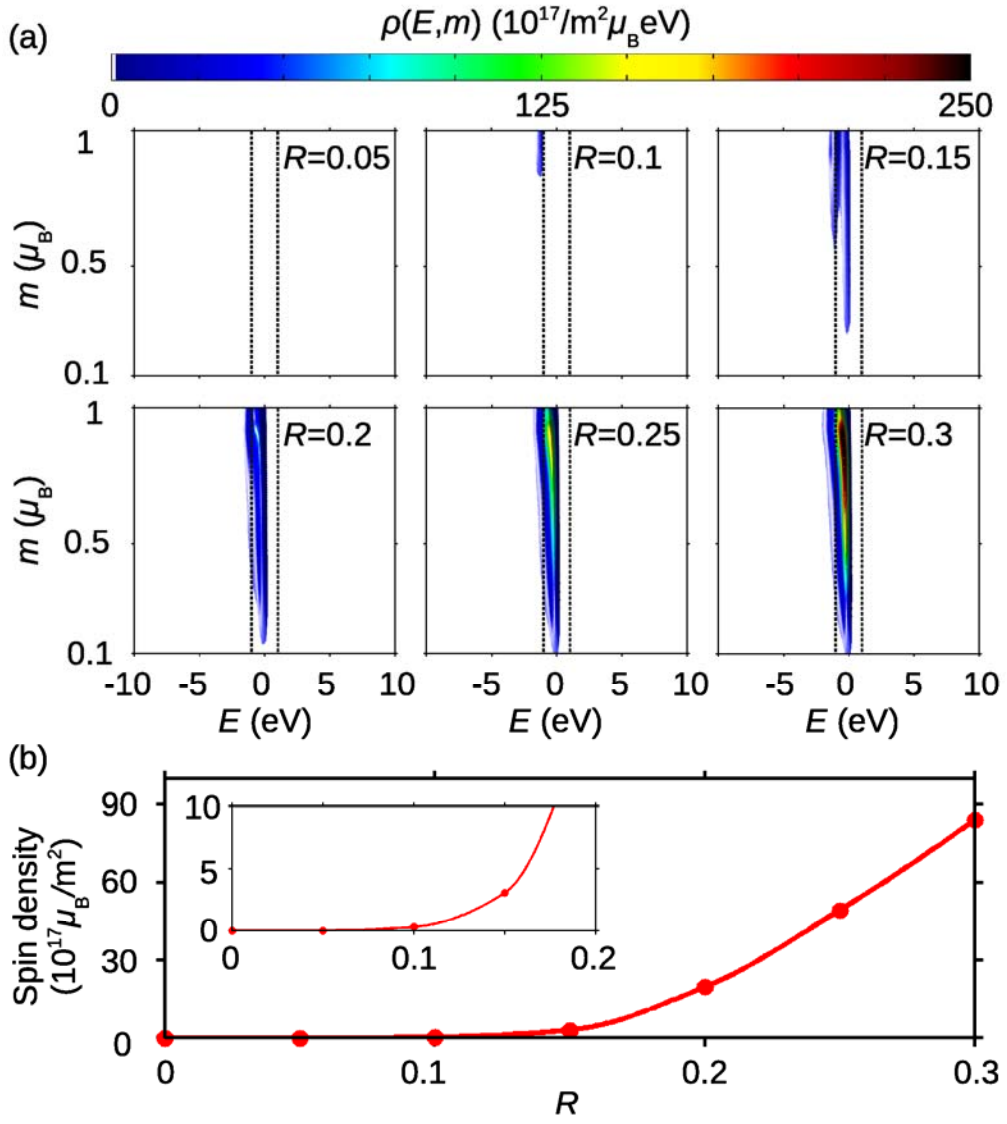

Figure III-5. (a) Electron density distribution $\rho(E,m)$ for 6 values of R. We simulated 5000 different configurations of disorder for each value of R. The position of the insulator band gap is represented by black dashed lines. Virtually all the magnetic moments are from the MIGS in the band gap of the insulator. (b) Integrated spin density versus randomness parameter R. For $R = 0.05$, we estimate the spin density to be less than $0.01 \times 10^{17} m^{-2}$.

2. Dielectric screening effects on local magnetic moment density at nonmagnetic metal-insulator interfaces

(a) Introduction

Local magnetic moments play an important role in many phenomena and devices. The presence of local magnetic moments is typically attributed to magnetic atoms such as those with partially-filled d or f shells. Strong local electron correlation in the partially-filled atomic d or f orbitals makes materials [5,104] with these atoms magnetic. There is however another origin of local magnetic moments: defects. One intriguing example is the moments at nonmagnetic metal-insulator interfaces [81,105]. Sendelbach et al. [86] showed that Nb/Al oxide/Nb SQUIDs are paramagnetic, with a Curie (1/T) susceptibility. Assuming the paramagnetic moments arise from localized electrons, they deduced an areal density of 5×10^{17} m^{-2}. Subsequently, Bluhm et al. [87] used a scanning SQUID microscope to measure the low temperature paramagnetic response of (nonsuperconducting) Au rings deposited on Si substrates and reported an areal density of $4\times10^{17}m^{-2}$. Paramagnetic moments were not observed on the bare Si substrate. Later experiments on different systems have also observed values of $\sim5\times10^{17}$ m^{-2} for the moments.

The universality of localized moment density of $\sim5\times10^{17}$ m^{-2} regardless of measurement and materials lead to the conclusion that the magnetic moments do not originate from impurities composed of the magnetic atoms. In our previous work [105], we argued that interfacial potential disorder localizes the metal-induced-gap states (MIGS) [88] at the interface, and strong electron-electron correlation effects at these localized MIGS lead to the formation of the local magnetic moments. The previous study gives the correct order of magnitude for the moment density but shows a dependence of the magnetic moment areal density on the magnitude of disorder; the aim of the present work is to address this issue.

(b)Theory and Computation

We work within in the same physical picture as in Ref. [105], i.e., localized MIGS give rise to the magnetic moments; but we evaluate the magnetic moment areal density using a more advanced method including dielectric screening effect, which was missing in our previous study. Since the volume near the metal-insulator junction consists of many electrons, these electrons polarize to screen any charge interactions. In particular, dielectric screening will decrease the Coulomb repulsion associated with doubly occupying localized MIGS at the interface. Therefore, it has a potential to weaken the dependence of the magnetic moment areal density on the disorder magnitude. Using a model Hamiltonian based on the tight-binding formalism and incorporating electron-electron interaction and disorder potential explicitly, we evaluated the magnetic moment areal density numerically.

We employed the following model Hamiltonian for the generic metal-insulator interface shown in Figure III-6(a):

$$H = H_M + H_I + H_{IF} + H_{M-IF} + H_{IF-I} \text{ .(II-76)}$$

The bulk metal Hamiltonian (H_M) is modeled as a simple cubic lattice with one s orbital basis at half-filling. In occupation number representation,

$$H_M = \sum_{\mathbf{R}} E_{\mathbf{R}}^M n_{\mathbf{R}} + \sum_{\langle \mathbf{R},\mathbf{R}' \rangle} t^M c_{\mathbf{R}}^\dagger c_{\mathbf{R}'}, \qquad \text{(II-77)}$$

where $\mathbf{R}$ is the lattice vector. Here $n_{\mathbf{R}}$, $c_{\mathbf{R}}^\dagger$, and $c_{\mathbf{R}}$ are electron number, creation and annihilation operator, respectively, at the orbital located at $\mathbf{R}$. The onsite energy of the metal s orbital $E_{\mathbf{R}}^M$ is set to be zero and nearest neighbor hopping integral t^M is set at -0.83 eV to yield a typical metal bandwidth of 10eV as shown in Figure III-6(b). The bulk insulator Hamiltonian (H_I) is modeled by CsCl crystal structure with two different s orbital basis at half-filling, i.e.,

$$H_I = \sum_{\mathbf{R}\tau} E_{\mathbf{R}\tau}^I n_{\mathbf{R}\tau} + \sum_{\langle \mathbf{R}\tau,\mathbf{R}'\tau' \rangle} t_{NN}^I c_{\mathbf{R}\tau}^\dagger c_{\mathbf{R}'\tau'} + \sum_{\langle\langle \mathbf{R}\tau,\mathbf{R}'\tau' \rangle\rangle} t_{NNN}^I c_{\mathbf{R}\tau}^\dagger c_{\mathbf{R}'\tau'}, \qquad \text{(II-78)}$$

where $\tau = 1$ or 2 is the basis index. The onsite energies of the two insulator s orbitals $E_{\mathbf{R}1}^I$ and $E_{\mathbf{R}2}^I$ are set to be -4eV and 2eV, respectively. The nearest neighbor (NN) hopping integral t_{NN}^I and the next nearest neighbor (NNN) hopping energy t_{NNN}^I in the insulator are set to $-0.5eV$. These parameter values are determined to yield a valence band width of 8eV, conduction band width of 4 eV, and a gap of 2 eV as shown in Figure III-6(c), which are representative of values in semiconductors and insulators.

The noninteracting interface Hamiltonian (H_{IF}^0) is modeled by a region consisting of two unit cell layers of the insulator and two unit cell layers of the metal. The hopping energy between metal atoms and insulator atoms closest to the interface is set to be -0.67eV, the arithmetic means of -0.5 eV and -0.83 eV. In contrast to H_I and H_M , it is essential to include disorder effect explicitly in the interface Hamiltonian (H_{IF}) to produce local magnetic moments. At a realistic interface, there are various sources of potential disorder such as lattice mismatch, dislocations, atomic diffusion between metal and insulators, and interface roughness. The disorder potential breaks translation symmetry in the interfacial region along the in-plane directions, and gives rise to scattering centers to electrons, resulting in the in-plane localization of electrons from Anderson's disorder theory [92]. In our study, the potential disorder at the interface is modeled by onsite energy fluctuations of the metal and insulator orbitals with a Gaussian distribution $P(E) = \left(1/\sqrt{2\pi\sigma}\right) \mathrm{e}^{-(E-E_0)^2/2\sigma^2}$, where σ is the standard deviation and E_0 is the original onsite energy. After the diagonalization of the isolated term H_{IF}^0 , H_{IF}^0 may be written as

$$H_{IF}^{0} = \sum_{i} E_{0,i} n_i \,, \qquad \text{(II-79)}$$

where i is the index for the eigenstates with eigenenergy of $E_{0,i}$ is the energy of the ith eigenstates.

The localization of electron wavefunctions at the interface requires explicit treatment of electron-electron interaction. The spatial extent of electron wavefunction determines the energy cost for double occupation of the wavefunction due to the repulsive Coulomb interaction between the two electrons. We may evaluate the repulsive Coulomb interaction associated with a wave function $\psi_i(\mathbf{r})$ of the isolated interfacial region in the static limit,

$$U_i = \int d\mathbf{r} d\mathbf{r}' \, |\psi_{i\uparrow}(\mathbf{r})|^2 \, W(\mathbf{r},\mathbf{r}') \, |\psi_{i\downarrow}(\mathbf{r}')|^2 \,, \qquad \text{(II-80)}$$

where $\uparrow$ and $\downarrow$ represent the two spin directions and $W(\mathbf{r},\mathbf{r}')$ is the screened Coulomb interaction in the static limit. The form of Eq. (II-80) shows that the smaller the electron wavefunction, the larger repulsive Coulomb interaction, since $W(\boldsymbol{r},\boldsymbol{r}')$ is a decreasing function of increasing $|\boldsymbol{r}-\boldsymbol{r}'|$. We calculate the screened Coulomb interaction in the following way. The screened Coulomb interaction is given by $\tilde{W} \simeq \left(\tilde{1} - \tilde{V}\tilde{\chi}^0\right)^{-1} \tilde{V}$ [102]. Here, "~" denotes a matrix in the basis of orbitals in the system, and $\tilde{1}$ is the identity matrix. The quantity $\tilde{V}$ is the usual bare Coulomb interaction which decays as $1/|\mathbf{r}-\mathbf{r}'|$, and we have regularized it to have a value of 10 eV when $\boldsymbol{r}$ and $\boldsymbol{r}'$ are on the same orbital. The polarizability $\tilde{\chi}^0$ is, within random phase approximation in the static limit, is given by

$$\chi^0_{\boldsymbol{R},\boldsymbol{R}'}(\omega = 0) = 2\sum_{i,j} \beta_{i\boldsymbol{R}} \beta^*_{j\boldsymbol{R}} \beta^*_{i\boldsymbol{R}'} \beta_{j\boldsymbol{R}'} \frac{f(E_{0,j}) - f(E_{0,i})}{E_{0,j} - E_{0,i}}, \quad \text{(II-81)}$$

where $\beta_{i\boldsymbol{R}}$ and E_i^0 are the tight-binding wavefunction coefficient and the noninteracting Hamiltonian energy of i th eigenstate, respectively. The term $f(E)$ is the Fermi-Dirac distribution function. In the calculation of $\tilde{\chi}^0$, if one neglects the hybridization between states in the metal region and interface region as well as in the insulator region and interface region, then the static polarizability may be simplified to

$$\tilde{\chi}^0 = \tilde{\chi}^{0,M+I} + \tilde{\chi}^{0,IF} \qquad \text{(II-82)}$$

with

$$\chi^{0,M+I}_{\mathbf{R},\mathbf{R}'} = 2\sum_{i,j\in M\cup I} \beta_{i\mathbf{R}}\beta^*_{j\mathbf{R}}\beta^*_{i\mathbf{R}'}\beta_{j\mathbf{R}'}\frac{f(E_{0,j})-f(E_{0,i})}{E_{0,j}-E_{0,i}} \qquad \text{(II-83)}$$

and

$$\chi^{0,IF}_{\mathbf{R},\mathbf{R}'} = 2\sum_{i,j\in IF} \beta_{i\mathbf{R}}\beta^*_{j\mathbf{R}}\beta^*_{i\mathbf{R}'}\beta_{j\mathbf{R}'}\frac{f(E_{0,j})-f(E_{0,i})}{E_{0,j}-E_{0,i}}. \qquad \text{(II-84)}$$

Here, M / I / IF in the summation of Eq. (II-83) and (II-84) represents the set composed of the eigenstates of H_M / H_I / H^0_{IF}, respectively. The screened Coulomb interaction is given by

$$\tilde{W}_{IF} = \left(\tilde{1} - \tilde{V}_{IF}\tilde{\chi}^0_{IF}\right)^{-1}\tilde{V}_{IF} \qquad \text{(II-85)}$$

with

$$\tilde{V}_{IF} \equiv \left(1 - \tilde{V}\tilde{\chi}^{0,M+I}\right)^{-1}\tilde{V} \quad . \qquad \text{(II-86)}$$

For simplicity we evaluate $\tilde{V}_{IF}$ using a classical image charge model [106], not by calculating Eq. (II-86) directly. This simplified model has shown to work well in other metal junction [107]. The nonlocal screening from the metal and insulator regions can be mimicked by putting image charges in the metal and insulator regions with appropriate charge magnitude. The two image planes are assumed to be at the metal-interface boundary and interface-insulator boundary, as shown in Figure III-7. In this classical model, if a point charge is residing on an orbital in the interface region, the screened Coulomb potential on another orbital in the interface region will be the sum of bare Coulomb potential from the point charge and its image charges shown in Figure III-7 (with an insulator dielectric constant ϵ_I).

From the screen Coulomb interaction W, we calculate the Coulomb repulsion associated with the double occupation of state i in the interface region, the extra interaction term U_i is included in a new interacting interface Hamiltonian which is now given by

$$H_{IF} = \sum_i \left(E_{0,i}n_i + U_i n_{i\uparrow}n_{i\downarrow}\right) \quad . \qquad \text{(II-87)}$$

Although this interface Hamiltonian does not incorporate all possible many-electron interaction terms in the exact many-body Hamiltonian, it includes the most dominant terms when an eigenstate of the noninteracting Hamiltonian, i, is localized. This assumption can also be justified by the observed magnetic moment areal density of 5×10^{17}m^{-2}. If we assume that they are from localized states at the interface, average distance between the localized states is ~ 1.4

nm. At this distance, the Coulomb repulsion between the nearest localized states should be one order of magnitude smaller than U_i.

We have included one further correction to our Hamiltonian rising from the finite supercell [90] size we use to construct the disorder in our numerical calculation. If the localization length ξ_i of the localized states at the interface region is larger than the supercell size L in the interface plane, there is overlap of wavefunctions in neighboring supercell. This will cause an overestimation of U_i for the very weakly localized states if it were calculated using only the amplitude of the wavefunction within a supercell. Using a scaling law [93] for the localization length ξ_i, we map the U_i value from a finite supercell calculation onto that of an infinite supercell. The localization length of each state is estimated by calculating the participation number, $P_i = 1 \Big/ \left(\sum_{\mathbf{r}} |\beta_{i\mathbf{r}}|^4 \right)$ which is known to be $\sim (\xi_i / L)^d$, where d is the dimension of the system.

The reformulated interface region-metal Hamiltonian (H_{M-IF}) and insulator-interface region Hamiltonian (H_{IF-I}) are modeled by electron hopping term between the orbitals in the metal and the insulator with the ith states in the interface region.

$$H_{M-IF} = \sum_{\langle \mathbf{R}i \rangle} \left(t_i^M c_{\mathbf{R}}^{\dagger} c_i + h.c. \right) \quad , \quad \text{(II-88)}$$

and

$$H_{IF-I} = \sum_{\langle \mathbf{R}\tau i \rangle} \left(t_{NN,i}^I c_{\mathbf{R}\tau}^{\dagger} c_i + h.c. \right) + \sum_{\langle\langle \mathbf{R}\tau i \rangle\rangle} \left(t_{NNN,i}^I c_{\mathbf{R}\tau}^{\dagger} c_i + h.c. \right) \quad , \quad \text{(II-89)}$$

where t_i^M are hopping integral between an orbital on a metal atom and the state i in the interface region, and $t_{NN,i}^I$ and $t_{NNN,i}^I$ are nearest neighbor and next nearest neighbor hopping integrals between an orbital on the insulator atom and the state i in the interface region.

The total Hamiltonian in Eq. (II-76) with the new terms is analogous to the Anderson impurity Hamiltonian [5]. To illustrate, the states in the interface region are analogous to the localized d orbital state and the metal and insulator band states here are analogous to the extended s band states in the Anderson model. From this similarity, we can apply our understanding of Anderson impurity Hamiltonian to our Hamiltonian for the evaluation of magnetic moments associated with the localized states at the interface region. For the interface Hamiltonian H_{IF} in Eq. (II-87), the Coulomb repulsion associated with double occupation of the eigenstates favors the formation of local magnetic moments because it hinders double occupancies. On the other hand, the hybridization between eigenstates of H_{IF} and extended states in the metal tend to interrupt the formation of moments. This hybridization energy associated with the eigenstate i is given by [5]

$$\Delta_i = \pi \sum_{\mathbf{k}} \left| \langle i | H_{M-IF} | \mathbf{k}^M \rangle \right|^2 \delta(E_i - E_{\mathbf{k}}^M) + \pi \sum_{\nu\mathbf{k}} \left| \langle i | H_{I-IF} | \nu\mathbf{k} \rangle \right|^2 \delta(E_i - E_{\nu\mathbf{k}}^I) \quad \text{(II-90)}$$

where $\left|\mathbf{k}^M\right\rangle \left(\left|\nu\mathbf{k}^I\right\rangle\right)$ and $E_{\mathbf{k}}^M \left(E_{\nu\mathbf{k}}^I\right)$ are an eigenstate and its eigenenergy of $H_M \left(H_I\right)$. With the three parameters of $E_{0,i}$, U_i, and Δ_i for state i in the interface region, we calculate the expectation value of electron density using [5]

$$\left\langle n_{i,\sigma} \right\rangle = \frac{1}{\pi} \int_{-\infty}^{E_F} dE \frac{\Delta_i}{(E - E_{i,\sigma})^2 + \Delta_i^2} \quad \text{(II-91)}$$

(derived within Hartree-Fock approximation), where $E_{i,\sigma} = E_{i,0} + U \left\langle n_{i,-\sigma} \right\rangle$ and σ is spin index. Then the net magnetic moment for the ith localized state is given by $m_i = \mu_B \left| n_{i,\uparrow} - n_{i,\downarrow} \right|$

(c)Results and Discussion

Setting the Fermi energy at the insulator midgap value, we have evaluated with the above model the areal density of magnetic moments for a given degree of randomness R using a 500 member ensemble average. We characterize the degree of disorder by the dimensionless ratio $R = 2\sigma / W$, where W is the bandwidth of the metal. The interface Hamiltonian is modeled using a supercell containing 20 × 20 × 2 metal unit cells and 20 × 20 × 2 insulator unit cells, with a total of 2,400 atoms. Figure III-8(a) shows the magnetic moment areal density as a function of R. If we don't incorporate dielectric screening in evaluating the Coulomb repulsion associated with the states at the interface (marked by red color), the magnetic moment areal density is rapidly increasing function of R. Although the magnetic moment areal density agrees with experimentally measured moment density of $5 \times 10^{17} m^{-2}$ (grey dashed line) at $R \simeq 0.15$, the steep slope in Figure III-8(a) disagrees with the observed insensitivity of the measured magnetic moment density to the interface conditions. However, if we incorporate dielectric screening in calculating the Coulomb repulsion associated with the doubly occupying the eigenstates in the interfaces region (with $\epsilon_I = 12$), the magnetic moment areal density saturates to a maximum value of $4 \times 10^{17} m^{-2}$, in a good agreement with experiments.

Further the calculated maximum value of $4 \times 10^{17} m^{-2}$ is relatively insensitive to the dielectric constant of insulator used. As shown in Figure III-8(b), the calculated magnetic moment areal density at each R doesn't change much when we change ϵ_I from 4 to 12. This is because the magnitude of the image charge changes slowly as ϵ_I changes. For example, the charge of the first image charge in the insulator region is given by $(\epsilon_I - 1)\mathrm{q}/(\epsilon_I + 1)$. If we increase ϵ_I 3 times from 4 to 12, the charge of this image charge increases by only 40%.

To understand the physical origin of the local magnetic moment, we calculated the magnetic moment weighted electron areal density of states in the interface region

$$\rho_m(E,m) = \sum_i m\,\delta(E - E_{0,i})\delta(m - m_i) / \mathrm{A} \quad . \quad \text{(II-92)}$$

where A is the area of interface plane in the sample and $E_{0,i}$ is noninteracting interface Hamiltonian energy. Figure III-8(c) shows the calculated $\rho_m(E,m)$ for R=0.2 and 0.3 from a 500 ensemble average. We see all the magnetic moment is originated from the states of which the energy from the noninteracting Hamiltonian is in the bandgap of the insulator (marked by black dashed lines), confirming that the magnetic moment are derived from the disorder-induced localized MIGS. As R increases from 0.2 to 0.3, all the magnetic moments are still from the states in the bandgap of the insulator.

(d)Conclusion

To summarize, using the screened Hartree-Fock solution of a model Hamiltonian including double occupancy Coulomb repulsion of states, we show that metal-induced gap states at the interfaces are prone to be localized by disorder and that the localized metal-induced gap states are magnetic due to electron-electron interactions. The magnetic moment areal density is saturated to its maximum value of $4\times10^{17}\,m^{-2}$ as the disorder increases, consistent with the experimental observation of having an universal value for the measured moment areal density in different systems. Dielectric screening effect is found to be essential for explaining this universal behavior.

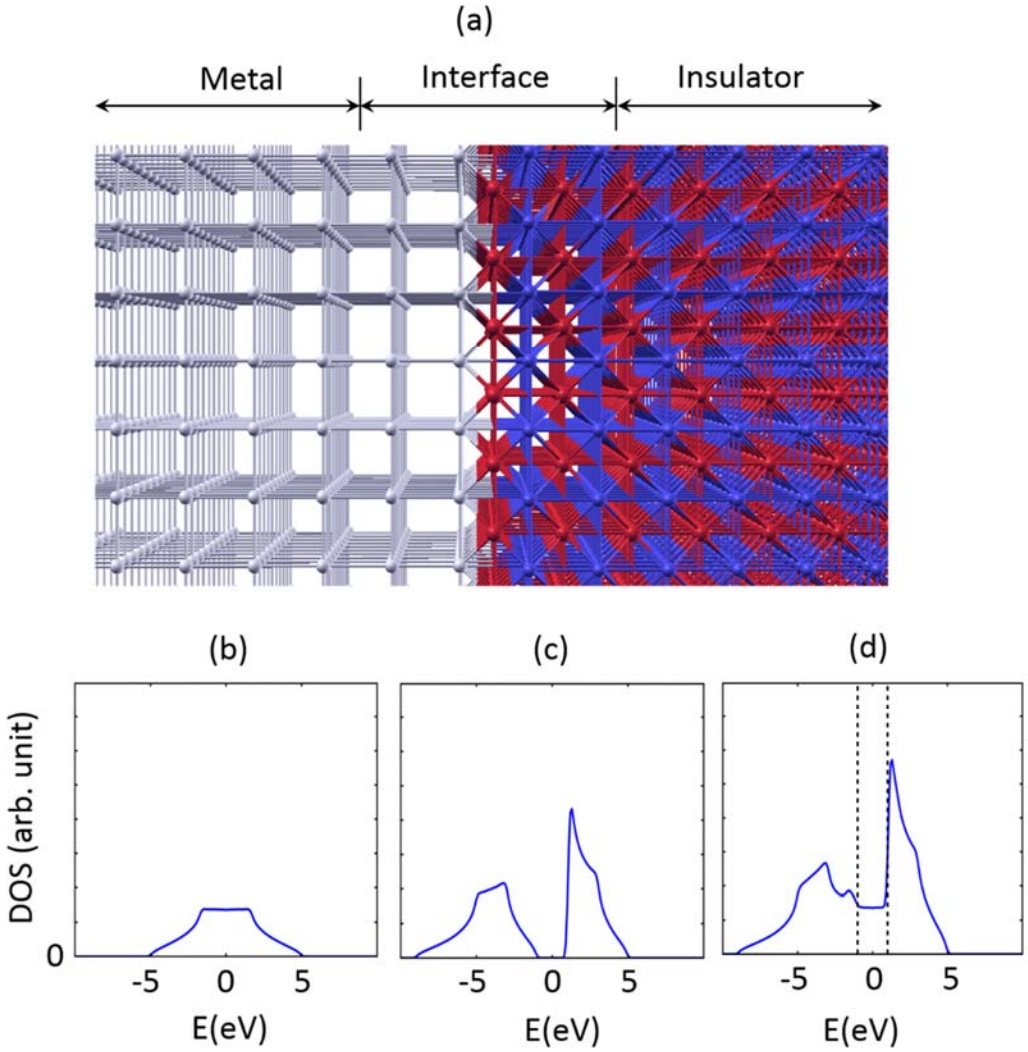

Figure III-6 (a) Atomic geometry of a model metal-insulator interface. The bulk metal is modeled by a simple-cubic lattice with one s orbital, and the bulk insulator is modeled by a CsCl structure with two different s orbitals per unit cell. Interfacial region consists of 2 layers of metal unit cells and 2 layers of insulator unit cells. The lattice constant is set to 1.5 $\mathring{A}$, to yield a typical areal density of states for the MIGS of $\sim 3\times 10^{18}\ m^{-2}$. Computed DOS of (a) bulk metal with 10 eV bandwidth, (b) bulk insulator with a 2 eV band gap separating two bands, one with a bandwidth of 8 eV and the other with a bandwidth of 4 eV, and (c) the metal-insulator interface. The Fermi level is set at 0 eV.

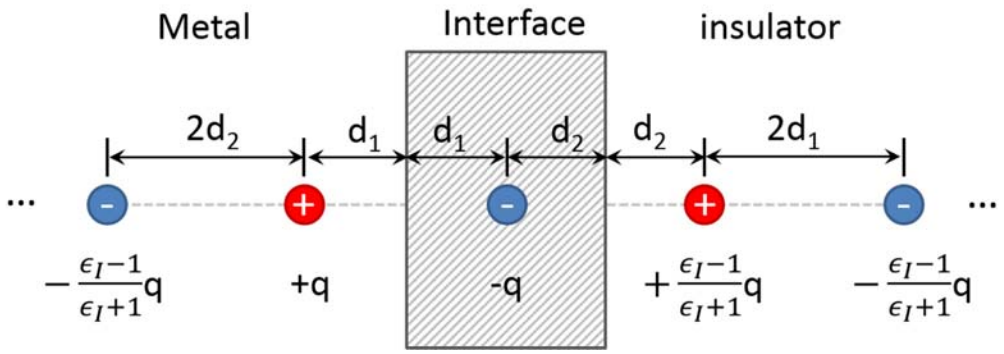

Figure III-7 dielectric screening model of disordered metal-insulator interface. The dielectric screening from the bulk metal and insulator has been incorporated within a classical image charge model. The dielectric constant of the insulator is set to ϵ_I. Higher order image charges going beyond the two primary image charges are also included. The dielectric screening from the localized electron in the interface region is separately included using a polarizability calculated within the random phase approximation in the static limit.

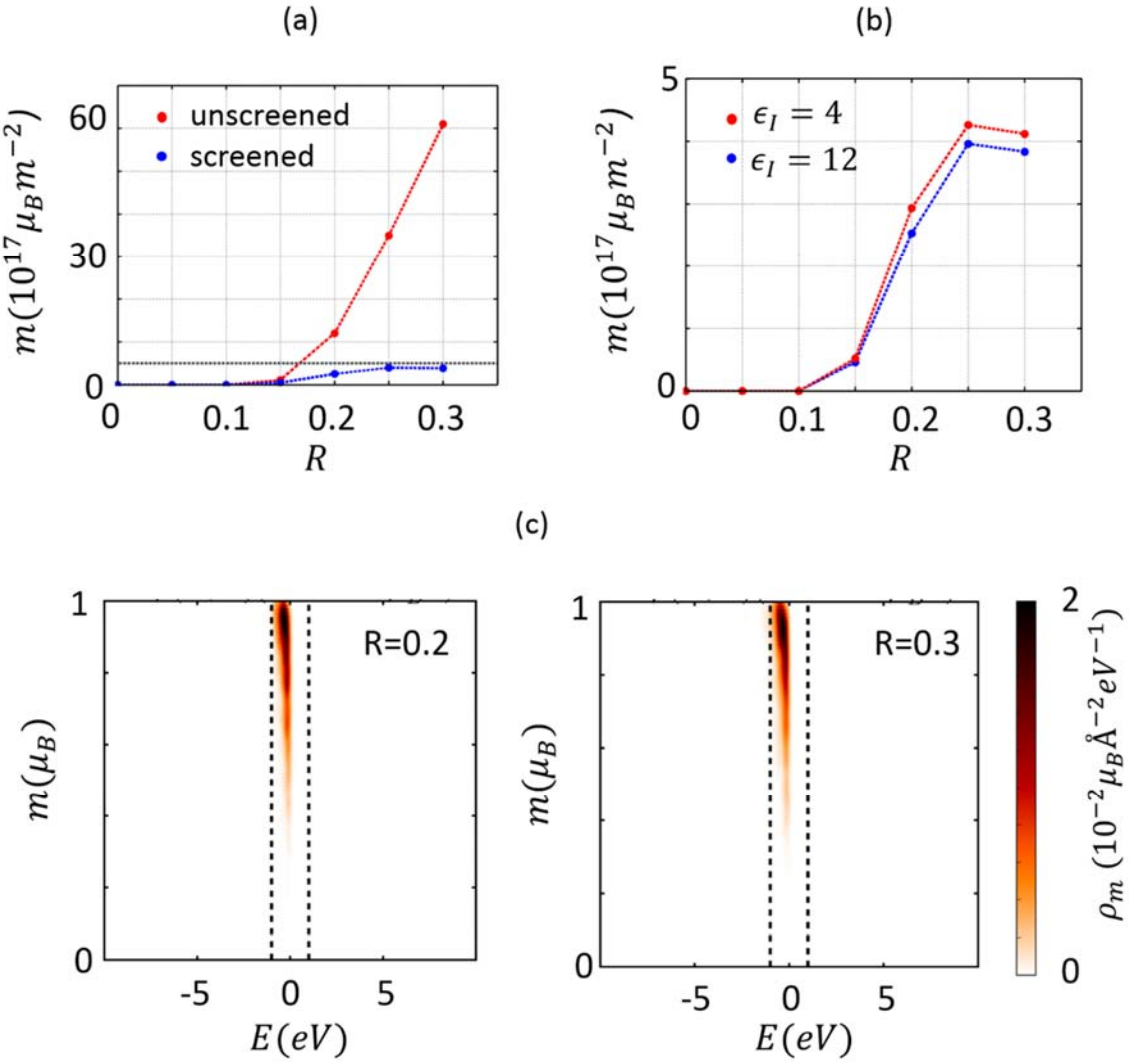

Figure III-8 (a) (a) The effect of dielectric screening on the magnetic moment areal density as a function of the dimensional-less parameter R which characterizes the interfacial disorder. Red and blue dots show calculated magnetic moment areal density with and without dielectric screening effects. An insulator dielectric constant of $\epsilon_I = 12$ is used. (b) The effect of changing ϵ_I on the magnetic moment areal density against R. (c) Magnetic moment weighted electron density of states as a function of energy E and magnetic moment (m) with $\epsilon_I = 12$ at R=0.1 and R=0.2.

IV. **Defects**

1. Mechanism for optical initialization of spin in NV^- center in diamond

(a) Introduction

NV^- in diamond is a defect complex composed of a substitutional nitrogen atom and an adjacent carbon vacancy [108,109] as shown in Figure IV-1. NV^- has emerged as one of the best candidates for realization of individually addressable spins in the solid state for quantum computing and other studies [110–119]. The interest in this system in large part stems from an optical initialization process under ambient conditions, which results in a state with long spin coherence time of up to ~ 1 ms [120]. The optical initialization of the NV^- center, which starts with a degenerate mixed triplet ground state, involves optical transition to an excited state and subsequent relaxations to a specific ground state with an un-entangled pure spin of m_s=0. The detailed electronic structure of the low-energy excited states, especially the placement of possible singlet defect levels with respect to the ground ($^3A_2$) and first excited triplet (^3E) levels, is crucial in explaining the optical initialization mechanism. However, up to now there is no consensus. It is reported experimentally that two singlet levels ($^1A_1$ and ^1E) are near the ground and the first excited triplet levels, but the character and ordering of the two singlet levels are not determined [121,122]. Various theoretical studies also failed to agree with each other [123–129]. There are several different optical initialization pictures in the literature. The most widely used picture, where one singlet level ($^1A_1$) is assumed to lie in between the two lowest-lying triplet levels [130–132], has not been confirmed. There exist two different "two active singlet level" models [122–124] involving an intermediate step of radiative decay between two singlet levels of $^1A_1$ and ^1E symmetry before the system decays to the ground state. However these models are in contradiction with the experimental findings which show that after the initially excited triplet level decayed to a singlet state, the system decays nonradiatively [121,122].

The main theoretical difficulty in determining the nature of this system arises from the fact that NV^- is a deep-level center in the band gap of diamond with multiple localized, interacting electrons. Such systems are not appropriate for mean-field type of calculations because of strong electron-electron interaction. Alternatively, mimicking the system as a small isolated diamond cluster with a NV^- defect without additional input is also expected to be not so appropriate because it does not include the large screening effects from the bulk and because of issues with possible spurious boundary effects. Furthermore, this defect is prone to large excited-state structural relaxation [123,126,133]. An effective model Hamiltonian with reliable interaction parameters for the electrons, such as an extended Hubbard model, offers an efficient way to evaluate the excited-state level structure which could include many-electron interactions fully if solved exactly. In such models, the electron-electron interaction and screening effect of the host material however must be accurately incorporated using effective Coulomb interaction parameters. The effects of structural relaxation should also be taken into account through the

parameters. Such approaches had been hindered in the past by the difficulty in getting physically grounded model parameters.

In this study, we employ an extended Hubbard model Hamiltonian with structure-dependent interaction parameters that are derived from *ab intio* quasiparticle energy levels. These parameters are put on physical grounds by fitting the quasiparticle excitation energies of the model system to those of the real system, both calculated within the same GW approximation to the electron self-energy operator [19,134]. The idea is to use relevant physical quantities, and a sufficient number of them, to accurately determine the effective electron-electron interactions.

(b) Theory and computation

For the real system, we calculated from first principles the ground-state using density functional theory in the local spin density approximation (DFT-LSDA) and the low-energy excited-state quasiparticle levels using the *ab initio* GW method. To obtain the ground-state equilibrium geometry (GEG) of NV^- in diamond, we performed *ab initio* calculations within the pseudopotential density functional theory (DFT) framework. We used the local spin density approximation (LSDA) to the exchange correlation functional. Norm-conserving pseudopotentials were used with a plane wave basis (80 Ry cutoff) for structural relaxations. The defect system was modeled with a supercell containing 214 carbon and 1 nitrogen atoms [135]. We then calculated the quasiparticle energies of the NV^- within the GW approximation to the electron self energy following the method of Hybertsen and Louie [19,134]. For these calculations, we used a dielectric matrix cutoff of 10 Ry and 3990 bands in the evaluation of the polarizability and self-energy operator. Our *ab initio* GW quasiparticle level diagram at the ground-state equilibrium geometry (GEG) of the NV^- center is shown in Figure IV-1b. There are 8 quasiparticle defect states near the band gap. These defect states, which are localized at the defect site, should form an efficient basis set for describing the low-energy charge-conserved excitations that are of the main interest of the present study.

We therefore chose the Hilbert space for the effective model system to be spanned by the 8 dangling-bond spin orbitals centered at the 3 carbon atoms and the one nitrogen atom nearest to the vacancy site [136]. To ensure that such a basis would describe the lowest lying excitations well, we constructed maximally localized Wannier functions from the *ab initio* wavefunctions out of above mentioned 8 defect states [137]. As is evident from Figure IV-2, the Wannier functions are strongly localized at the atoms nearest to the vacancy, showing dangling bond characteristics and justifying our choice of an 8 atom-centered spin-orbital Hilbert space. It also shows that hybridization of the *u* states and the extended state in the valence band is small. Simple electron counting dictates that 6 electrons be shared amongst these 8 spin-orbitals for the NV^-: 3 electrons from the 3 carbon atoms, 2 electrons from the nitrogen atom, and 1 added electron from the defect being negative charged. The effective Hamiltonian hence is taken as:

$$H = \sum_{\substack{i=\{C,N\} \\ \sigma=\{\uparrow,\downarrow\}}} E_i n_{i\sigma} + \sum_{\substack{i\neq j=\{C,N\} \\ \sigma=\{\uparrow,\downarrow\}}} t_{ij} c_{i\sigma}^{\dagger} c_{j\sigma} + \sum_{i=\{C,N\}} U n_{i\uparrow} n_{i\downarrow} + \frac{1}{2} \sum_{\substack{i\neq j=\{C,N\} \\ \sigma,\sigma'=\{\uparrow,\downarrow\}}} V n_{i\sigma} n_{i\sigma'} \quad \text{(II-93)}$$

where $c_{i,\sigma}^{\dagger}$, $c_{i,\sigma}$,and $n_{i,\sigma}^{\dagger}$ are creation, annihilation, and number operators at the site *i* with spin σ.

It should be noted that while this model does not include all possible electron-electron interaction terms in the exact many-body Hamiltonian, it includes the *two dominant* terms when the Hilbert space is spanned by an atom-centered basis set [28], namely, the onsite-Coulomb repulsion (U) as well as the nearest neighbor Coulomb repulsion (V) term. Further simplifications have been made to the model Hamiltonian parameters by examining the Wannier functions corresponding to the 8 defect states. As shown in the Figure IV-2, the Wannier functions centered at the carbon atoms and the nitrogen atom are all similar in shape and size. Their mean radii, which are defined as $\sqrt{\langle W||\vec{r}|^2|W\rangle - |\langle W|\vec{r}|W\rangle|^2}$ where $\vec{r}$ is the position operator, are within 5% of one another. The mean radius is 2.0 Å for the up-spin orbital of nitrogen, 1.9 Å for the up-spin orbital of carbon, 1.9 Å for the down-spin orbital of nitrogen, and 1.8 Å for the down-spin orbital of carbon. Based on this, we constrain that the onsite Coulomb repulsion (U) for carbon and nitrogen are the same, and that the carbon-nitrogen nearest-neighbor Coulomb repulsions and carbon-carbon nearest-neighbor Coulomb-repulsions (V) are also all the same.

We determined the parameters in Eq. (II-93) by comparing the quasiparticle energies calculated within the *ab initio* GW approach to those from a GW calculation of our model Hamiltonian at the GEG. To calculate the quasiparticle energies for the extended Hubbard model with a given set of interaction parameters, we use the DFT-LSDA as the mean-field starting point [28,138,139]. We calculated the quasiparticle self-energy correction to the mean-field solution within the GW approximation. This is exactly the same level of approximation as the *ab initio* GW quasiparticle calculation for the real system. We tuned the model parameters (Table IV-1) until we minimize the differences between the model Hamiltonian quasiparticle energy levels and the *ab initio* quasiparticle levels. As seen in Figure IV-1b, the quasiparticle energies from our extended Hubbard model match the *ab initio* values to within 0.1eV.

The interaction parameters in Table IV-1 are physically well-determined because the two Hamiltonians (model and real) are treated in equal footing with important self-energy effects incorporated. Because nitrogen has a larger atomic number than carbon, as expected, the onsite energy of nitrogen is lower than that of carbon (E_C-E_N > 0). The transfer integrals (t_{NC} and t_{CC}) are close to a value from a Wannier function analysis (which is -0.7 eV). The onsite Coulomb repulsion is also reasonable; the bare onsite Coulomb repulsion of π electrons in carbon nanotube is ~ 16 eV [140] but for NV^- in diamond it is screened by the dielectric constant of diamond of 5.5 [141].

To understand the optical initialization process, it is important to include this Frank-Condon relaxation. To account for this effect, we first calculated the excited-state equilibrium geometry (EEG) for the ^3E state of NV^- in diamond within an *ab initio* constrained DFT framework by depopulating the $\bar{v}$ level and populating either the $\bar{e}_x$ or $\bar{e}_y$ level. The overlap of $^3A_2$ and ^3E many-body states from exact diagonalization with the model single Slater determinant listed in Table IV-2 at GEG and EEG are more than 0.98, which justifies our geometric relaxation calculation by constrained DFT, which assumes a single Slater determinant many-body state. At the EEG, N moves toward the vacancy by 0.05Å while the three C nearest to the vacancy move outwards from the vacancy by 0.06Å. We re-evaluated the

model parameters following the same procedure as for the GEG. Because the structural change between GEG and EEG is small (Figure IV-3a), we may safely assume that the minimum-energy path between the two geometries can be explored by using parameters that are linear interpolations of the values from the two end points – the GEG and EEG. The parameters at the GEG and EEG are given in Table IV-1.

(c) Results and discussion

Having parameterized the model Hamiltonian, we calculated the many-body eigenstates and their corresponding energies by exact diagonalization (or, in quantum chemistry language, a full CI calculation) of the Hamiltonian matrix in the basis of all possible 6-electron Slater determinants spanned by the 8 spin orbitals. It is worth pointing out that exact diagonalization includes all many-electron correlation effects within our restricted Hilbert space. This is important because U/t >3 in this system. Figure IV-3b shows the energy surfaces of the ground and excited states of the extended Hubbard model. The many-body levels in the Figure IV-3b and Figure IV-3c are aligned by the following way. The ground-state energy surface is taken to be a parabola centered at the GEG and having the value of $E_{EEG}^{^3A_2} - E_{GEG}^{^3A_2} = 0.15eV$. This value of the structural energy is from *ab initio* DFT-LSDA calculation of the ground state, which is known to predict accurately such relative structural energy. The excited-state energy surfaces are obtained by adding the calculated excitation energy to the ground-state energy surface.

In the range of generalized coordinates considered, the many-body states listed in Table IV-2 are ordered (from low to high energies) as $^3A_2$, ^1E, and $^1A_1$ in the e^2 hole configuration and, ^3E and ^1E in the v^1e^1 hole configuration [128,129]. If there were no electron-electron interaction, the hole occupation in the many-body state of lowest energy corresponds to having two holes in the two e orbitals (e^2) (see Table IV-2). The hole occupation in the first excited many-body state corresponds to one hole in one of the e orbitals and the other in one of the v orbitals (v^1e^1). In Table IV-2, we list all possible symmetry adapted many-body states labeled by their C_{3v} symmetry representation. In the e^2 configuration, the 6 many-body states can be labeled with 3-fold degenerate $^3A_2$, two-fold degenerate ^1E, and non-degenerate $^1A_1$ states. The v^1e^1 configuration is spanned by 6-fold degenerate ^3E and 2-fold degenerate ^1E states. These degeneracies are lifted when one includes electron-electron interactions. If we assume that the many-body states of the interacting system are close to the many-body state of the non-interacting system shown in Table IV-2, the energy splitting in the degenerate subspace for a given hole configuration is a consequence of electron-electron interaction. In the e^2 configuration, triplet states should be lower in energy than singlet states. This is because the triplet (singlet) states are odd (even) with respect to exchange of two hole orbitals so that two holes cannot (can) occupy the same orbital. So, the triplet state would have lower Coulomb repulsion than singlet states. Between the two different singlet states in e^2 configuration, $^1A_1$ state should be higher in energy than ^1E states. This is because, as shown in Table IV-2, two holes occupy the same orbital in $^1A_1$. In contrast, two holes occupy different orbitals in e_y of the state of ^1E. Two holes in e_x of ^1E occupy the same orbital but the relative phase between

the two basis configurations is π, so that Coulomb repulsion contribution should cancel each other. Using the same argument as above, ^{3}E should be lower in energy than ^{1}E in the v^1e^1 configuration. Electron-electron interaction effect on the level order between the two different triplet $^3A_2$ and ^{3}E should be small because the Coulomb repulsion parameter for carbon and nitrogen is the same in the present model. Following all these arguments, one can expect the low-lying many-body state to be ordered as $^3A_2$, ^{1}E, and ^{1}A in the e^2 configuration, and ^{3}E and ^{1}E in the v^1e^1 configuration. However, the position of ^{3}E in v^1e^1 with respect to ^{1}E and ^{1}A in e^2 cannot be ascertained based solely on symmetry arguments.

Without any free parameters, our calculated many-body energy level differences for the triplet states match very well with experimental findings: (i) $E_{GEG}^{^3E} - E_{GEG}^{^3A_2} = 2.1$ eV, as compared to experimental vertical absorption energy of 2.2 eV. (ii) $E_{EEG}^{^3E} - E_{EEG}^{^3A_2} = 1.8$ eV, as compared to experimental vertical emission energy of 1.8 eV. (iii) A zero phonon line $E_{EEG}^{^3E} - E_{GEG}^{^3A_2} = 2.0$ eV, as compared to experimental value of 1.945 eV [108].

Figure IV-3b shows that the ordering of ^{3}E and $^1A_1$ levels is inverted as the system relaxes beyond EEG. This inversion of the ordering allows for the possibility of an intersystem crossing between these states. If intersystem crossing is mediated by spin-orbit coupling, which is known as the only mechanism to couple many-body states of different spin multiplicities in this system [128,129], only the ^{3}E state with A_1 representation ($m_s = \pm 1$) can couple to $^1A_1$ as shown in Table IV-2. As discussed more below, these findings explain the observed optical initialization from the $m_s = \pm 1$ excited triplet state. Our results are distinctly different from those from a recent *ab initio* GW-BSE study [123], where a level crossing between the ^{3}E and ^{1}E' levels is reported and there is no crossing between the ^{3}E and $^1A_1$ levels. We also computed the excited-state energies within the same GW-BSE approximation for the extended Hubbard model in the same Hilbert space; the results are shown in Figure IV-3c. Our calculated GW-BSE results for the extended Hubbard model reproduce the *ab initio* GW-BSE results in Ref. [123]. Figure IV-3c shows that the ^{3}E and ^{1}E' level are indeed very close within the GW-BSE approach as in Ref. [123]. The difference between the results from conventional GW-BSE and exact diagonalization arises from: i) the number of configurations (Slater determinants) to describe the many-electron states, and ii) how these two methods treat electron-electron interaction. Conventional GW-BSE approach take only one, e.g., the $|e_x e_y>$ configurations out of the three fold degenerate ground state ($^3A_2$) configurations of $|e_x e_y>$, $|\bar{e}_x \bar{e}_y>$, and $1/\sqrt{2}\,|e_x \bar{e}_y> + 1/\sqrt{2}\,|\bar{e}_x e_y>$ in Table IV-2. Then it considers single electron-hole excitation and de-excitation from them. Due to this less complete description, the number of configurations composing a particular state within the GW-BSE calculation is smaller than the actual number of configurations from an exact diagonalization calculation. For instance, if one considers the ^{3}E representation in Table IV-2, exact diagonalization would give rise to states mixing all 6 configurations ($|ve_x>$, $|\bar{v}\bar{e}_x>$, $|ve_y>$, $|\bar{v}\bar{e}_y>$, $1/\sqrt{2}\,|v\bar{e}_y> + 1/\sqrt{2}\,|\bar{v}e_y>$, $1/\sqrt{2}\,|v\bar{e}_x\rangle + 1/\sqrt{2}\,|\bar{v}e_x\rangle$). However, within GW-BSE, the ^{3}E states would only consist of two configurations (|v e_x> and |v e_y>) and are two-fold degenerate. As for the treatment of

interactions, standard GW-BSE method being a perturbative approach is an approximation to exact diagonalization in several ways for a given Hamiltonian. Conceptually, it doesn't include vertex contribution in evaluating the electron self-energy, and the electron-hole interaction kernel in the Bethe-Salpeter equation is taken at the GW level.

While knowing the excited-state level positions is a necessary requirement of any model that would explain optical initialization, they are of themselves not sufficient. To have a complete understanding of the process, it is also important to calculate the transition rate between the many-body states. Our calculations lead to the following optical initialization mechanism shown in Figure IV-3d. First, an electron is excited radiatively from the $^3A_2$ ground-state level to the ^3E level, both are spin triplet states. Second, the $^1A_1$ ($m_s = \pm 1$) state in the ^3E level is de-excited to the $^1A_1$ level by an intersystem crossing mediated by spin-orbit coupling. For the last step, two paths are possible. One possible transition path to the final ground state is an intersystem crossing mediated by spin-orbit interaction [128,129] from $^1A_1$ to the m_s=0 state of the ground-state $^3A_2$ level. The other possible path to the final ground state is first a non-radiative transition from $^1A_1$ to ^1E by electron-multiple phonon interaction and a subsequent intersystem crossing transition from the ^1E level to the m_s=0 state of $^3A_2$ by spin-orbit coupling, enabled by dynamic-Jahn-Teller-effect-assisted symmetry lowering of the structure from C_{3V} to C_{1h} [129].

The proposed mechanism is supported by agreement of the calculated transition rates with the corresponding measured values. We have calculated radiative de-excitation lifetime between many-body states. Within the electric dipole approximation, the radiative transition lifetime from many-body state $\left|\Psi_i\right\rangle$ to many-body state $\left|\Psi_j\right\rangle$ is given by $3c^3 \Big/ 4nE_{ij}^3 \left|\vec{r}_{ij}\right|^2$ in atomic unit [142], where n is index of refraction of diamond, $\vec{r}_{ij} = \left\langle \Psi_i \left| \vec{r} \right| \Psi_j \right\rangle$ and $E_{ij} = E_i - E_j$ are the dipole matrix element and transition energy. For the calculation of dipole matrix element between two many-body states, the position operator is $\vec{r} = \sum_\alpha \vec{r}_\alpha$ where α denotes the α_{th} electron and we calculated $\vec{r}_{ij}$ using *ab initio* quasiparticle wavefunctions forming the Slater determinants that span our restricted Hilbert space. The triplet-triplet ($^3E \rightarrow {}^3A_2$) radiative de-excitation lifetime is calculated to be 20 ns using our calculated many-body states and within the electric dipole approximation, as compared to the experimental value of 13 ns. Radiative de-excitation from the $^1A_1$ state to the lower singlet state of ^1E is calculated to be ~70 ns, which is much larger than the reported lifetime of 1 ns [14]. It is consistent with the experimental observation that de-excitation from the singlet level (that the system in the initially optically excited triplet state decayed nonradiatively to), in our model is $^1A_1$, is dominated by nonradiative transition [14,15]. We therefore assign that the de-excitation from $^1A_1$ is dominated by nonradiative transition.

The intersystem crossing rate between ^3E and $^1A_1$, mediated by spin-orbit coupling, is calculated to be ~50 ns within a displaced harmonic oscillator model, as compared to the experimental value of 30 ns [132]. We calculated it within the first order perturbation by spin-orbit coupling including dephasing effect. First, we assumed that initial state for intersystem crossing is A_1 in ^3E with α number of phonon and final state is any phonon-excited states in the $^1A_1$ energy surface, satisfying energy conservation law. d is displacement between

initial and final state energy surface, ΔE_0 is electronic energy changes, and λ is reorganization energy (nuclear energy change when the system is displaced from it's minimum to d). Nonradiative transition rate from ^{3}E to ^{1}A$_1$ is calculated within the first order perturbation by spin-orbit coupling including dephasing effect. First we assumed that initial state is A$_1$ in ^{3}E with α number of phonons, which is localized at the NV$^-$ center. Vertical absorption from the ground state (^{3}A$_2$) energy surface excites the system into the ^{3}E state with energy of 0.2 eV higher than the minimum of ^{3}E. This is about 2 times of the local vibrational mode energy (~70 meV) of the NV$^-$ center [128]. The final state will be any phonon-excited states in the ^{1}A$_1$ energy surface, satisfying energy conservation for the nonradiative transition. The unperturbed Hamiltonian for the system is composed of electronic as well as nuclear degrees of freedom. We modeled the nuclear motion of NV$^-$ as a harmonic oscillator with mode frequency of ω. Spin-orbit coupling is assumed to be the perturbing Hamiltonian V. From first order perturbation theory, total nonradiative transition rate between initial (|I>) and final (|F>) state can be calculated by knowing time correlation function of the spin-orbit coupling Hamiltonian [143]

$$W = \sum_F \int_{-\infty}^{-\infty} dt \left\langle I \left| e^{iH_I t} V e^{-iH_F t} \right| F \right\rangle \left\langle F \left| V \right| I \right\rangle \quad \text{(II-94)},$$

where H_I and H_F are the initial- and final-state Hamiltonian. To calculate the matrix elements, we used two approximations: Born-Oppenheimer approximation and Condon approximation. Within the Born-Oppenheimer approximation, electronic and nuclear parts of wavefunctions can be decoupled. Within the Condon approximation, spin-orbit coupling is assumed to be independent of the nuclear geometry. Then, we can decouple the nuclear and electronic contributions to the matrix element completely as follows.

$$W = \int_{-\infty}^{\infty} dt \left| V\left(R_0\right) \right|^2 e^{i\Delta E_0 t} f_{FC} \qquad \text{(II-95)}$$

with

$$f_{FC} = \sum_{F_n} \left\langle I_n \left| e^{iH_{I_n} t} e^{-iH_{F_n} t} \right| F_n \right\rangle \left\langle F_n \mid I_n \right\rangle \qquad \text{(II-96)}$$

where $\left|I_e\right\rangle$ and $\left|F_e\right\rangle$ are the electronic part of initial and final state wavefunctions and $\left|I_n\right\rangle$ and $\left|F_n\right\rangle$ are the nuclear part of initial and final state wavefunctions. R_0 is the GEG and ΔE_0 is electronic energy change between initial and final states. The Frank-Condon factor (f_{FC}) describes nuclear wavefunction overlap between initial and final state. Here, we assumed that the nuclear part of the Hamiltonian of initial ($H_{I,n}$) and final ($H_{F,n}$) states can be described by a displaced harmonic oscillator model, which is widely used in Markus's theory [144–147] for electron-transfer reactions. The initial- and final-state energy surface are assumed to have the same curvature with phonon frequency f_{FC} of ω, which is not a bad assumption for our case as we see from Figure IV-3b. Then $H_{F,n}$ is a displaced harmonic oscillator by d from $H_{I,n}$ as

shown in Figure IV-4. Dephasing by states outside of our Hilbert space as well as ensemble measurement is considered by the short-time approximation. Homogeneous broadening effect by states outside of our Hilbert space can be characterized by a coherence time (t_c) of local vibration mode. From the fact that nonradiative transition rate is ~30 ns, we conclude that t_c is longer than 30 ns. Inhomogenous broadening can be characterized by broadening parameter () η of $\sqrt{2\lambda kT}$ =0.1 eV. Since our system is in the regime where inhomogeneous broadening is dominant ($\eta \gg \hbar / t_c$), we used the short-time approximation to [143–147] to mimick dephasing effect. Then, the transition rate is given as follows.

$$W = \left|\left\langle I_e \middle| V \middle| F_e \right\rangle\right|^2 \sqrt{2\pi}\frac{1}{\eta} \times \left\{ \sum_{j=0}^{\alpha} \sum_{k=0}^{2\alpha-2j} \frac{\left(\tilde{d}^2\right)^{\alpha-j}\left(n+1\right)^{2\alpha-j}}{j!} \frac{\alpha!}{j!(\alpha-j)!} \frac{(2\alpha-2j)!}{(2\alpha-2j-k)!k!} e^{-\frac{\left(\Delta E_0-\lambda+(\alpha-j-k)\omega\right)^2}{2\eta^2}} \right\} \quad \text{(II-97)}$$

where λ is the reorganization energy (i.e., the energy change when system is displaced from its minimum to d as shown in Figure IV-4, $\tilde{d} = \sqrt{\lambda / \hbar\omega}$ is a reduced displacement between harmonic oscillators, and $n = 1/(e^{\hbar\omega/kT} - 1)$ is average phonon number at temperature T of 300K. With parameters of $\Delta E_0 = 0.5eV$, $V = 20\mu eV$ [128,129], $\omega = 70meV$ [128], $\lambda = 0.2eV$, we get a lifetime of 50 ns.

A definitive calculation of the rate of the last step of this mechanism is beyond our current model. The overall process nevertheless explains all the steps consistently with experiments in the optical initialization to the $m_s = 0$ ground state. It should be noted that within our formalism, we cannot absolutely determine the equilibrium geometries of the singlet states, $^1A_1$ and ^1E, which can't be represented by a single Slater determinant and therefore cannot compare directly to the singlet-singlet zero-phonon line experiments [121,122]

(d) Conclusion

To conclude, we have constructed a theoretical model to understand the physical mechanism for the optical initialization of spin of NV^- center in diamond. Using exact diagonalization of an extended Hubbard Hamiltonian determined from *ab initio* GW calculations, we incorporated full electron-electron interactions, the diamond host screening, and geometrical relaxation effects in the calculation. The computed ground- and excited-state energy surfaces and transition rates between them provided a consistent picture with experiments in support of an optical initialization path of $^3A_2 \rightarrow {}^3E \rightarrow {}^1A_1 \rightarrow {}^3A_2$ or $^3A_2 \rightarrow {}^3E \rightarrow {}^1A_1 \rightarrow {}^1E \rightarrow {}^3A_2$ in which intersystem crossings play a crucial role. Our method should be applicable to other deep centers in large band gap materials.

Parameters (eV)	E_C-E_N	t_{NC}	t_{CC}	U	V
GEG	2.56	-0.68	-1.03	3.43	0.83
EEG	2.86	-0.75	-0.90	3.45	0.67

Table IV-1. Extended Hubbard model interaction parameters. Model parameters in Eq. (1) at the ground-state equilibrium geometry (GEG) and the optically excited-state equilibrium geometry (EEG).

Hole Occ.	Representation		Many-body States
	w/o SO	w SO	
v^1e^1	${}^1E'$	E_x	$1/\sqrt{2}\left\|v\bar{e}_x\right\rangle - 1/\sqrt{2}\left\|\bar{v}e_x\right\rangle$
		E_y	$1/\sqrt{2}\left\|v\bar{e}_y\right\rangle - 1/\sqrt{2}\left\|\bar{v}e_y\right\rangle$
	${}^3E$	E_x	$1/2\left\|ve_x\right\rangle - 1/2\left\|\bar{v}\bar{e}_x\right\rangle - i/2\left\|ve_y\right\rangle + i/2\left\|\bar{v}\bar{e}_y\right\rangle$
		E_y	$-1/2\left\|ve_x\right\rangle + 1/2\left\|\bar{v}\bar{e}_x\right\rangle + i/2\left\|ve_y\right\rangle + i/2\left\|\bar{v}\bar{e}_y\right\rangle$
		E_x	$1/\sqrt{2}\left\|v\bar{e}_y\right\rangle + 1/\sqrt{2}\left\|\bar{v}e_y\right\rangle$
		E_y	$1/\sqrt{2}\left\|v\bar{e}_x\right\rangle + 1/\sqrt{2}\left\|\bar{v}e_x\right\rangle$
		A_2	$1/2\left\|ve_x\right\rangle - 1/2\left\|\bar{v}\bar{e}_x\right\rangle + i/2\left\|ve_y\right\rangle + i/2\left\|\bar{v}\bar{e}_y\right\rangle$
		A_1	$1/2\left\|ve_x\right\rangle + 1/2\left\|\bar{v}\bar{e}_x\right\rangle + i/2\left\|ve_y\right\rangle - i/2\left\|\bar{v}\bar{e}_y\right\rangle$
e^2	${}^1A_1$	A_1	$1/\sqrt{2}\left\|e_x\bar{e}_x\right\rangle + 1/\sqrt{2}\left\|e_y\bar{e}_y\right\rangle$
	${}^1E$	E_x	$1/\sqrt{2}\left\|e_x\bar{e}_x\right\rangle - 1/\sqrt{2}\left\|e_y\bar{e}_y\right\rangle$
		E_y	$1/\sqrt{2}\left\|e_x\bar{e}_y\right\rangle - 1/\sqrt{2}\left\|\bar{e}_xe_y\right\rangle$
	${}^3A_2$	E_x	$1/\sqrt{2}\left\|e_xe_y\right\rangle - 1/\sqrt{2}\left\|\bar{e}_x\bar{e}_y\right\rangle$
		E_y	$1/\sqrt{2}\left\|e_xe_y\right\rangle + 1/\sqrt{2}\left\|\bar{e}_x\bar{e}_y\right\rangle$
		A_1	$1/\sqrt{2}\left\|e_x\bar{e}_y\right\rangle + 1/\sqrt{2}\left\|\bar{e}_xe_y\right\rangle$

Table IV-2. Low-lying many-body states of the NV^- center in diamond denoted by hole occupations and their symmetry representations (degenerate representation without spin-orbit coupling and corresponding spin-orbit split representations). Instead of electron occupation of single-particle orbitals, one can equivalently express a many-body state by holes occupation. Each ket vector represents a 6-orbital Slater determinant in second-quantized notation, for example, $c_a c_b \left|f\right\rangle = \left|ab\right\rangle$, where $\left|f\right\rangle$ is the fully filled configuration (the 8-orbital Slater determinant).

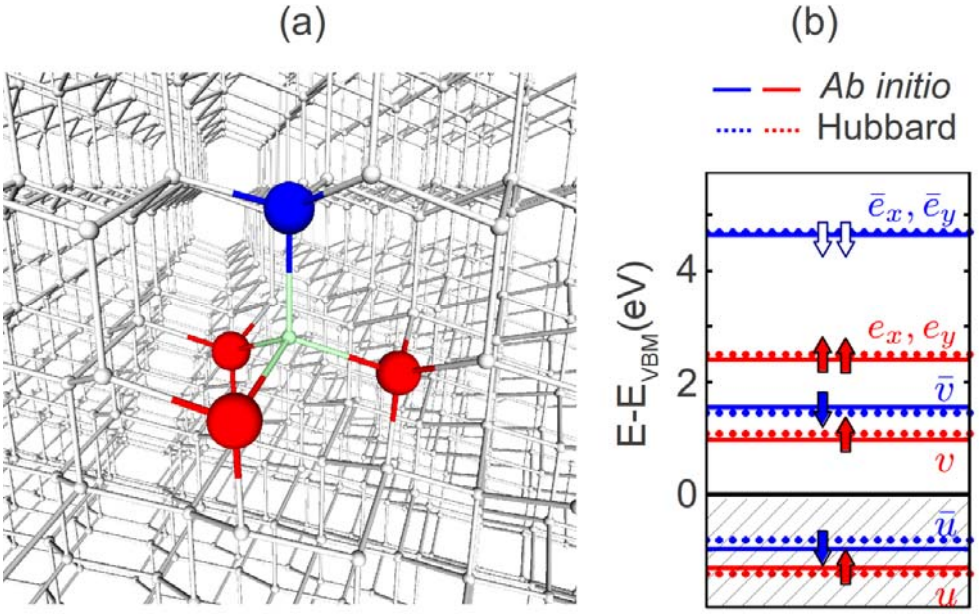

Figure IV-1. (a) Ground-state structure. Carbon (nitrogen) atom nearest to the vacancy site (light green colored sphere) is marked by red (blue) color. (b) Quasiparticle energy levels near the band gap, from *ab initio* GW calculation (solid line) of a NV^- center in diamond and from GW calculation of the extended Hubbard model (dotted line). The filled and open arrows correspond to quasi-hole and quasiparticle state (i.e., removing and adding an electron to the system), respectfully. For each spin, these levels belong to the two A_1 and one E representation in C_{3v} symmetry group. We label them as u ($\bar{u}$), v ($\bar{v}$), e_x ($\bar{e}_x$), and e_y ($\bar{e}_y$) for up (down) spin states, marked by red (blue) color.

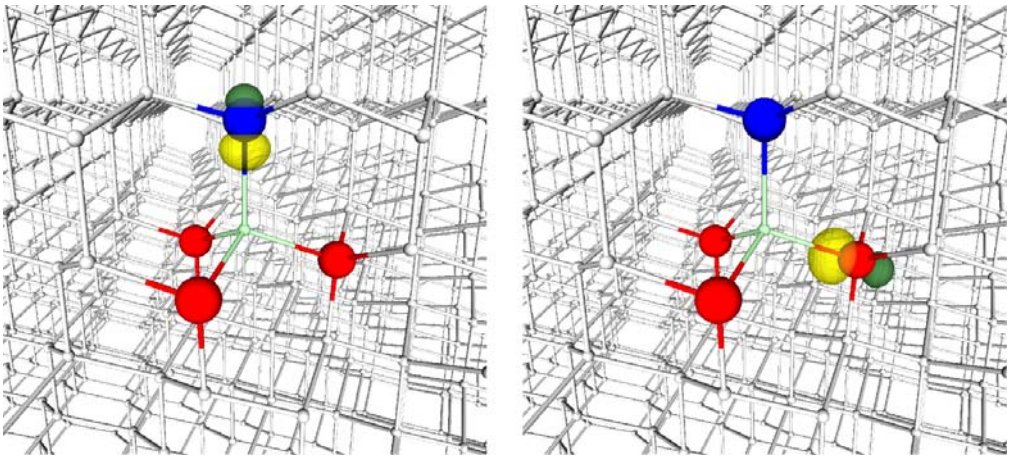

Figure IV-2. Defect-state Wannier functions. Isosuface plot of maximally localized spin-up Wannier function at amplitude $W(\vec{r}) = \pm |W(\vec{r})|_{\max} \times 0.5$, constructed from the 4 spin-up defect states in Figure IV-1b. Yellow (green) color denotes plus (minus) sign of the amplitude. The Wannier function centered at each carbon is equivalent, so only one of them is shown.

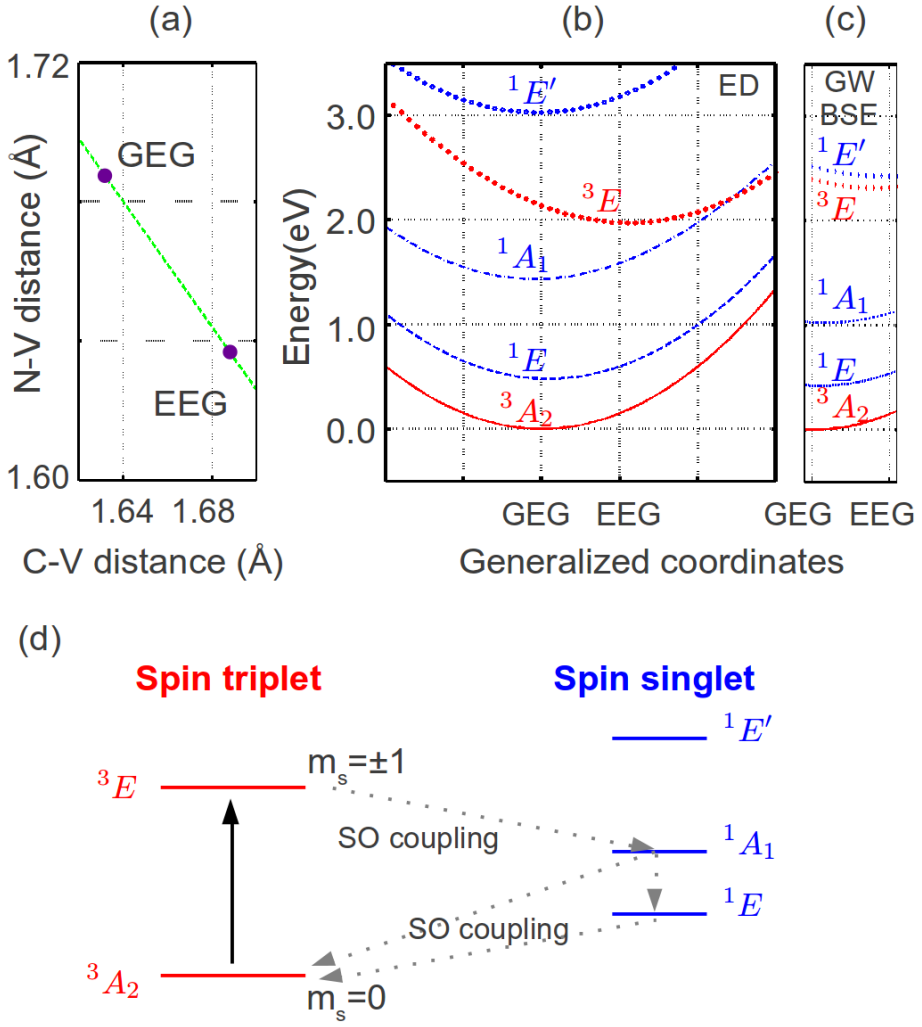

Figure IV-3. (a) Relaxation path taken between the GEG and EEG. (b) Energy surfaces from exact diagonalization of the extended Hubbard model. (c) Energy surfaces from a GW-BSE calculation of the extended Hubbard model. (d) Optical spin initialization mechanism supported by results from exact diagonalization of the extended Hubbard model.

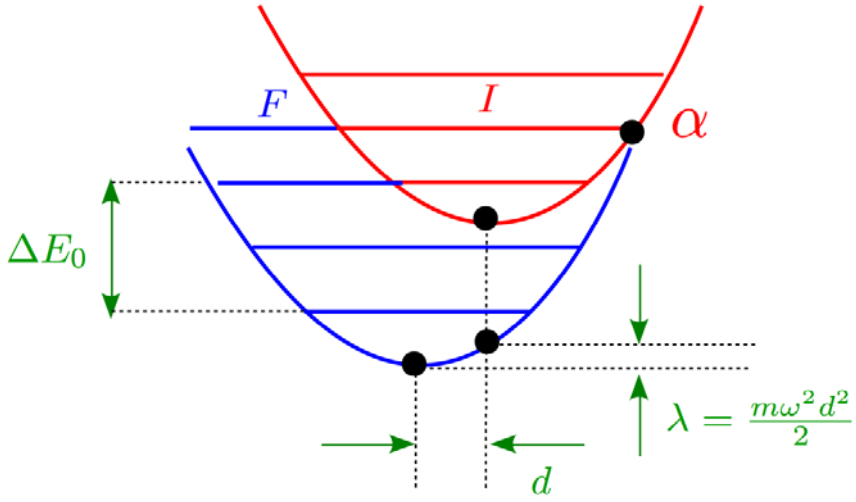

Figure IV-4. Displaced harmonic oscillator model. Initial state for intersystem crossing is A_1 in ^3E with α number of phonon and final state is any phonon-excited states in the $^1A_1$ energy surface, satisfying energy conservation law. d is displacement between initial and final state energy surface, ΔE_0 is electronic energy changes, and λ is reorganization energy (nuclear energy change when the system is displaced from it's minimum to d)

2. The screened charge associated with a single Ca dimer on an graphene sheet

(a) Introduction

Atomic collapse theory addresses the stability of an atom due to relativistic quantum effects. In light elements with the charge of nucleus (Z) less than a critical value $Z_c = 170$, [148] electrons make stable orbits around the nucleus. In contrast, in super-heavy elements with $Z > Z_c$, has been predicted that electrons collapse into the nucleus and positrons are emitted away. Although this theory dates back to Paul Dirac in the 1930s, experimental demonstrations have been hindered by the large threshold number of 170, which is higher than the atomic number of any atom in the periodic table.

Graphene has been predicted to be a good test material for atomic collapse theory [149–151]. First, electrons in graphene behave in a manner similar to relativistic electrons due to its linear band structure. Second, charged impurities on graphene can play the role of nucleus to the electrons, forming artificial atoms with the electron in graphene. Third, electrons in graphene move 300 times slower than the speed of light. As a consequence, atomic collapse in the artificial atom can be observed with a charge of the artificial nucleus 300 times smaller than 170. The atomic collapse state near a charged impurity on graphene is expected to be a spatially extended electronic resonance whose energy lies just below the Dirac point. Such resonances correspond to the electron-like part of the atomic collapse wavefunction.

The Crommie group at UC Berkeley measured, using scanning tunneling microscopy, electrons bound to the positively charged calcium dimers on graphene placed on a hexagonal boron nitride substrate, which corresponds to electrons collapsed to the super-heavy nucleus in artificial atoms. To compare measured bound states to atomic collapse theory in an artificial atom on graphene, the net charges associated with calcium dimers should be quantified. Here, we quantified the net charges associated with a calcium dimer.

(b) Theory and computation

As charges are transferred from a Ca dimer to graphene, into the band states as carriers, the Ca dimer becomes charged and the electrons in the graphene layer would self-consistently rearrange to screen the bare charge on the dimer. We computed the charge density around a calcium dimer on an isolated graphene sheet in the relaxed geometry obtained using the first-principles norm-conserving pseudopotential density functional theory (DFT), as implemented in the OpenMX package [152] which is based on a linear combination of pseudo-atomic orbital (LCPAO) method. The system is modeled by a n×n (n=8, 9, and 10) hexagonal graphene supercell with a Ca dimer as shown in Figure IV-5. The in- and out-of-graphene plane lattice constants are n×2.47 Å and 1000 Å, respectively. The Brillouin zone is sampled with a 3×3×1 Γ-centered k-point grid and the wavefunction cutoff used is 150Ry. In the calculated relaxed structure in the generalized gradient approximation to the exchange correlation functional, both

Ca atoms are located at 2.4 Å above the graphene plane with a Ca-Ca distance of 3.4 Å and the center of the Ca dimer is on the center of a C-C bond in graphene as shown in Figure IV-5.

(c) Results and discussion

Partitioning the electron density in real space can be used to evaluate the screened charge of the Ca dimer as seen by a test particle far from the dimer on an isolated graphene sheet. First, we define the electron density difference, quantifying the redistribution of the electron density due to the dimer-graphene interaction, as

$$\Delta\rho(\mathbf{r}) = \rho_{ca+g}(\mathbf{r}) - \rho_g(\mathbf{r}) - \rho_{ca}(\mathbf{r}), \quad \text{(II-98)}$$

where $\rho_{ca+g}(\mathbf{r})$ is the electron density of the combined dimer-graphene system, and $\rho_g(\mathbf{r})$ and $\rho_{ca}(\mathbf{r})$ are the electron density of an isolated graphene and an isolated Ca dimer in the same position as for the dimer-graphene system, respectively. Fig. S7 shows the z-direction-integrated charge density differences, $\Delta\bar{\rho}(x,y) = \int dz\, \Delta\rho(\mathbf{r})$. The electron density within a stadium-shaped region (a rectangles with a length of the Ca-Ca distance and a width of $2\times r_{sn}$ plus semicircles with a radius of r_{sn} on two sides) with the radius of r_{sn}, marked by black line in Figure IV-6, redistributes the most. The net electron accumulation density outside the stadium-shaped region of radius r_{sn} is due to the electron transferred from the Ca dimer to the graphene itinerary states, which is expected to decrease to zero in the infinite supercell size limit. We estimated the screened charge on a Ca-dimer as seen by a test charge at large distance by calculating the integrated $\Delta\bar{\rho}(x,y)$ (or the monopole charge) in a stadium-shaped region. The radius of the particular stadium r_{sn}, that gives the screened charge associated with a dimer, is defined in our calculation as the radius r_s at which the net charge inside the region has a maximum value in magnitude, which is expected for a single Ca dimer on an infinitely extended pristine graphene sheet. Figure IV-7 shows the net charge as a function r_s in our n×n graphene supercell calculation with n=8, 9, and 10, using the generalized gradient approximation to the exchange correlation functional. Around $r_s = 3.5\mathring{A}$, the net charge is at its maximum value in magnitude of -0.4e, where e is the electron charge, from all three supercell calculations regardless of the exchange correlation functional used. As r_s increases to the supercell size dimension, the calculated net charge within the stadium in our calculations converges to 0 due to the finite supercell size used and charge neutrality condition. An estimated fractional uncertainty in the value of the screened charge as evaluated here r_{sn}, originated from the finite supercell size and imposed charge neutrality condition, should roughly be given by the ratio of the stadium area given by r_{sn} to the supercell area; in the case of a 10x10 supercell, it would be around 10% if an order of 1 electron is donated from the Ca dimer to the conduction band of graphene.

In a second approach, we estimated the screened charge associated with a Ca dimer on an isolated graphene sheet employing another widely used method of "real space partition" [153]. The charge density is partitioned into two regions, one belonging to graphene and one to the Ca dimer. The position of the partitioning plane, which is parallel to the graphene plane (gray line in Figure IV-8), is defined as the position at which the region of charge depletion changes to that of charge accumulation for charge transfer from the dimer to the graphene, as calculated from the x-y planar integrated electron density difference, $\Delta\tilde{\rho}(z) = \int dxdy\, \Delta\rho(\mathbf{r})$, as shown in Figure IV-8 for the case of n=10. The screened charge associated with the Ca dimer is defined in this method by integrating $\Delta\tilde{\rho}(z)$ within the dimer region. This method also gives a screened charge value of -0.4e associated with the Ca dimer.

As a third method, the screened charge of a Ca dimer on an isolated graphene sheet is obtained from calculating the dipole moment of the graphene-dimer system along the graphene surface normal (out-of-plane) direction. By calculating the out-of-plane dipole moment of the system and knowing the separation between the Ca dimer and the graphene plane, we obtain also a screened charge of missing 0.4 electrons from the Ca dimer.

Our calculated results (from the three methods above and with three different supercell sizes) thus all give a screened charge of missing 0.4 electrons from the Ca dimer (i.e., a screened charge of -0.4 e) on an isolated graphene sheet. This value is insensitive to the particular exchange correlation functional used in our DFT calculation.

The dielectric screening from the electrons in the BN substrate is incorporated as follows. The dielectric screening from the electrons in the BN substrate renormalizes the bare Coulomb interaction in graphene, so that the dielectric constant of isolated graphene (ϵ_g) will be renormalized [154] and the total dielectric constant (ϵ_{tot}) of the dimer-graphene placed on the BN substrate may be represented as the product of the renormalized dielectric constant of graphene ($\tilde{\epsilon}_g$) and the dielectric constant of the BN substrate (ϵ_s) within random phase approximation to the longitudinal polarizability. The screened charge of a single Ca dimer on graphene placed on a BN substrate is thus given by $Z = \frac{(-0.4e)\times\epsilon_g}{\tilde{\epsilon}_g \times \epsilon_s}$, where ϵ_g = 3±1 [154–157], $\tilde{\epsilon}_g = 3.0 \pm 1.0$ [158], and $\epsilon_s = 2.5 \pm 0.5$ [159–161], where ϵ_g given here has a range of values depending on the method from which it is estimated. From *ab initio* calculation [157] at wavevectors relavant to this experiment its value is 2 to 4, while from a random phase approximation calculation [154,157] $\epsilon_g \approx 4$, and an experimental [156] measurements put it at $\epsilon_g \approx 2.2$. The uncertainty in $\tilde{\epsilon}_g$ arises from fitting experimental data to a Dirac model calculation [158] while uncertainty in ϵ_s comes from different reported values of the dielectric constant of BN [159–161] ($\epsilon_s = (1+\epsilon_{BN})/2$). By taking into account the uncertainties of the screened charge of a single dimer on isolated graphene in our calculation and uncertainty in the different dielectric constants, a resulting $Z/Z_c = 0.6 \pm 0.3$ for a single Ca dimer on graphene placed on a BN substrate is obtained (here $Z_c = \frac{\hbar v_F}{2e^2} = 0.25$ is the supercritical charge threshold).

(d) Conclusion

Z/Z_c associated with a Ca dimer deposited on graphene placed on BN substrate is estimated in the following ways. First, we calculated the screened charge associated with a Ca dimer on isolated graphene, as seen by a test charge at large distance, using three different methods described below and arrived at a value of a positively charged center with missing of 0.4 electrons from the neutral Ca dimer. Then the dielectric screening from a BN substrate is incorporated. The additional substrate screening reduces the screened charge, resulting in a Z/Z_c associated with a Ca dimer on graphene on a BN substrate estimated to be ~0.6±0.3, with $Z_c = \frac{\hbar v_F}{2e^2} = 0.25$.

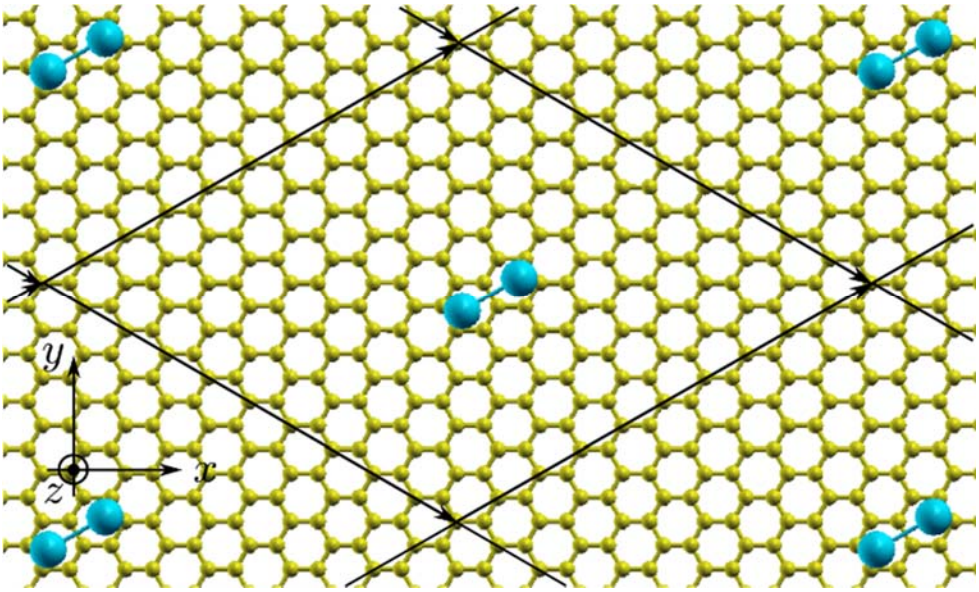

Figure IV-5. Geometrical structure for a single Ca dimer on a 10×10 hexagonal graphene supercell used in *ab initio* DFT calculation.

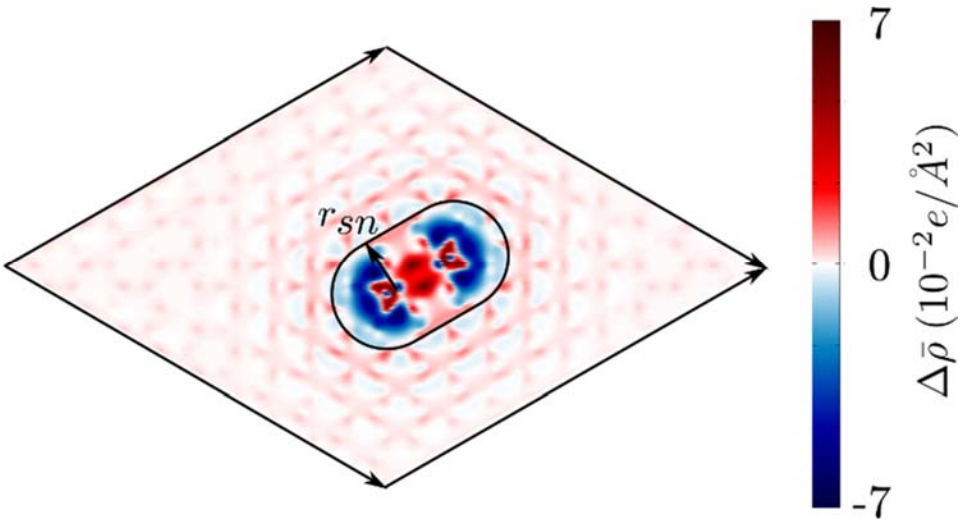

Figure IV-6. The z-direction-integrated charge density difference, $\Delta\bar{\rho}(x,y)=\int dz\,\Delta\rho(\mathbf{r})$, from a 10×10 hexagonal graphene supercell calculation where $\Delta\rho(\mathbf{r})$ is defined as the electron density difference between that of the combined graphene-dimer system and that of the individual entities as given in Eq. (II-98). The stadium-shaped region (a rectangle with a length of the Ca-Ca distance and a width of $2\times r_{sn}$ plus semicircles with a radius of r_{sn} on two sides) with a radius of r_{sn} is indicated by a black full line.

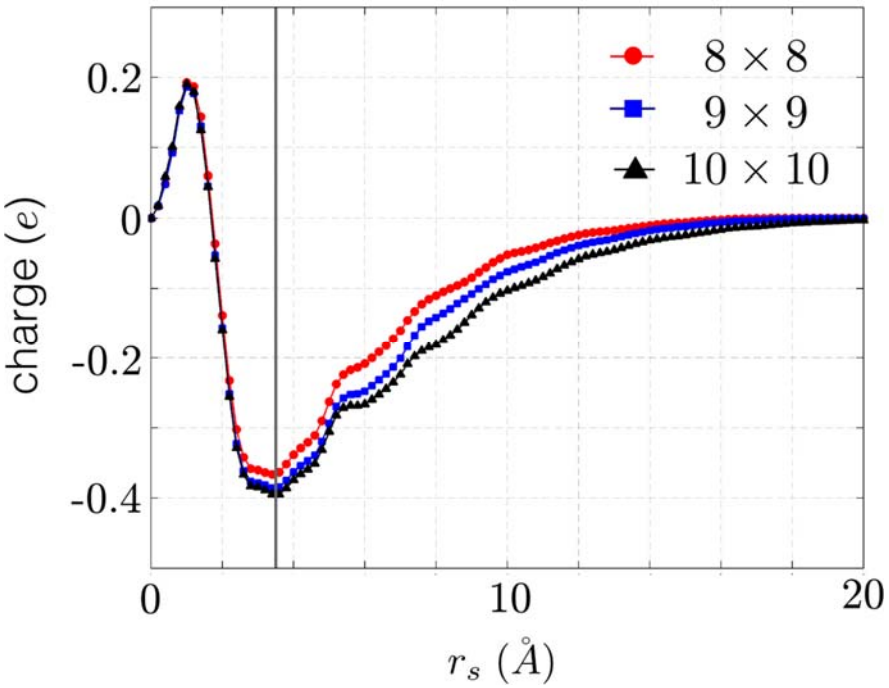

Figure IV-7. The net charge inside a stadium shaped region in Figure IV-6, as function of the stadium radius r_s from a n×n hexagonal graphene supercell calculation with n=8, 9, and 10. The particular stadium radius r_{sn} in Figure IV-6, that gives the screened charge associated with the Ca dimer in our calculation, is marked by a gray vertical line.

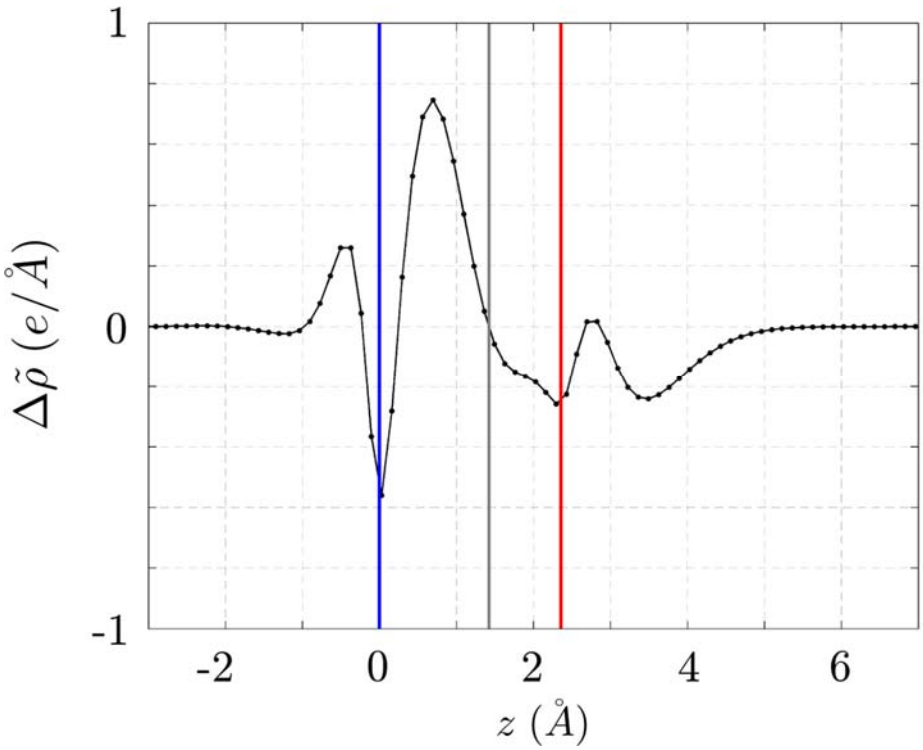

Figure IV-8. The x-y planar integrated electron density difference, $\Delta\tilde{\rho}(z) = \int dxdy\,\Delta\rho(\mathbf{r})$, as a function of position along the out-of graphene plane direction where $\Delta\rho(\mathbf{r})$ is defined as the electron density difference between that of the combined graphene-dimer system and that of the individual entities as given in Eq. 1S. Blue, gray, and red vertical lines indicate the positions of the graphene sheet, the partition plane (see text), and the Ca dimer, respectively.

V. References

[1] P. Hohenberg and W. Kohn, Phys. Rev. **136**, B864 (1964).
[2] R. M. Martin, *Electronic Structure: Basic Theory and Practical Methods* (Cambridge University Press, 2004).
[3] W. Kohn and L. J. Sham, Phys. Rev. **140**, A1133 (1965).
[4] G. Strinati, Phys. Rev. B **29**, 5718 (1984).
[5] P. W. Anderson, Phys. Rev. **124**, 41 (1961).
[6] S. Iijima, Publ. Online 07 Novemb. 1991 Doi101038354056a0 **354**, 56 (1991).
[7] S. Iijima and T. Ichihashi, Publ. Online 17 June 1993 Doi101038363603a0 **363**, 603 (1993).
[8] H. Kataura, Y. Kumazawa, Y. Maniwa, I. Umezu, S. Suzuki, Y. Ohtsuka, and Y. Achiba, Synth. Met. **103**, 2555 (1999).
[9] J. A. Misewich, R. Martel, P. Avouris, J. C. Tsang, S. Heinze, and J. Tersoff, Science **300**, 783 (2003).
[10] M. Freitag, Y. Martin, J. A. Misewich, R. Martel, and P. Avouris, Nano Lett **3**, 1067 (2003).
[11] T. Ando, J. Phys. Soc. Jpn. **66**, 1066 (1997).
[12] C. D. Spataru, S. Ismail-Beigi, L. X. Benedict, and S. G. Louie, Phys. Rev. Lett. **92**, 077402 (2004).
[13] J. Deslippe, C. D. Spataru, D. Prendergast, and S. G. Louie, Nano Lett **7**, 1626 (2007).
[14] R. Saito, G. Dresselhaus, and M. S. Dresselhaus, *Physical Properties of Carbon Nanotubes* (Imperial College Press, 1998).
[15] G. G. Samsonidze, A. R. Saito, D. A. Jorio, E. M. A. Pimenta, E. A. G. Souza Filho, F. A. Grüneis, D. G. Dresselhaus, and M. S. Dresselhausa, J. Nanosci. Nanotechnol. **3**, 431 (2003).
[16] R. B. Capaz, C. D. Spataru, S. Ismail-Beigi, and S. G. Louie, Phys. Rev. B **74**, 121401 (2006).
[17] A. Jorio, C. Fantini, M. A. Pimenta, R. B. Capaz, G. G. Samsonidze, G. Dresselhaus, M. S. Dresselhaus, J. Jiang, N. Kobayashi, A. Grüneis, and R. Saito, Phys. Rev. B **71**, 075401 (2005).
[18] J. Jiang, R. Saito, G. G. Samsonidze, A. Jorio, S. G. Chou, G. Dresselhaus, and M. S. Dresselhaus, Phys. Rev. B **75**, 035407 (2007).
[19] M. S. Hybertsen and S. G. Louie, Phys. Rev. B **34**, 5390 (1986).
[20] M. Rohlfing and S. G. Louie, Phys. Rev. B **62**, 4927 (2000).
[21] L. Hedin, Phys. Rev. **139**, A796 (1965).
[22] E. Malić, M. Hirtschulz, F. Milde, M. Richter, J. Maultzsch, S. Reich, and A. Knorr, Phys. Status Solidi B **245**, 2155 (2008).
[23] J. Deslippe, G. Samsonidze, D. A. Strubbe, M. Jain, M. L. Cohen, and S. G. Louie, Comput. Phys. Commun. **183**, 1269 (2012).
[24] S. Ismail-Beigi, Phys. Rev. B **73**, 233103 (2006).
[25] T. Ando, J. Phys. Soc. Jpn. **69**, 1757 (2000).
[26] K. Ohno, Theor. Chem. Acc. Theory Comput. Model. Theor. Chim. Acta **2**, 219 (1964).
[27] P. W. Phillips, *Advanced Solid State Physics* (Westview Press, 2003).

[28] A. Svane and O. Gunnarsson, Phys. Rev. B **37**, 9919 (1988).
[29] W. von der Linden and P. Horsch, Phys. Rev. B **37**, 8351 (1988).
[30] M. Rohlfing, P. Krüger, and J. Pollmann, Phys. Rev. B **52**, 1905 (1995).
[31] F. Léonard and J. Tersoff, Appl. Phys. Lett. **81**, 4835 (2002).
[32] P. Y. Yu and M. Cardona, *Fundamentals of Semiconductors: Physics and Materials Properties* (Springer, 2010).
[33] S. Balasubramanian, Am. J. Phys. **58**, 1204 (1990).
[34] E. B. Barros, R. B. Capaz, A. Jorio, G. G. Samsonidze, A. G. Souza Filho, S. Ismail-Beigi, C. D. Spataru, S. G. Louie, G. Dresselhaus, and M. S. Dresselhaus, Phys. Rev. B **73**, 241406 (2006).
[35] R. Loudon, Am. J. Phys. **27**, 649 (1959).
[36] K. Liu, J. Deslippe, F. Xiao, R. B. Capaz, X. Hong, S. Aloni, A. Zettl, W. Wang, X. Bai, S. G. Louie, E. Wang, and F. Wang, Nat. Nanotechnol. **7**, 325 (2012).
[37] S. M. Bachilo, M. S. Strano, C. Kittrell, R. H. Hauge, R. E. Smalley, and R. B. Weisman, Science **298**, 2361 (2002).
[38] J. Lefebvre, J. M. Fraser, Y. Homma, and P. Finnie, Appl. Phys. Mater. Sci. Process. **78**, 1107 (2004).
[39] Kaihui Liu, Xiaoping Hong, Sangkook Choi, Rodrigo Capaz, Shaul Aloni, Wenlong Wang, Xuedong Bai, Steven Louie, Enge Wang, and Feng Wang, in preparation (n.d.).
[40] V. Perebeinos, J. Tersoff, and P. Avouris, Phys. Rev. Lett. **92**, 257402 (2004).
[41] T. Ando, J. Phys. Soc. Jpn. **74**, 777 (2005).
[42] K. S. Novoselov, A. K. Geim, S. V. Morozov, D. Jiang, Y. Zhang, S. V. Dubonos, I. V. Grigorieva, and A. A. Firsov, Science **306**, 666 (2004).
[43] K. S. Novoselov, D. Jiang, F. Schedin, T. J. Booth, V. V. Khotkevich, S. V. Morozov, and A. K. Geim, Proc. Natl. Acad. Sci. U. S. A. **102**, 10451 (2005).
[44] K. S. Novoselov, A. K. Geim, S. V. Morozov, D. Jiang, M. I. Katsnelson, I. V. Grigorieva, S. V. Dubonos, and A. A. Firsov, Nature **438**, 197 (2005).
[45] Y. Zhang, Y.-W. Tan, H. L. Stormer, and P. Kim, Nature **438**, 201 (2005).
[46] P. R. Wallace, Phys. Rev. **71**, 622 (1947).
[47] G. W. Semenoff, Phys. Rev. Lett. **53**, 2449 (1984).
[48] T. Ando and T. Nakanishi, J. Phys. Soc. Jpn. **67**, 1704 (1998).
[49] P. L. McEuen, M. Bockrath, D. H. Cobden, Y.-G. Yoon, and S. G. Louie, Phys. Rev. Lett. **83**, 5098 (1999).
[50] M. I. Katsnelson, K. S. Novoselov, and A. K. Geim, Nat. Phys. **2**, 620 (2006).
[51] J. H. Bardarson, J. Tworzydło, P. W. Brouwer, and C. W. J. Beenakker, Phys. Rev. Lett. **99**, 106801 (2007).
[52] K. Nomura, M. Koshino, and S. Ryu, Phys. Rev. Lett. **99**, 146806 (2007).
[53] P. San-Jose, E. Prada, and D. S. Golubev, Phys. Rev. B **76**, 195445 (2007).
[54] M. Titov, EPL Europhys. Lett. **79**, 17004 (2007).
[55] Y. P. Bliokh, V. Freilikher, S. Savel'ev, and F. Nori, Phys. Rev. B **79**, 075123 (2009).
[56] Q. Zhao, J. Gong, and C. A. Müller, Phys. Rev. B **85**, 104201 (2012).
[57] N. Abedpour, A. Esmailpour, R. Asgari, and M. R. R. Tabar, Phys. Rev. B **79**, 165412 (2009).
[58] C.-H. Park, Y.-W. Son, L. Yang, M. L. Cohen, and S. G. Louie, Nano Lett. **8**, 2920 (2008).

[59] M. Z. Hasan and C. L. Kane, Rev. Mod. Phys. **82**, 3045 (2010).
[60] X. Huang, Y. Lai, Z. H. Hang, H. Zheng, and C. T. Chan, Nat. Mater. **10**, 582 (2011).
[61] G. H. Golub and C. F. V. Loan, *Matrix Computations* (JHU Press, 1996).
[62] J. J. Sakurai and J. Napolitano, *Modern Quantum Mechanics* (Addison-Wesley, 2010).
[63] V. V. Cheianov and V. I. Fal'ko, Phys. Rev. B **74**, 041403 (2006).
[64] P. Sheng, *Introduction to Wave Scattering: Localization and Mesoscopic Phenomena* (Springer, 2006).
[65] D. S. Fisher and P. A. Lee, Phys. Rev. B **23**, 6851 (1981).
[66] É. Akkermans and G. Montambaux, *Mesoscopic Physics of Electrons and Photons* (Cambridge University Press, 2007).
[67] S. Ryu, C. Mudry, A. Furusaki, and A. W. W. Ludwig, Phys. Rev. B **75**, 205344 (2007).
[68] S. Marchini, S. Günther, and J. Wintterlin, Phys. Rev. B **76**, 075429 (2007).
[69] J. C. Meyer, C. O. Girit, M. F. Crommie, and A. Zettl, Appl. Phys. Lett. **92**, 123110 (2008).
[70] W. Bao, F. Miao, Z. Chen, H. Zhang, W. Jang, C. Dames, and C. N. Lau, Nat. Nanotechnol. **4**, 562 (2009).
[71] L. Brey and J. J. Palacios, Phys. Rev. B **77**, 041403 (2008).
[72] A. Isacsson, L. M. Jonsson, J. M. Kinaret, and M. Jonson, Phys. Rev. B **77**, 035423 (2008).
[73] S. Dubey, V. Singh, A. K. Bhat, P. Parikh, S. Grover, R. Sensarma, V. Tripathi, K. Sengupta, and M. M. Deshmukh, Nano Lett. **13**, 3990 (2013).
[74] J. Berezovsky, M. F. Borunda, E. J. Heller, and R. M. Westervelt, Nanotechnology **21**, 274013 (2010).
[75] J. Clarke and A. I. Braginski, *The SQUID Handbook: Fundamentals and Technology of SQUIDs and SQUID Systems* (John Wiley & Sons, 2006).
[76] F. C. Wellstood, C. Urbina, and J. Clarke, Appl. Phys. Lett. **50**, 772 (1987).
[77] F. Yoshihara, K. Harrabi, A. O. Niskanen, Y. Nakamura, and J. S. Tsai, Phys. Rev. Lett. **97**, 167001 (2006).
[78] K. Kakuyanagi, T. Meno, S. Saito, H. Nakano, K. Semba, H. Takayanagi, F. Deppe, and A. Shnirman, Phys. Rev. Lett. **98**, 047004 (2007).
[79] R. C. Bialczak, R. McDermott, M. Ansmann, M. Hofheinz, N. Katz, E. Lucero, M. Neeley, A. D. O'Connell, H. Wang, A. N. Cleland, and J. M. Martinis, Phys. Rev. Lett. **99**, 187006 (2007).
[80] T. Lanting, A. J. Berkley, B. Bumble, P. Bunyk, A. Fung, J. Johansson, A. Kaul, A. Kleinsasser, E. Ladizinsky, F. Maibaum, R. Harris, M. W. Johnson, E. Tolkacheva, and M. H. S. Amin, Phys. Rev. B **79**, 060509 (2009).
[81] R. H. Koch, D. P. DiVincenzo, and J. Clarke, Phys. Rev. Lett. **98**, 267003 (2007).
[82] S. Machlup, J. Appl. Phys. **25**, 341 (1954).
[83] P. Dutta and P. M. Horn, Rev. Mod. Phys. **53**, 497 (1981).
[84] R. de Sousa, Phys. Rev. B **76**, 245306 (2007).
[85] L. Faoro and L. B. Ioffe, Phys. Rev. Lett. **100**, 227005 (2008).
[86] S. Sendelbach, D. Hover, A. Kittel, M. Mück, J. M. Martinis, and R. McDermott, Phys. Rev. Lett. **100**, 227006 (2008).

[87] H. Bluhm, J. A. Bert, N. C. Koshnick, M. E. Huber, and K. A. Moler, Phys. Rev. Lett. **103**, 026805 (2009).
[88] S. G. Louie and M. L. Cohen, Phys. Rev. B **13**, 2461 (1976).
[89] H. Nyquist, Phys. Rev. **32**, 110 (1928).
[90] M. L. Cohen, M. Schlüter, J. R. Chelikowsky, and S. G. Louie, Phys. Rev. B **12**, 5575 (1975).
[91] S. G. Louie, J. R. Chelikowsky, and M. L. Cohen, Phys. Rev. B **15**, 2154 (1977).
[92] P. W. Anderson, Phys. Rev. **109**, 1492 (1958).
[93] A. MacKinnon and B. Kramer, Phys. Rev. Lett. **47**, 1546 (1981).
[94] J. D. Sau, J. B. Neaton, H. J. Choi, S. G. Louie, and M. L. Cohen, Phys. Rev. Lett. **101**, 026804 (2008).
[95] J. K. Tomfohr and O. F. Sankey, Phys. Rev. B **65**, 245105 (2002).
[96] W. Kohn, Phys. Rev. **115**, 809 (1959).
[97] M. A. Ruderman and C. Kittel, Phys. Rev. **96**, 99 (1954).
[98] T. Kasuya, Prog. Theor. Phys. **16**, 45 (1956).
[99] K. Yosida, Phys. Rev. **106**, 893 (1957).
[100] M. B. Weissman, Rev. Mod. Phys. **65**, 829 (1993).
[101] R. Harris, M. W. Johnson, S. Han, A. J. Berkley, J. Johansson, P. Bunyk, E. Ladizinsky, S. Govorkov, M. C. Thom, S. Uchaikin, B. Bumble, A. Fung, A. Kaul, A. Kleinsasser, M. H. S. Amin, and D. V. Averin, Phys. Rev. Lett. **101**, 117003 (2008).
[102] A. L. Fetter and J. D. Walecka, *Quantum Theory of Many-Particle Systems* (Courier Dover Publications, 2003).
[103] S. Sendelbach, D. Hover, M. Mück, and R. McDermott, Phys. Rev. Lett. **103**, 117001 (2009).
[104] P. Anderson, Science (1978).
[105] S. Choi, D.-H. Lee, S. G. Louie, and J. Clarke, Phys. Rev. Lett. **103**, 197001 (2009).
[106] J. B. Neaton, M. S. Hybertsen, and S. G. Louie, Phys. Rev. Lett. **97**, 216405 (2006).
[107] C. Tao, J. Sun, X. Zhang, R. Yamachika, D. Wegner, Y. Bahri, G. Samsonidze, M. L. Cohen, S. G. Louie, T. D. Tilley, R. A. Segalman, and M. F. Crommie, Nano Lett. **9**, 3963 (2009).
[108] G. Davies and M. F. Hamer, Proc. R. Soc. Lond. Ser. Math. Phys. Sci. **348**, 285 (1976).
[109] A. Gruber, A. Dräbenstedt, C. Tietz, L. Fleury, J. Wrachtrup, and C. von Borczyskowski, Science **276**, 2012 (1997).
[110] F. Jelezko, T. Gaebel, I. Popa, M. Domhan, A. Gruber, and J. Wrachtrup, Phys. Rev. Lett. **93**, 130501 (2004).
[111] R. J. Epstein, F. M. Mendoza, Y. K. Kato, and D. D. Awschalom, Nat Phys **1**, 94 (2005).
[112] L. Childress, M. V. Gurudev Dutt, J. M. Taylor, A. S. Zibrov, F. Jelezko, J. Wrachtrup, P. R. Hemmer, and M. D. Lukin, Science **314**, 281 (2006).
[113] M. V. G. Dutt, L. Childress, L. Jiang, E. Togan, J. Maze, F. Jelezko, A. S. Zibrov, P. R. Hemmer, and M. D. Lukin, Science **316**, 1312 (2007).
[114] R. Hanson, V. V. Dobrovitski, A. E. Feiguin, O. Gywat, and D. D. Awschalom, Science **320**, 352 (2008).
[115] G. D. Fuchs, V. V. Dobrovitski, D. M. Toyli, F. J. Heremans, and D. D. Awschalom, Science **326**, 1520 (2009).

[116] G. D. Fuchs, V. V. Dobrovitski, D. M. Toyli, F. J. Heremans, C. D. Weis, T. Schenkel, and D. D. Awschalom, Nat Phys **6**, 668 (2010).
[117] B. B. Buckley, G. D. Fuchs, L. C. Bassett, and D. D. Awschalom, Science **330**, 1212 (2010).
[118] J. M. Taylor, P. Cappellaro, L. Childress, L. Jiang, D. Budker, P. R. Hemmer, A. Yacoby, R. Walsworth, and M. D. Lukin, Nat Phys **4**, 810 (2008).
[119] F. Dolde, H. Fedder, M. W. Doherty, T. Nöbauer, F. Rempp, G. Balasubramanian, T. Wolf, F. Reinhard, L. C. L. Hollenberg, F. Jelezko, and J. Wrachtrup, Nat. Phys. **7**, 459 (2011).
[120] G. Balasubramanian, P. Neumann, D. Twitchen, M. Markham, R. Kolesov, N. Mizuochi, J. Isoya, J. Achard, J. Beck, J. Tissler, V. Jacques, P. R. Hemmer, F. Jelezko, and J. Wrachtrup, Nat Mater **8**, 383 (2009).
[121] V. M. Acosta, A. Jarmola, E. Bauch, and D. Budker, Phys. Rev. B **82**, 201202 (2010).
[122] L. J. Rogers, S. Armstrong, M. J. Sellars, and N. B. Manson, New J. Phys. **10**, 103024 (2008).
[123] Y. Ma, M. Rohlfing, and A. Gali, Phys. Rev. B **81**, 041204 (2010).
[124] P. Delaney, J. C. Greer, and J. A. Larsson, Nano Lett **10**, 610 (2010).
[125] A. Ranjbar, M. Babamoradi, M. Heidari Saani, M. A. Vesaghi, K. Esfarjani, and Y. Kawazoe, Phys. Rev. B **84**, 165212 (2011).
[126] A. Gali, M. Fyta, and E. Kaxiras, Phys. Rev. B **77**, 155206 (2008).
[127] A. Lenef and S. C. Rand, Phys. Rev. B **53**, 13441 (1996).
[128] J. R. Maze, A. Gali, E. Togan, Y. Chu, A. Trifonov, E. Kaxiras, and M. D. Lukin, New J. Phys. **13**, 025025 (2011).
[129] M. W. Doherty, N. B. Manson, P. Delaney, and L. C. L. Hollenberg, New J. Phys. **13**, 025019 (2011).
[130] J. H. N. Loubser and J. A. van Wyk, Rep. Prog. Phys. **41**, 1201 (1978).
[131] A. P. Nizovtsev, S. Y. Kilin, F. Jelezko, I. Popa, A. Gruber, and J. Wrachtrup, Phys. B Condens. Matter **340-342**, 106 (2003).
[132] N. B. Manson, J. P. Harrison, and M. J. Sellars, Phys. Rev. B **74**, 104303 (2006).
[133] A. Gali, E. Janzén, P. Deák, G. Kresse, and E. Kaxiras, Phys. Rev. Lett. **103**, 186404 (2009).
[134] J.-L. Li, G.-M. Rignanese, E. K. Chang, X. Blase, and S. G. Louie, Phys. Rev. B **66**, 035102 (2002).
[135] F. M. Hossain, M. W. Doherty, H. F. Wilson, and L. C. L. Hollenberg, Phys. Rev. Lett. **101**, 226403 (2008).
[136] J. H. N. Loubser and J. A. van Wyk, *Diamond Research* (Industrial Diamond Information Bureau, London, 1977).
[137] A. A. Mostofi, J. R. Yates, Y.-S. Lee, I. Souza, D. Vanderbilt, and N. Marzari, Comput. Phys. Commun. **178**, 685 (2008).
[138] J. A. Majewski and P. Vogl, Phys. Rev. B **46**, 12219 (1992).
[139] Y. Xie, R. Han, and X. Zhang, Phys. Rev. B **58**, 12721 (1998).
[140] C. D. Spataru, S. Ismail-Beigi, R. Capaz, and S. Louie, in *Carbon Nanotub. Adv. Top. Synth. Struct. Prop. Appl.*, edited by A. Jorio, G. Dresselhaus, and M. S. Dresselhaus (Springer, 2008).

[141] C. Kittel, *Introduction to Solid State Physics* (Wiley, 2005).
[142] O. Svelto, *Principles of Lasers* (Springer, 2009).
[143] P. Scherer and S. F. Fischer, *Theoretical Molecular Biophysics* (Springer, 2009).
[144] J. Jortner, J. Chem. Phys. **64**, 4860 (1976).
[145] V. Balzani, A. Juris, M. Venturi, S. Campagna, and S. Serroni, Chem Rev **96**, 759 (1996).
[146] D. Beljonne, Z. Shuai, G. Pourtois, and J. L. Bredas, J Phys Chem A **105**, 3899 (2001).
[147] S. Mukamel, *Principles of Nonlinear Optical Spectroscopy* (Oxford University Press, 1999).
[148] W. Greiner and N. A. T. Organization, *Quantum Electrodynamics of Strong Fields* (Plenum Press, 1983).
[149] V. M. Pereira, J. Nilsson, and A. H. Castro Neto, Phys. Rev. Lett. **99**, 166802 (2007).
[150] A. V. Shytov, M. I. Katsnelson, and L. S. Levitov, Phys. Rev. Lett. **99**, 246802 (2007).
[151] A. V. Shytov, M. I. Katsnelson, and L. S. Levitov, Phys. Rev. Lett. **99**, 236801 (2007).
[152] T. Ozaki and H. Kino, Phys. Rev. B **72**, 045121 (2005).
[153] K. T. Chan, J. B. Neaton, and M. L. Cohen, Phys. Rev. B **77**, 235430 (2008).
[154] E. H. Hwang and S. Das Sarma, Phys. Rev. B **75**, 205418 (2007).
[155] T. Ando, J. Phys. Soc. Jpn. **75**, 074716 (2006).
[156] D. C. Elias, R. V. Gorbachev, A. S. Mayorov, S. V. Morozov, A. A. Zhukov, P. Blake, L. A. Ponomarenko, I. V. Grigorieva, K. S. Novoselov, F. Guinea, and A. K. Geim, Nat. Phys. **7**, 701 (2011).
[157] M. van Schilfgaarde and M. I. Katsnelson, Phys. Rev. B **83**, 081409 (2011).
[158] Y. Wang, V. W. Brar, A. V. Shytov, Q. Wu, W. Regan, H.-Z. Tsai, A. Zettl, L. S. Levitov, and M. F. Crommie, Nat. Phys. **8**, 653 (2012).
[159] C. R. Dean, A. F. Young, I. Meric, C. Lee, L. Wang, S. Sorgenfrei, K. Watanabe, T. Taniguchi, P. Kim, K. L. Shepard, and J. Hone, Nat. Nanotechnol. **5**, 722 (2010).
[160] R. Geick, C. H. Perry, and G. Rupprecht, Phys. Rev. **146**, 543 (1966).
[161] K. K. Kim, A. Hsu, X. Jia, S. M. Kim, Y. Shi, M. Dresselhaus, T. Palacios, and J. Kong, ACS Nano **6**, 8583 (2012).